UNIVERSITÀ DEGLI STUDI DI MILANO BICOCCA

Scuola di Dottorato di Scienze
Corso di Dottorato di Ricerca in Fisica e Astronomia

Laura Sironi
Matricola 041003

Nanoparticles for in-vitro and in-vivo biosensing and imaging

Tutore
Prof. Giuseppe Chirico

Coordinatore
Prof. Claudio Destri

Ciclo XXIII 2008-2010

Contents

Introduction

In the last two decades several groups have investigated the changes of chemical and physical properties of materials with size in the nanometric scale. These studies have highlighted a number of possible applications for nanostructures, which are now also employed, in biology and medicine, for imaging, disease detection, diagnosis, sensing and therapy.

Noble metal (especially gold and silver nanoparticles) are particularly versatile for these applications due to the phenomenon known as surface plasmon resonance (SPR), an in-phase oscillation of all the conduction band electrons that resonates with the light wave electric field. The resonance frequency depends on the size, shape, orientation and dielectric constant of the nanoparticle. The coupling of SPR with the electromagnetic field leads to a great enhancement of both the absorption and scattering cross sections. The overall extinction cross section of these nanoparticles (NPs) is 10^5-10^6 larger than that of organic dye. In contrast to common molecular chromophores, they are extremely photostable and, depending on the shape, they convert efficiently light into heat.

The SPR, tunable in the visible (for spherical NPs) and near-infrared region (for non spherically symmetric NPs) of the electromagnetic spectrum, can also affect the fluorescence emission of dyes and substantially modify their brightness and excited-state lifetime. Depending on the fluorophores-NP distance and the NPs anisotropy one can obtain fluorescence enhancement or quenching. In both cases we expect that any change in the dielectric constant of the NP surface, induced, for example, by a biorecognition process that occurs on the surface itself, can produce a change in the emission properties of the fluorophores. This expectation led us to devise a protein nanosensor described in this thesis.

The coupling of the SPR with dye electronic levels becomes also particularly important under two-photon excitation (TPE), which consists in the simultaneous absorption of two photons, each carrying about half the energy necessary to excite the molecule. This excitation technique has been particularly useful in the context of this work because it induces a significant luminescence emission of non spherically symmetric NPs: due to non-linear phenomena such as the TPE, the luminescence (TPL) intensity is enhanced

by many orders of magnitude with respect to the single photon excitation, improving the usefulness of these nanoparticles for in-vivo imaging in the NIR region of the electromagnetic spectrum.
TPE offers a series of unique features for biological investigation both in vitro and in vivo. First, the two-photon absorption bands of the dyes commonly used in biological studies are wider than their one-photon analogous allowing the simultaneous excitation of multiple fluorophores with a single excitation wavelength. Second, the stimulating light beam has a high penetration depth because of the long infra-red wavelengths used, allowing experiments in turbid media and biological tissues. Third, excitation takes place only at the plane of focus, due to the superlinear scaling of the probability of simultaneous photon absorption with the light intensity. As a consequence no excitation occurs outside of a thin layer close to the focal plane in the specimen. TPE and all non linear spectroscopies acquire then instrinsic 3D resolution and almost drastically reduce both photo-toxicity and fluorophore bleaching. These advantages make nowadays TPE a well established tool for scientific biological and medical research that can benefits from its coupling to the use of non spherically symmetric gold nanoparticles.
According to these considerations we have developed our project on two lines related to the use of gold nanoparticles for sensing and non linear imaging.
In the first part of this work we have reviewed the materials and methods used: in Chapter 1, the most relevant features of the surface plasmon resonance and the properties of spherical symmetric and asymmetric nanoparticles are presented.
Moreover, the interaction between fluorophores and nanoparticles and the basics of fluorescence emission and two-photon excitation employed in the reported measurements are discussed.
The aim of the first part of this research project (reported in Chapter 3) is to exploit changes of the dye excited-state lifetime and brightness induced by its interaction with the gold surface plasmons for the detection of tiny amounts of protein in solution under physiological conditions. The system we investigated is based on 10 and 5 nm diameter gold NPs coupled (via a biotin-streptavidin linker) to the FITC dye and to a specific protein antibody. The interaction of the fluorophore with the gold surface plasmon resonances, mainly occuring through quenching, affects the excited state lifetime that is measured by fluorescence burst analysis in standard solutions. The binding of protein to the gold NPs through antigen-antibody recognition further modifies the dye excited-state lifetime. This change can therefore be used to measure the protein concentration. In particular, we have tested the nanodevice measuring the change of the FITC excited-state lifetime after the binding of the model protein bovine serum albumin (BSA); then we have applied the nanoassay to the detection of traces of p53 protein, a marker for

early cancer diagnosis and prognosis, both in standard solutions and in total cell extracts. The selectivity of the construct with respect to other globular proteins has been also addressed. The data indicate that the FITC excited-state lifetime is a very sensitive parameter in order to detect tiny amounts of protein in solution with an estimated limit of detection of about 5 pM, mostly determined by the statistical accuracy of the lifetime measurement.

In the second part of the project (discussed in Chapter 4) we focused on the exploitation of anisotropic gold nanoparticles as probes in cellular imaging. We have then studied the Two-Photon Luminescence (TPL) properties by focusing on gold nanorods, that can easily be obtained by synthesis with the standard surfactant CTAB (cetyl trimethulammonium bromide).

The synthesis of asymmetric branched gold nanoparticles, obtained using for the first time in the seed growth method approach a zwitterionic surfactant, laurylsulphobetaine (LSB), has been developed by the University of Pavia (Prof. P.Pallavicini, General Chemistry Department). It has been shown that LSB concentration in the growth solution allows to control the dimension of the NPs and the SPR position, that can be tuned in the 700-1100 nm Near Infrared range.

I have analyzed samples synthesized at increasing levels of surfactants with several structural techniques to obtain a complete structural and spectroscopic characterization: the absorption spectra in the UV-Visible region, TEM images, Fluorescence Correlation Spectroscopy (FCS) and Dynamic Light Scattering (DLS) experiments. From the analysis of these data I have reached information on the nanoparticles shapes, dimensions and aggregation.

Three different populations have been found in the LSB seeded NPs: nanospheres with diameter lower than 20 nm, nanostars characterized by large trapezoidal branches, and asymmetric branched nanoparticles with high aspect ratio.

For imaging applications of the NPs, we have undertaken a spectroscopic characterization under two photon excitation (TPE): the dependence of the TPL intensity on the power, wavelength and polarization of the incident light intensity was studied.

TPL was finally exploited to study the cellular uptake of the nanoparticles by different cell lines (macrophages and HEK cells).

Chapter 1

Metal nanoparticles

1.1 Nanoscaled materials

The research in nanoscaled matter began to grow exponentially when it became recognized that the properties of materials change drastically as their sizes decrease from the bulk to small clusters of atoms [1]. Suitable control of the properties of nanometer-scale structures can lead to new science as well as new devices and technologies [2]. Two principal factors cause the properties of nanoscaled materials to differ significantly from their behavior in bulk. First, the increased relative surface area and, second, the size dependent properties begin to dominate when matter is reduced to the nanoscale. Not only these effects change the chemical reactivity and strength drastically, but also the electrical, optical and thermal response of the matter.

The most striking phenomenon encountered in metal nanoparticles are electromagnetic resonances due to the collective oscillation of the conduction electrons. These so-called localized Surface Plasmon Resonances (SPR) induce a strong interaction with light; the wavelength at which this resonance occurs depends on the local environment and on the shape, size and orientation of the particle. The fundamental aspects and the potential technological applications of SPR have been widely investigated in the past decade, during which metal nanoparticles have been used for catalysis, sub-wavelength optical devices, surface enhanced Raman spectroscopy, diagnostic application, biological imaging, sensing and for cancer treatment. Moreover, the compatibility of NPs and biological systems, proteins and oligonucleotides is well established. Small particles of different sizes and shapes have been shown to be suitable markers, contrast agents (for instance in optical coherence tomography) and therapeutic agents for biomedical applications [3],[4],[5]. For all these issues, it is advantageous to be able to tune the particle plasmon resonance to the near-infrared region between 650 and 900 nm, where water and hemoglobin have their lowest absorption coefficient [6],[7],[8]. This tunability

is provided by engineering the shape (principally spheric and elliptic) and the dimension of the particles.
The following sections describe briefly the significant properties and the origin of the plasmon resonances in spherical and ellipsoidal metal nanoparticles.

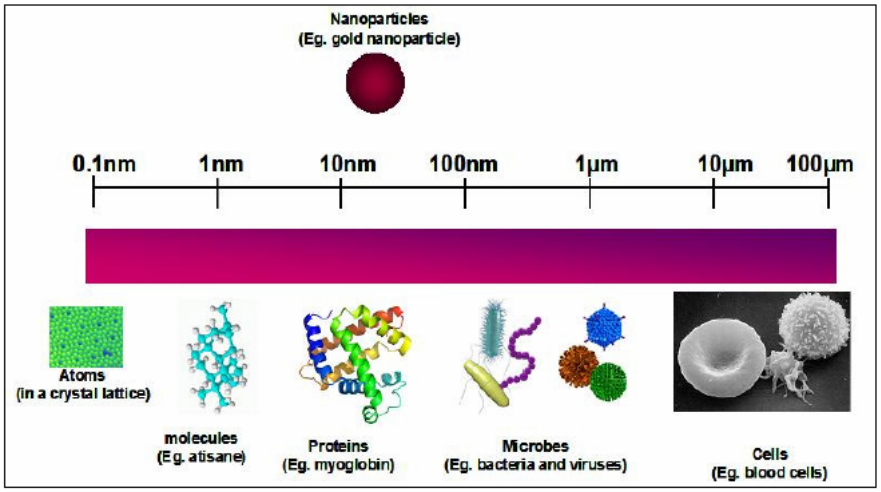

Figure 1.1: *Nanoparticles in comparison with other biological entities. From [9].*

1.2 Historical overview: gold through the centuries

The fact that gold compounds could impart a red color to the objects was well known; Egyptian manuscripts from the Greco-Roman era refer to it [10]. The Egyptians, Greeks and Romans used many colored pigments for the decoration of their buildings, ceramics and glass-ware. The use of gold and silver particles in glassblowing is evident in the famous Lycurgus Cup (Fig.1.2). Gold NPs scatter green and transmit red light so the cup appear to be red or green depending on the position of the light source (inside or outside) [11]. Chemical analysis of the Lycurgus cup shows that it is similar to most other Roman glass, but it contains very small amounts of gold (about 40 parts per million) and silver (about 300 parts per million). In figure 1.2 (right), a TEM image, a silver-gold alloy coming from a sample of the Lycurgus cup is clearly visible [12]. The crystalline nature of the Ag/Au particles and their fine dispersion in the glass suggests that this colloidal metal was precipitated out from solution by heat treatment.

In the Middle Ages, chemistry developed mostly through the protoscience of Alchemy. Alchemical processes required the construction of scientific apparatus and the invention of many laboratory techniques like heating, refluxing, extraction, sublimation and distillation to treat metals with various chemical substances [13]. In the early thirteenth

century the improvement of distillation methods resulted in the discovery of the mineral acids which greatly increased the power of the alchemist to dissolve substances and to carry out reactions in solution. The 'royal' solvent for gold was found to be "aqua regia", created by adding salt ammoniac (ammonium chloride) to aqua fortis (HNO_3) [14].

Figure 1.2: *Left: The Lycurgus cup dates from the fourth century AD. In reflected light (daylight) the glass appears to be green, but when light is transmitted from the inside of the vessel it is red [11]. Right: TEM image of a Ag/Au alloy [12]*

Paracelsus (16th century), used gold in the preparation of drugs to relieve suffering, as a cure for ailments and particularly for heart disorders. Recipes for the preparation of medicinal colloidal gold solutions were well known by the early seventeenth century [14]. Closely to this use in medicine, colloids were employed to produce ruby glass; the florentine priest Antonio Neri, in 1612, wrote the first treatise about ruby glasses. A contemporary chemist, Johann Kunckel, published his 'Ars Vitraria Experimentalis', which has been a standard treatise on glass technology for many years. It concerns the production of ruby glass by the use of the purple precipitate, referred to as the 'Purple of Cassius' because in 1685 a doctor called Andreas Cassius published a basic alchemical work "De Auro", where he described a method for the precipitation of gold [10].

A more scientific approach to colloidal gold

The first scientific study of metal nanoparticles is dated back to the seminal work of Michael Faraday around 1850. He was the first to recognize that the red colour of gold colloids was due to the minute size of the Au particles and that one could turn the preparation to blue by adding salt to the solution. He obtained gold colloids reducing $AuCl_4^-$ by phosphorus, following a procedure already reported by Paracelsus in the 16th century. Faraday's discovery that metals could form colloids was a breakthrough, although the importance of his observations was not fully realized at that time; today his studies are

generally considered to mark the foundations of modern colloid science [15] [16]. The word "colloid" was first introduced by a London colleague of Faraday, Thomas Graham (1805-1869), who is referred to as "the father of colloid chemistry". Subsequently the German physicist Gustav Mie (1869-1957) published in 1908 an important article on light scattering in matter, describing the optical properties of small metal particles; he calculated the absorbance of colloidal gold particles as a function of the particle size using classical electromagnetic theory.

In 1925 Richard Adolf Zsigmondy (1865-1929) was awarded by the Nobel price [17] for his demonstration of the heterogenous nature of colloid solutions and for the methods he used, which have since became fundamental in modern colloid chemistry. Zsigmondy prepared practically equally-sized red gold hydrosols by the reduction of gold chloride with formaldehyde in a weakly alkaline solution. Finally, he showed that colloidal gold particles have a negative electrical charge, which largely determined their stability. This charge can be screened or exchanged by adding salts resulting in an immediate particle aggregation whereby the system coagulates.

Since colloidal gold has a particle size falling below the resolution limit of the optical microscope, the world of colloids has been opened up to a detailed study with the invention of the electron microscope at the beginning of World War II [18]. An interesting investigation of various preparations of colloidal gold using the electron microscope as the main tool started in 1948 at Princeton University and the RCA Laboratories by John Turkevich and colleagues, who studied the reduction of gold salt with sodium citrate extensively. G. Frens used the citrate reduction method studied by Turkevich to control the size of gold particles ranging from 16 nm to 150 nm simply by varying the concentration of sodium citrate added to the solution during the nucleation of the particles [19]. The real renaissance of gold nanoparticles, however, started when M. Brust and coworkers reported a simple reductive method using the borohydride reduction of chloroauric acid in the presence of alkane thiols [20]: functionalized groups on gold colloids surfaces allow their incorporation in three dimensional networks and make them useful in a wide range of applications in the fields of sensors and molecular electronics.

1.3 Physical and chemical properties

Gold and silver are known for being generally inert and, especially gold, for not being attacked by O_2 to a significant extent; this makes AuNP and AgNP stable in ordinary conditions [21]. Gold nanoparticles are resistant also to strong oxidizing or highly acid environments, on the other hand "aqua regia" or solutions containing CN^- can immediately dissolve them [22]. Both Au and Ag are reactive with sulfur; in particular in the case of organic thiols, ligation to nanoparticles surface is particularly effective for

the contemporary presence of a σ type bound, in which sulfur is the electron density donor and the metal atom is the acceptor, and a π type bound, in which metal electrons are partially delocalised in molecular orbitals formed between the filled d orbitals of the metal and the empty d orbitals of sulfur[21]. Since solid to liquid transition begins at interfaces, a well known feature of nanometric particles is the lower melting temperature with respect to the bulk. For instance gold undergoes a decrease in melting temperature of about 400 °C going from 20 nm to 5 nm particles and about 50 °C going from the bulk to 20 nm particles.
When nanoparticles size becomes comparable to the de Broglie's wavelength of an electron at the Fermi energy (0.5 nm for gold and silver), quantum size effects on the optical properties of metal nanoparticles induce fluorescence emission, due to transitions between discrete electronic states [23].

Thermal conductivity is enhanced for small particles due to higher surface to volume ratio, and phonons energy become higher for very small particles [22].

Finally, when a metal particle decreases in size to become a nanoparticle or a nanocrystal, a larger proportion of atoms is found at the surface. This observation together with the fact that catalytic chemical reactions occur at surfaces leads to much more pronunced reactivity when a given mass of gold is used in nanoparticulate form compared to the case in which microscopic particles are used [22] [24].

1.4 Optical properties

Due to their metallic nature, AuNp and AgNp possess a huge number of easily polarizable electrons, that means strong interactions of the matter with light and high non-linear optical properties. [25],[26],[27],[28],[29]
As mentioned in section 1.1, the most striking phenomenon in metal NPs is the surface plasmon resonance (SPR), namely the coherent displacement of the conduction band electrons from their equilibrium positions around their positive ionic core, in the presence of a resonant electromegnetic wave (Figure 1.3).

These plasmon resonances give rise to the Surface Plasmon Absorption (SPA) band, which lays in the visible spectral window for gold and silver particles with size 2-100 nm and confers the characteristic bright yellow and red colour to AgNp and AuNp colloidal solutions respectively. Moreover, the large number of electrons involved in the SPA accounts for the incredibly high extinction cross section of these nanoparticles, which is 10^5-10^6 larger than that of organic chromophores [30]. Another general photonic peculiarity of AuNp and AgNp is their solid state behavior: in contrast to common molecular chromophores they are extremely high photostable and they fast convert light into heat. [8] [31]

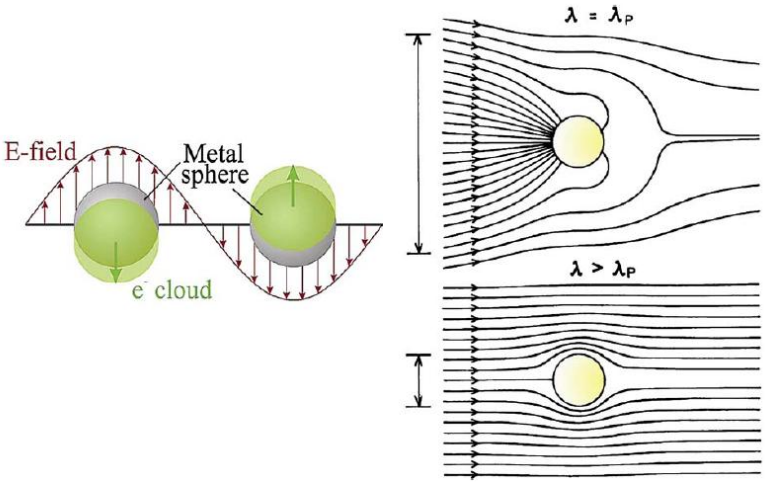

Figure 1.3: *Left: Schematic of plasmon oscillation for a sphere. From [8]. Right: Poynting vector or energy flow (lines) around a subwavelength metallic colloid illuminated at the plasmon wavelength (top) and at a wavelength longer than the plasmon wavelength (bottom). The vertical lines on the left indicate the diameter of the cross sections for absorption. This diagram does not show the energy flow due to scattered light. From [31]. A colloid is illuminated with light with a wavelength (λ) that matches the Plasmon resonance at λ_P (top) or with $\lambda \succ \lambda_P$ (bottom). The lines show the energy flow near the particle. For $\lambda = \lambda_P$, the colloid has an optical cross section much greater than its geometrical cross section. This effect gives rise to the energy flow into the particle, which results in the enhanced fields near the illuminated colloids. For $\lambda \succ \lambda_P$, the optical cross section can be similar to or smaller than the geometrical cross section (bottom), which is typical of organic fluorophores and semiconductor nanoparticles (quantum dot).*

Other than size, the SPA is primarily affected by particles shape and physical-chemical environment properties, including the reciprocal distance between particles.

Figure 1.4 shows the creation of a surface plasmon oscillation in a simple manner. The electric field of an incoming light wave induces a polarization of the free conduction electrons with respect to the much heavier ionic core of a spherical nanoparticle. A net charge difference occurs at the nanoparticle boundaries (i.e. at the surface) which in turn acts as a restoring force. In this manner a dipolar oscillation of the electrons is created with period T.

Figure 1.4(b) shows the SPA of 22, 48 and 99 nm gold nanoparticles [32] prepared in aqueous solution by the reduction of gold ions with sodium citrate [33] [34]. The absorption spectra of the different particles are normalized at their SPA maximum for comparison. The molar extinction coefficient is of the order of $1{\cdot}10^9 M^{-1}cm^{-1}$ for 20 nm nanoparticles and increases linearly with increasing volume of the particles [35]. Note that these extinction coefficients are three to four orders of magnitude higher than those

for the very strongly absorbing organic dye molecules [32].

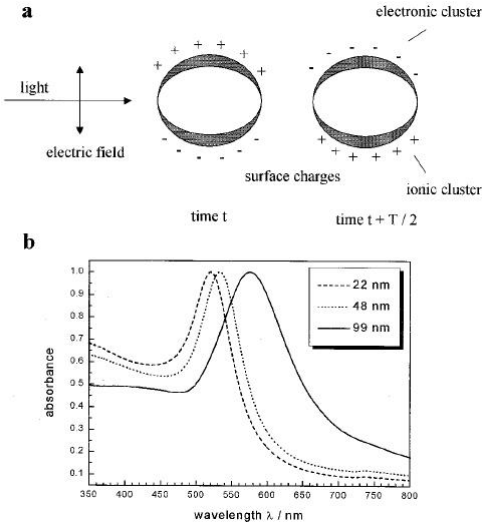

Figure 1.4: *Surface plasmon absorption of spherical nanoparticles and its size dependence. (a) A scheme illustrating the excitation of the dipole surface plasmon oscillation. The electric field of an incoming light wave induces a polarization of the (free) conduction electrons with respect to the much heavier ionic core of a spherical gold nanoparticle. A net charge difference is only felt at the nanoparticle boundaries (surface) which in turn acts as a restoring force. In this way a dipolar oscillation of the electrons is created with period T. This is known as the surface plasmon absorption. (b) Optical absorption spectra of 22, 48 and 99 nm spherical gold nanoparticles. The broad absorption band corresponds to the surface plasmon resonance. From [36]*

1.5 Mathematical origin of the plasmon resonances

The mathematical origin of the plasmon resonance was described by Mie in 1908 [37]. He solved the problem of light diffraction by a single sphere using classic electrodynamic theory.

1.5.1 Mie theory

Solving the problem of absorption and scattering of light by a small particle means solving Maxwell's equations with boundary conditions. The general formulation of the problem is shown in Figure 1.5.

Assuming harmonic time dependence of the light source, it is possible to rewrite Maxwell's equations into the Helmotz wave equation

$$\nabla^2\mathbf{E} + k^2\mathbf{E} = 0 \tag{1.1}$$

$$\nabla^2\mathbf{H} + k^2\mathbf{H} = 0 \tag{1.2}$$

where k is the wave number. Both the particle and the medium can be described by the dielectric function ϵ and the magnetic permeability μ (generally, the relative magnetic permeability of the materials under study is close to 1), that enter in the wave number as $k^2 = \omega^2\epsilon\mu$. At the boundary between the particle and the medium, ϵ and μ are discontinuous. It follows that the normal components of the field are discontinuous whereas tangential ones are continuous. For points $\mathbf{x}$ on the particle surface, we can write ($\hat{\mathbf{n}}$ is the normal vector)

$$[\mathbf{E}_2(\mathbf{x}) - \mathbf{E}_1(\mathbf{x})] \times \hat{\mathbf{n}} = 0 \tag{1.3}$$

$$[\mathbf{H}_2(\mathbf{x}) - \mathbf{H}_1(\mathbf{x})] \times \hat{\mathbf{n}} = 0 \tag{1.4}$$

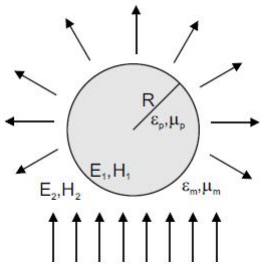

Figure 1.5: *Sketch of the problem as it is treated in section 1.5.1. A particle with optical constants ϵ_p and μ_p is embedded in a medium with optical constants ϵ_m and μ_m, and illuminated by a plane wave, which generates an electric field $\boldsymbol{E}_1$ and a magnetic field $\boldsymbol{H}_1$ inside the particle. The particle radiates a scattered field in all directions, which leads, together with the applied fields, to an electric field $\boldsymbol{E}_2$ and a magnetic field $\boldsymbol{H}_2$ outside of the particle. From [38].*

Only restricted to spherical particles, this problem is exactly solvable as shown in 1908 by Gustav Mie [37] (a complete derivation of Mie theory is given by Bohren and Huffman [31]), and the scattering matrices can be derived. From these information, e.g., the direction and polarization dependence of the scattered light can be extracted. An important parameter that can be also calculated is the cross section, a geometrical quantity that relates the incident light to the scattered, absorbed or extincted power. The absorption, scattering and extinction cross sections (σ_{abs}, σ_{sca} and σ_{ext} respectively) [39] [40],[41],[31] for an arbitrary spherical particle with dielectric function ϵ_p are defined as:

$$\sigma_{sca} = \frac{P_{sca}}{I_{inc}} \qquad \sigma_{abs} = \frac{P_{abs}}{I_{inc}} \qquad \sigma_{ext} = \frac{P_{ext}}{I_{inc}} \tag{1.5}$$

Since the extincted power is the sum of the scattered and absorbed power, the absorption cross section is simply

$$\sigma_{abs} = \sigma_{ext} - \sigma_{sca} \tag{1.6}$$

where the scattering and extinction cross sections are:

$$\sigma_{sca} = \frac{2\pi}{k^2}\sum_{n=1}^{\infty}(2n+1)(|a_n|^2 + |b_n|^2) \tag{1.7}$$

$$\sigma_{ext} = \frac{2\pi}{k^2}Re(a_n + b_n) \tag{1.8}$$

where a_n and b_n are given by

$$a_n = \frac{m\psi_n(mx)\psi_n^{'}(x) - \psi_n(x)\psi_n^{'}(mx)}{m\psi_n(mx)\xi_n^{'}(x) - \xi_n(x)\psi_n^{'}(mx)} \tag{1.9}$$

$$b_n = \frac{\psi_n(mx)\psi_n^{'}(x) - m\psi_n(x)\psi_n^{'}(mx)}{\psi_n(mx)\xi_n^{'}(x) - m\xi_n(x)\psi_n^{'}(mx)} \tag{1.10}$$

in equations 1.9 and 1.10 ψ and ξ are the Ricatti-Bessel functions of order n [31], x=kR is a size parameter (R is the radius of the particle) and m=$\sqrt{\epsilon_p/\epsilon_m}$ is the square root of the ratio between the dielectric functions of the particle ϵ_p and of the medium ϵ_m. The prime indicates a derivation to the parameter in parentheses. Equations 1.9 and 1.10 signifies that the electric and magnetic fields inside the sphere can be expressed as a multipolar series of spherical armonics with different symmetry, identified by the multipolar order n (n equal to 1 corresponds to dipolar sphere excitation, n equal to 2 corresponds to quadrupolar oscillation and so on).
The x parameter determines if the sphere is in the quasistatic (dipolar: R << λ then $|x|$ <<1) or in the dynamic regime (multipolar: R $\approx \lambda$). This type of size dependence is called "extrinsic size effect" in contrast to the "intrinsic size effect", that is due to the metal dielectric constant dependence on the size, discussed in the following.

In order to calculate the cross section, we need the dielectric function of the particle. The dielectric function of metals can be calculated using models such as the Drude model [42]: it treats the electrons as simple harmonic oscillator subject to the driving force of applied electromagnetic field. The basic picture of the properties of metals in the framework of this theory is a gas of independent, point-like electrons. These electrons move freely in between independent collisions with unspecified collision centers (lattice ions, other electrons, defects, phonons, etc.), which occur with an average rate of γ_0 that is the inverse of the so-called electron relaxation time τ. The resulting equation is:

$$\epsilon_p(\omega) = \epsilon_\infty - \frac{\omega_p^2}{\omega(\omega + i\gamma_0)} \approx \epsilon_\infty - \frac{\omega_p^2}{\omega^2} + i\frac{\gamma_0\omega_p^2}{\omega^3} \tag{1.11}$$

In eq. 1.11, ω_p is the so-called plasma frequency and ϵ_∞ includes the contribution of the bound electrons to the polarizability. The plasma frequency is given by $\omega_p = \sqrt{ne^2/\epsilon_0 m^*}$ with n and m^* being the density and effective mass of the conduction electrons, respectively.
However, the complex electronic structure of metals is not described very accurately by this model, so most calculations involving metals use a dielectric function known from measurements. The measurements by Johnson and Christy [43] are generally considered to be most reliable and were obtained on metal films under high vacuum conditions

Figure 1.6 shows a comparison between the Drude model and the values measured by Johnson and Christy [43]: whereas the low energy values are well described by the Drude-Sommerfeld model, additional contributions are present at higher energies (E>2 eV). The reason for this discrepancy is related to the excitation of electrons from deeper bands into the conduction band, the so-called interband excitations. An additional reason for the deviation from the Drude-Sommerfeld behavior is that the conduction band is increasingly non-parabolic for higher energies.

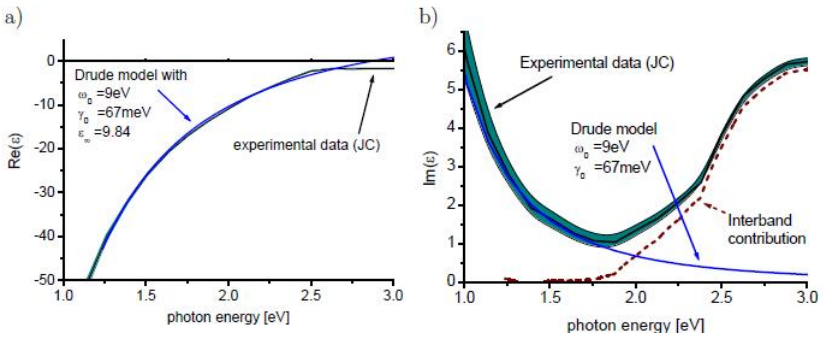

Figure 1.6: *(a) Real part of the dielectric function of gold; (b) imaginary part. Experimental data (JC) from Johnson and Christy (1972) [43] compared to calculated values using the quasi-free electron or Drude model with the parameters indicated in the graph. The shaded area around the experimental data indicates the measurement uncertainty. The interband contribution (broken line) is calculated from the difference of the experimental data to the Drude model. From [44]*

The effect of the dielectric constants of the metal and the surrounding medium on the polarizability is illustrated in the simulations in figure 1.7; the solid line shows the calculated extinction spectrum of a spherical Au particle with a diameter of 50 nm in water. The peak in the extinction is found at a wavelength of about 520 nm, i.e., green light is absorbed, giving the particles their red color. The spectrum of a Ag sphere of the same size in the same medium is also shown in Figure 1.7 (dashed line). The extinction

peak is found at a smaller wavelength (at 420 nm), a direct consequence of the different dielectric constants for Ag than for Au.
Changing the embedding medium to glass instead of water (i.e., ϵ_m from 1.45 to 1.33) causes a peak red shift for Ag by about 25 nm (see dash-dotted line). The glass effectively screens the surface charges resulting in a smaller restoring force and thus to a lower resonance frequency.

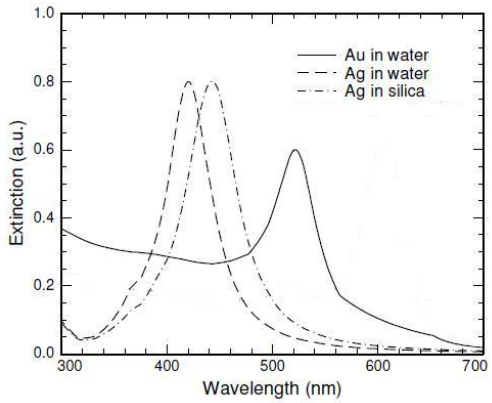

Figure 1.7: *Calculated extinction spectra of Au spheres (solid line), Au rods (dotted line) and Ag spheres in water (dashed line) or silica (dash-dotted line). The refractive index of silica is taken as 1.45, the radius of the particles is 25 nm. The rods have aspect ratio of 2 with a length of 80 nm. Ref [45]*

1.6 Mie-theory approximations

Although Mie theory gives an exact solution for any spherical particle, in some cases it can be useful to obtain simpler formulas for the cross sections using some approximations, as discussed below.

1.6.1 Size dependence: small particles

For nanoparticles much smaller than the wavelength of light only the dipole oscillation contributes significantly to the extinction cross-section. In this regime, which is called the Rayleigh limit, it is required for the size parameter x=kR that [46],[16],[39],[40],[31]

$$|m|\, x << 1 \tag{1.12}$$

This assumption physically means that the electric field is constant over the size of the particle and that any change in the electric field propagates across the particle in a time much shorter than the oscillation period of the electromagnetic field. The Mie theory then reduces to the following relationship (dipole approximation):

$$\sigma_{ext}(\omega) = 9\frac{\omega}{c}\epsilon_m^{3/2}V\frac{\epsilon_2(\omega)}{[\epsilon_1(\omega)+2\epsilon_m]^2+\epsilon_2(\omega)^2} \tag{1.13}$$

where V is the particle volume, ω is the angular frequency of the exciting light, c is the speed of light, and ϵ_m and ϵ_p= ϵ_1+i$\epsilon_2(\omega)$ are the dielectric functions of the surrounding medium and the particle material respectively. While the first is assumed to be frequency independent, the latter is complex and is a function of the energy. The resonance condition is fullfilled when $\epsilon_1(\omega)$=-2ϵ_m, if ϵ_2 is small or weakly dependent on ω [39]. This resonance is independent of particle size.
The dipole approximation is also often described as the quasistatic approximation, which assumes that the entire surface of the nanoparticle is experiencing a constant electric field. The above equation has been used extensively to explain the absorption spectra of small metallic nanoparticles in a qualitative as well as quantitative manner [39].

1.6.2 Size dependence: larger particles

For larger nanoparticles (greater than about 20 nm in the case of gold), where the dipole approximation is no longer valid, the plasmon resonance depends explicitly on the particle size as the size parameter x (eq. 1.7-1.10)is a function of the particle radius r.

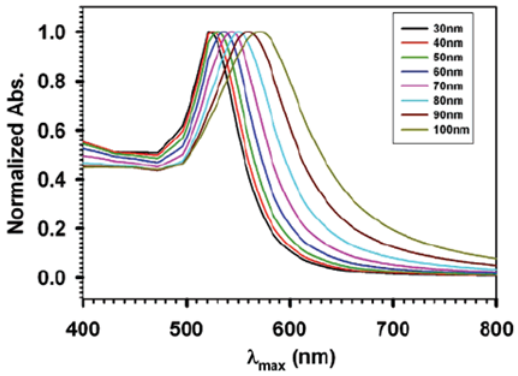

Figure 1.8: *Absorption spectra for increasing radius.*

The larger the particles become, the more important are the higher-order modes in eq. 1.7 as the light can no longer polarize the nanoparticles homogeneously. These higher-order modes peak at lower energies and therefore the plasmon band red shifts with increasing particle size [39],[40]. At the same time, the plasmon bandwidth increases with increasing particle size [39],[40]. This is illustrated experimentally from the spectra

shown in Figure 1.8. As the optical absorption spectra depend directly on the size of the nanoparticles, this is regarded as an *extrinsic size effect* [39].

1.7 Intrinsic size effect

The situation concerning the size dependence of the optical absorption spectrum is more complex for smaller nanoparticles for which only the dipole term is important. As can easily be seen from equation 1.13, the extinction coefficient does not depend on the particle dimension. However, a size dependence is observed experimentally [39],[40]. Figure 1.9 shows the absorption spectra of four different size gold nanoparticles where λ_{max} of the plasmon absorption redshifts with increasing particle diameter.

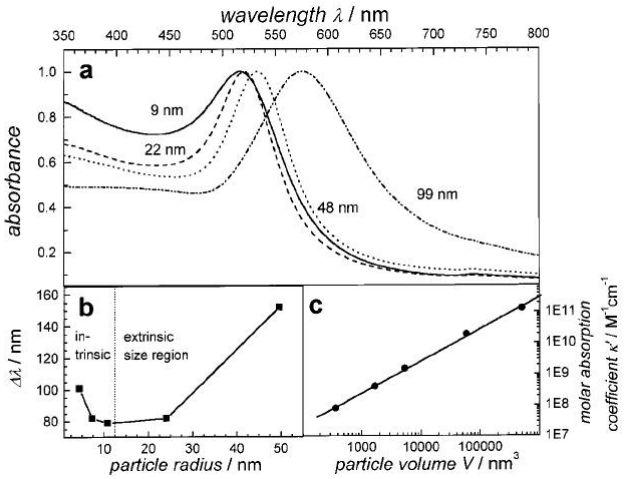

Figure 1.9: *Size effects on the surface plasmon absorption of spherical gold nanoparticles. The UV-vis absorption spectra of colloidal solutions of gold nanoparticles with diameters varying between 9 and 99 nm show that the absorption maximum red-shifts with increasing particle size (a), while the plasmon bandwidth follows the behavior illustrated in (b). The bandwidth increases with decreasing nanoparticle radius in the intrinsic size region and also with increasing radius in the extrinsic size region as predicted by theory. In panel (c) the extinction coefficients of these gold nanoparticles at their respective plasmon absorption maxima are plotted against their volume on a double logarithmic scale. The solid line is a linear fit of the data: a linear dependence is observed, in agreement with the Mie theory. Ref [47]*

Furthermore, it is seen that the plasmon absorption bandwidth decreases with increasing particle size and then increases again with a minimum for the 20 nm nanoparticles (Figure 1.9b). A modification to the Mie theory require that the dielectric function is assumed to become size-dependent when the diameter of the NP is smaller than the mean free path of the conduction electrons, $[\epsilon = \epsilon(\omega, r)]$ [48]. This means the absorption cross section to be size-dependent within the dipole approximation and thus is regarded as the *intrinsic size effect*.

Contrary to the extrinsic size effects on the extinction cross section, that are simply deduced from electromagnetic theory, intrinsic size effects are only due to the dependence of metal dielectric constant on the size [32]. In case of spherical AuNP and AgNP the extrinsic size effects are perceptible for sized above 20 nm in diameter and become important for a size $\geq$ 60 nm, while intrinsic ones appear in the SPA for a size smaller than 20 nm.

In general, the optical properties of noble metals are determined by conduction electrons and d-band electrons. Therefore the dielectric constant in the UV-Vis-NIR regime is composed of two terms [39]:

$$\epsilon_{\infty}(\omega) = 1 + \chi_s(\omega) + \chi_d(\omega) \tag{1.14}$$

where $\chi_d(\omega)$ is the contribute of d-bands electrons and $\chi_s(\omega)$ is that of s-band conduction electrons and can be expressed by a simple Drude-Sommerfield model:

$$\chi_s(\omega) = -\frac{\omega_p^2}{\omega^2 + \Gamma_{\infty}^2} + i\frac{\omega_P^2 \Gamma_{\infty}}{\omega(\omega^2 + \Gamma_{\infty}^2)} \tag{1.15}$$

where Γ_{∞} is the bulk metal damping frequency. According to the Matthiessen rule, conduction electron damping frequency of bulk metals is the sum of three main independent processes: electron-electron scattering (τ_{e-e}), electron-phonon scattering (τ_{e-p}) and electron-defects scattering (τ_{e-d}) [49]:

$$\Gamma_{\infty} = \frac{1}{\tau_{e-e}} + \frac{1}{\tau_{e-p}} + \frac{1}{\tau_{e-d}} \tag{1.16}$$

For metal particles with nanometric size the usual scattering processes change and new contributes appear, mainly due to surface effects. The dominant process consist of electron scattering at particle surface, that is no more negligible when conduction electrons mean free path ($\approx$ 45 nm for Au and Ag) becomes comparable to particle size. This scattering contributes overshadow other phenomena originated by changes in the phonons spectra, quantum size effects, changes in the phonon-electrons coupling for the high surface charge during plasmon oscillation and so on. Usually surface scattering produces the complete quenching of SPA in AuNP and AgNP smaller than about 2 nm and 1.5 nm respectively [22]. The most common way to account for the surface effect on the damping frequency Γ consists in expressing the Matthiessen formula as a size equation [39], [47]:

$$\Gamma(r) = \Gamma_{\infty} + A\frac{v_F}{r} \tag{1.17}$$

where v_F is the velocity of the electrons at the Fermi energy and A is an empirical adimensional parameter usually close to 1, used to account for some factors affecting the

width for the SPA in specific cases. When replacing Γ_∞ with $\Gamma(r)$ in equation 1.15 two terms can be isolated in the expression of the dielectric constant [39]:

$$\epsilon(\omega, r) = \epsilon_\infty(\omega) + \left[\omega_P^2 \left(\frac{1}{\omega^2 + \Gamma_\infty^2} - \frac{1}{\omega^2 + \Gamma(r)^2}\right)\right] + i\left[\frac{\omega_P^2}{\omega}\left(\frac{\Gamma(r)}{\omega^2 + \Gamma(r)^2} - \frac{\Gamma_\infty}{\omega^2 + \Gamma_\infty^2}\right)\right] \tag{1.18}$$

The first is equal to the bulk constant and only the second accounts for the size effect on the dielectic response of nanometric object. For Au and Ag the $\epsilon_\infty(\omega)$ is experimentally known with high precision [43], hence correction of $\epsilon(\omega, r)$ for the size is straightforward.

This model gives the correct 1/r dependence [50][39] of the plasmon bandwidth as a function of size for nanoparticles described by the dipole approximation in the intrinsic size region (r $<$ 20 nm). The best advantages of this theory are that it provides a very good description for the dependence of ϵ_m on size and that the modification of the dielectric constant is done in a straightforward manner.

1.7.1 Specific phenomena influencing the surface plasmon absorption

Beside surface electronic scattering, a certain number of specific not negligible factors affect the SPA. When a single nanoparticle is polycrystalline, electron scattering at the grain boundaries increases the dumping frequency and produces slightly larger SPA [51]. High temperatures produce a small broadening of the SPA because the electron-electron scattering frequency is dependent on the Fermi-Dirac electron distribution as [47]:

$$\frac{1}{\tau_{e-e}} \propto (E - E_F)^2 \tag{1.19}$$

where E_F is the Fermi energy and E is the electron energy. Another specific effect influencing the SPA arises from the fact that metal nanoparticles change the overall dielectric properties of a material when they are present in high concentration. In general, the Mie theory is valid under strict conditions: the concentration of the nanoparticles in a solvent or solid matrix must be very low [39] [40], the individual particles have to be non-interacting and separated each other. Under these assumptions, the electric field created around one particle by the excitation of a surface plasmon resonance is not felt by the other surrounding particles. If the interparticle distances become smaller than the particle dimension or if aggregation occurs, the plasmon resonance red shifts and often a second absorption peak at a longer wavelength is observed [39].

The most intense and common specific mechanism influencing the surface plasmon absorption is called Chemical Interface Damping (CID) [39] [52]. It produces a sensible widening and red shift of the SPA when adsorbates are present on particle surface.

This holds both for chemisorption, as in case of thiols stabilized nanoparticles, and for physisorption, as in the case of citrate or alchilamine stabilized nanoparticles. The SPA broadening due to CID is explained considering that adsorbates offer new relaxation pathways for both excited electrons and phonons in the metal.

1.8 Shape-dependent properties : the Gans theory

If the size and the environment effects are clearly important, shape effects on the optical absorption spectrum of gold nanoparticles seem to be even more pronounced [53] [54] [55]. The plasmon resonance absorption band splits into two bands as the particles aspect ratio (i.e. the ratio between the long axis, lenght, and the minor axis, width) increases; moreover, the energy separation between the resonance frequencies of the two plasmon bands increases [40] [41] [31]. The high-energy absorption band at around 520 nm corresponds to the oscillation of the electrons perpendicular to the minor rod axis and is referred to as the transverse plasmon absorption. This absorption band is relatively insensitive to the nanorod aspect ratio [53] [54] [55] and coincides spectrally with the surface plasmon oscillation of the spherically symmetric nanocrystals. The other absorption band at lower energies is caused by the oscillation of the free electrons along the major rod axis and is known as the longitudinal surface plasmon absorption.

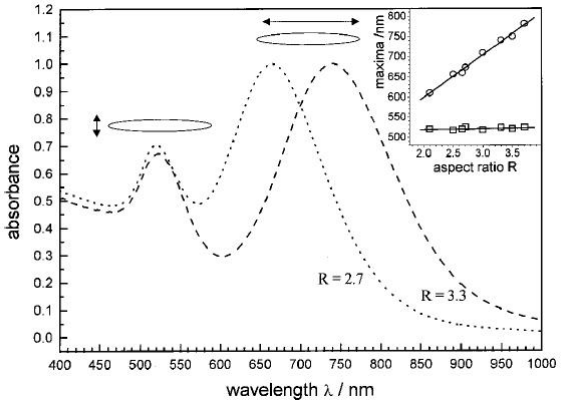

Figure 1.10: *Size-dependent surface plasmon absorption of gold nanorods. Optical absorption spectra of gold nanorods with mean aspect ratios of 2.7 and 3.3 are shown. The short-wavelength absorption band is due to the oscillation of the electrons perpendicular to the major axis of the nanorod while the long-wavelength band is caused by the oscillation along the major axis. The absorption bands are referred to as the transverse and longitudinal surface plasmon resonances respectively. The former is rather insensitive towards the nanorod aspect ratio in contrast with the longitudinal surface plasmon band which red shifts with increasing the aspect ratio. This is illustrated in the inset where the two band maxima (square for the, transverse mode; circle for the longitudinal mode) are plotted vs. the nanorod aspect ratio R. [36]*

Figure 1.10 (inset) shows the absorption spectra of two nanorod samples having aspect ratios of 2.7 and 3.3; the longitudinal plasmon band maximum (open circles) red shifts with increasing aspect ratio while the transverse absorption band maximum (open squares) does not change [53] [54] [55] [56].
The optical absorption spectrum of a collection of randomly oriented gold nanorods with aspect ratio R can be predicted using an extension of the Mie theory. Within the dipole approximation according to the Gans [57] treatment, the extinction cross-section σ_{ext} for elongated ellipsoids is given by the following equation [40] :

$$\sigma_{ext} = \frac{2\pi NV\epsilon_m^{3/2}}{3\lambda} \sum_j \frac{(\frac{1}{P_j^2})\epsilon_2}{[\epsilon_1 + \frac{1-P_j}{P_j}\epsilon_m]^2 + \epsilon_2} \tag{1.20}$$

whereby the P_j values are the depolarization factors that depend on the nanorod three axes A, B, and C as indicated in Figure 1.11. B and C correspond to the particle diameter (d), while the A axis represents the particle length (L).

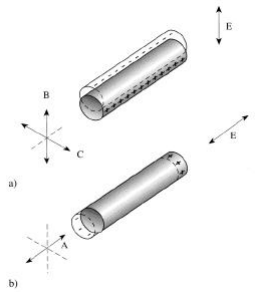

Figure 1.11: *Schematic representation illustrating the optical response of rodlike nano particles to an electric field E. Two oscillating modes can be possible: (a) the transverse oscillation along the B or C axis and (b) the longitudinal oscillation along the A axis [58].*

P_j for nanorods along A, B, and C axes are respectively

$$P_A = \frac{1-e^2}{e^2}[\frac{1}{2e}ln(\frac{1+e}{1-e}) - 1] \tag{1.21}$$

$$P_B = P_C = \frac{1-P_A}{2} \tag{1.22}$$

with

$$e = \sqrt{1-(\frac{d}{L})^2} = \sqrt{1-\frac{1}{R^2}} \tag{1.23}$$

where R = L/d is the aspect ratio. Link and coworkers [55] [59] calculated the absorption spectra of gold nanorods using Equation 1.20 for various aspect ratios starting

from the measured dielectric functions of gold [60]. When the medium dielectric constant was chosen to be 4, the maximum of the longitudinal plasmon band red-shifts 150 nm for the aspect ratio increasing from 2.6 to 3.6 (Figure 1.12).

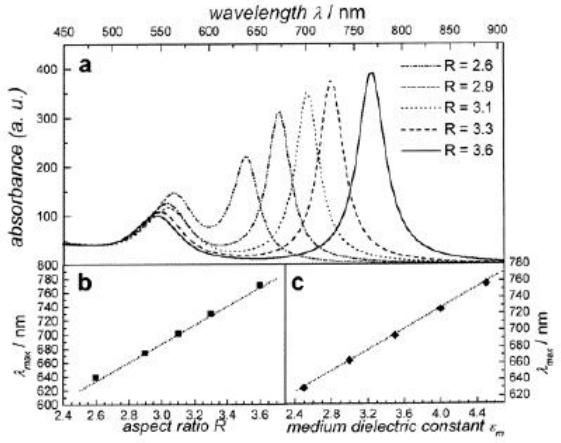

Figure 1.12: *Simulation of the surface plasmon absorption for gold nanorods of different aspect ratio by Link and coworkers. [55].*

Moreover, Figure 1.12 shows that the increase in the peak position of the longitudinal plasmon band with increasing nanorod aspect ratio follows a linear trend. The data shown here correspond to the absorption maxima of the longitudinal plasmon band as calculated in Figure 1.12b. The dotted line represents a plot of an equation derived by Link in order to predict the maximum of the longitudinal plasmon band λ_{max} [55]

$$\lambda_{max} = (33.34R - 46.31)\epsilon_m + 472.31 \tag{1.24}$$

It follows from Equation 1.24 that the maximum of the longitudinal plasmon resonance also linearly depends on the medium dielectric constant ϵ_m. Hence, with increasing the medium dielectric constant, there is also a red-shift of λ_{max} for a fixed aspect ratio (Figure 1.12 c with R=3.3).

The fact that gold nanorods exhibit a longitudinal SPR in the near-infrared has drawn interest of the biophysical community in the use of this particles in in-vivo study because of larger penetration depth of the laser light: in the region between 650-900 nm, $\geq$ 300 μm depending on tissue types.
Solid gold nanorods have several advantages over other contrast agents; their synthesis with various aspect ratios and tunable absorption wavelength in the near infrared region [61] [62] [8] is quite simple and well-established. The typical size of the nanorods (50-200 nm) is potentially useful in applications such as drug delivery and gene therapy. In addition, the biosafety of gold is well known and it has been used in vivo since the 1950's [63]

and recently the low cytotoxicity of gold nanoparticles in human cells has been studied in detail by Wyatt and coworkers [64].
Moreover, gold nanorods can be used as photo-absorbers in NIR and realize photothermal therapy. Thus, upon laser irradiation at the surface plasmon absorption band, the nanoparticles absorb energy and then immediately transfer it into heat. If the nanoparticles are incorporated or incubated with biomolecules, cells or tissues, heat causes the sharp increase on the local temperature around the nanoparticles and thus damages to the surrounding materials. This process is called photothermal destruction and can be used for disease or cancer therapy, providing a novel class of photo-absorber in medical applications. In fact, compared to the strongly absorbing Rhodimine 6G ($\epsilon = 1.16{\cdot}10^5 M^{-1}cm^{-1}$ at 530 nm [65]) dye molecules, gold nanoparticles absorb about 10^3 stronger (for nanospheres of 40 nm in diameter, $\epsilon = 2.74{\cdot}10^9 M^{-1}cm^{-1}$ at 530 nm, [61]).

Bibliography

[1] Nanotoxicology: nanotechnology grows up. *Science*, 304:1732–1734, 2004.

[2] C.N.R. Rao and A.K. Cheetham. Science and technology of nanomaterials: current status and future prospects. *J. Mater. Chem.*, 11:2887–2894, 2001.

[3] P. Alivisatos. The use of nanocrystals in biological detection. *Nat. Biotechnol.*, 22:47, 2004.

[4] J.G. Fujimoto. Optical coherence tomography for ultrahigh resolution in vivo imaging. *Nat. Biotechnol.*, 21:1361, 2003.

[5] J. Chen; F. Saeki; B.J. Wiley; H. Chang; M.J. Cobb; Z.Y. Li; L. Au; H. Zhang; M.B. Kimmey; X. Li and Y. Xia. Gold nanocages: bioconjugation and their potential use as optical imaging contrast agents. *Nano Lett.*, 5:473, 2005.

[6] R. Weissleder. A clearer vision for in vivo imaging. *Nat. Biotechnol.*, 19:316, 2001.

[7] R. Jin; Y. Cao; C.A. Mirkin; K.L. Kelly; G.C. Schatz and J. G. Zheng. Photoinduced conversion of silver nanospheres to nanoprisms. *Science.*, 294:1901, 2001.

[8] Kelly KL; Coronado E; Zhao LL; Schatz GC. The optical properties of metal nanoparticles: the influence of size, shape, and dielectric environment. *J Phys Chem B*, 107:668–677, 2003.

[9] Vijayalakshmi Kattumuri. Gold nanoparticles for biomedical applications: synthesis, characterization, in vitro and in vivo studies. *PhD Thesis*, 2006.

[10] L.B. Hunt. The True Story of Purple of Cassius. *Gold Bull.*, 9(4):134–139, 1976.

[11] F.E. Wagner; S. Haslbeck; L. Stievano; S. Calogero; Q.A. Pankhurst and K.P. Martinek. Before striking gold in gold-ruby glass. *Nature*, 407:691–692, 2000.

[12] D.J. Barber and I.C. Freestone. *Archaeometry*, 32:33–45, 1990.

[13] H.M. Leicester. The Historical Background of Chemistry. *Dover Publications, Inc.*, 1971.

[14] G.B. Kauffman. The Role of Gold In Alchemy. Part II. *Gold Bull.*, 18(2):69–78, 1985.

[15] M. Faraday. Experimental relations of gold (and other metals) to light. *Philos. Trans. R. Soc.*, pages 145–181, 1857.

[16] P. Mulvaney. Surface Plasmon Spectroscopy of Nanosized Metal Particles. *Langmuir.*, 12:788–800, 1996.

[17] R.A. Zsigmondy. Properties of Colloids. *Nobel Lecture.*, 11, 1926.

[18] J. Turkevich. Colloidal Gold Part I: Historical and Preparative Aspects, Morphology and Structure. *Gold Bull.*, 18(3):86–91, 1985.

[19] G. Frens. Controlled Nucleation for the Regulation of the Particle Size in Monodisperse Gold Suspensions. *Nature Phys. Sci.*, 241:19–22, 1973.

[20] M. Brust; M. Walker; D. Bethell; D. J. Schiffrin and R. Whyman. Synthesis of Thiol-derivatised Gold Nanoparticles in a Two-phase Liquid-Liquid System. *J. Chem. Soc.*, pages 801–802, 1994.

[21] Greenwood N.N.; Earnshaw A. Chemistry of the Elements. *Elsevier Science: Oxford*, 1997.

[22] Daniel ; Astruc. *Chemical Review*, 104:293–346, 2004.

[23] Zheng J.; Nicovich P.R.; Dickson R.M. *Annual Review of Physical Chemistry*, 58:409–431, 2007.

[24] Kvitek L.; Prucek R. *Journal of Material Science*, 2005.

[25] Lakowicz JR. Radiative decay engineering: biophysical and biomedical applications. *Anal Biochem.*, 298:1–24, 2001.

[26] Lakowicz JR; Shen Y.; DAuria S.; Malicka J.; Fang J.; Gryczynski Z.; Gryczynski I. Radiative decay engineering 2. Effects of silver island films on fluorescence intensity, lifetimes, and resonance energy transfer. *Anal Biochem.*, 301:261–277, 2002.

[27] Geddes C.D.; Aslan K.; Gryczynski I.; Malicka J.; Lakowicz JR. Radiative decay engineering. *In: Geddes CD, Lakowicz JR (eds) Topics in Fluorescent Spectroscopy vol 8: Radiative Decay Engineering. Springer Science-Business Media, Inc, New York*, page 405448, 2005.

[28] Geddes C.D.; Aslan K.; Gryczynski I.; Malicka J.; Lakowicz JR. Noble-metal surfaces for metal enhanced fluorescence. *In: Geddes CD, Lakowicz JR (eds) Topics in Fluorescent Spectroscopy vol 8: Radiative Decay Engineering. Springer Science-Business Media, Inc, New York*, page 365401, 2005.

[29] Lakowicz JR. Radiative decay engineering 5: metal-enhanced fluorescence and plasmon emission. *Anal Biochem*, 337:171194, 2005.

[30] Prasad P.N. *Nanophotonics. Wiley*, 2004.

[31] Bohren CF; Huffman DR. Absorption and Scattering of Light by Small Particles. *John Wiley and Sons, Inc., New York,*, page 530, 1983.

[32] Link S. and El-Sayed M.A. *J. phys. Chem. B*, 103:4212, 1999.

[33] Turkevich J.; Stevenson P.C.; Hillier J. *Discuss. Faraday Soc.*, 11:55, 1951.

[34] Turkevich J.; Garton G. and Stevenson P. C. *J. Colloid Sci., Suppl.*, 1:26, 1954.

[35] Link S. and El-Sayed M.A. *J. phys. Chem. B*, 103:8410, 1999.

[36] Link S.; El-Sayed M.A. Shape and size dependence of radiative, non-radiative and photothermal properties of gold nanocrystals. *Int. Reviews in Physical Chemistry*, 19 (3):409–453, 2000.

[37] Mie G. Articles on the optical characteristics of turbid tubes, especially colloidal metal solutions. *Annalen Der Physik.*, 25 (3):377–445, 1908.

[38] Meindert Alexander van Dijk. Nonlinear-optical studies of single gold nanoparticles. *PhD Thesis*, 2007.

[39] Kreibig U. and Vollmer M. Optical Properties of Metal Clusters. *Berlin : Springer*, 1995.

[40] Papavassiliou G.C. *Prog. solid st. Chem.*, 12:185, 1980.

[41] Kerker M. *The Scattering of Light and Other Electromagnetic Radiation (New York: Academic Press)*, 1969.

[42] Ashcroft N.W. and Mermin N.D. Solid State Physics. *Philadelphia, Pennsylvania: Saunders College*, 1976.

[43] P.B. Johnson and R.W. Christy. Optical-Constants Of Noble-Metals. *Phys. Rev. B*, 6(12):4370–4379, 1972.

[44] Carsten Soennichsen. Plasmons in metal nanostructures. *PhD Thesis*, 2001.

[45] Johanna Jacoba Penninkhof. Tunable plasmon resonances in anisotropic metal nanostructures. *PhD Thesis*, 2006.

[46] Henglein A. *J. phys. Chem.*, 97:8457, 1993.

[47] S. Link and M.A. El-Sayed. Simulation of the Optical Absorption Spectra of Gold Nanorods as a Function of Their Aspect Ratio and the Effect of the Medium Dielectric Constant. *J. Phys. Chem. B*, 103:3073–3077, 1999.

[48] U. Kreibig and C.V. Fragstein. The Limitation of Electron Mean Free Path in Small Silver Particles. *Z. Phys.*, 224:307323, 1969.

[49] Kittel C. Introduction to solid state physics. *Wiley*, 1996.

[50] Doremus R.H. *J. chem. Phys.*, 40:2389, 1964.

[51] Tang Y; Ouyang M. *Nature Materials*, 6:757–759, 2007.

[52] Llnaert T.; Mulvaney P.; Henglein A. *J.Phys.Chem.*, 97:679–682, 1993.

[53] Yu Y.; Chang S.; Lee C. and Wang C.R.C. *J. phys. Chem. B*, 101 (34):6661, 2005.

[54] Van der Zande B.M.I.; Bohmer M.R.; Fokkink L.G.J. and Schonenberger C. *J. phys. Chem. B*, 101:852, 1997.

[55] Mohamed M.B.; Ismael K.Z.; Link S. and El-Sayed M.A. *J. phys. Chem. B*, 101:852, 1997.

[56] Link S.; Mohamed M.B. and El-Sayed M.A. *J. phys. Chem. B*, 103:3073, 1999.

[57] Gans R. *Annln Phys.*, 47:270, 1915.

[58] Foss C.A.; Hornyak G.L.; Stockert J.A. and Martin C.R. *J. Phys. Chem*, 98:2963, 1994.

[59] Lisiecki I.; Billoudet F. and Pileni M.P. *J. Phys. Chem*, 100:4160, 1996.

[60] Lisiecki I. and Pileni M.P. *J. Am. Chem. Soc.*, 115:3887, 1993.

[61] Link S.; El-Sayed M.A. *J. Phys. Chem. B*, 103:8410, 1999.

[62] Murphy C.J.; Sau T.K.; Gole A.M.; Orendorff C.J.; Gao J.; Gou L.; Hunyadi S.E.; Li T. *J. Phys. Chem. B*, 109 (29):13857, 2005.

[63] Sherman A.I.; Ter-Pogossian M. *Cancer*, 6:1238, 1953.

[64] Connor E.E.; Mwamuka J.; Gole A.; Murphy C.J.; Wyatt M.D. *Small*, 1:325, 2005.

[65] Hao E.; Schatz G.C.; Hupp J.T. *Fluorescence*, 14:331, 2004.

Chapter 2

Principles

2.1 Basics of Fluorescence Optical Spectroscopy

Luminescence is the emission of light from any substances and occurs from electronically excited states [1]. It is divided in two categories: fluorescence and phosphorescence, depending on the excited state nature. Singlet excited states give rise to fluorescence; triplet states to phosphorescence. In the singlet state S_1 the electron e^- in the excited orbital is paired (of opposite spin) to the second e^- in the ground state, S_0, therefore the transition to S_0 ($S_1 \rightarrow S_0$) is allowed and occurs rapidly: 10^{-8} s ; so the typical fluorescence lifetime is 1-10 ns (for lifetime one means the average time a molecule spends in the excited state before coming back to the ground state). Phosphorescence is generated by transition from the triplet excited state T_1 in which the e^- has the same spin orientation of the e^- in S_0: than the transition $T_1 \rightarrow S_0$ is forbidden and its rate is slow compared with that of $S_1 \rightarrow S_0$, 10^{-3} - 10^0 s so the phosphorescence lifetime is from millisecond to second, significantly larger than that of fluorescence; this makes these two emission processes simply separable from a spectroscopic point of view [1]. Usually fluorescence comes from aromatic molecules: among the most used are the coumarins, the fluoresceines and the rhodamines. The first observation of fluorescence goes back to 1845 by Sir John Frederick William Herschel [2]. Fluorescence data are presented as emission spectra, i.e. a plot of the intensity vs. wavelength. This characteristic depends upon the chemical structure of the fluorophore and shows the structure due to the individual vibrational energy levels of the ground and the excited state. The absorption end emission of light can be described in terms of the Jablonsky diagram [3] (Figure 2.1).

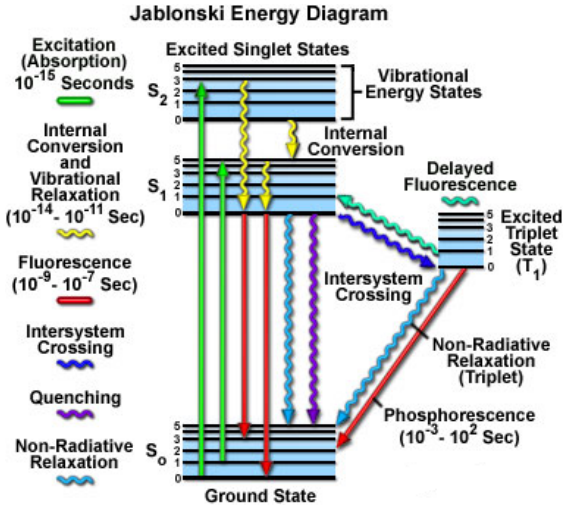

Figure 2.1: *Jablonski diagram. From www.olympusmicro.com.*

The ground state, the first and second exited singlet and the first excited triplet states are indicated respectively as S_0, S_1, S_2, and T_1; for each state there exist several vibronic levels (0, 1, 2, and so on). At room temperature the energy gap between S_0 and S_1 is too large for thermally population of S_1, so a light source is necessary to induce fluorescence. After the absorption of light ($h\nu_A$), that occurs in 10^{-16} s (i.e. instantaneously), several processes take place:

- *Internal conversion (IC)*: a fluorophore is excited to a higher vibrational level of either S_1 or S_2; after that the molecule relaxes rapidly to the lower vibrational level of S_1: this process takes place in 10^{-12} s.

- *Intersystem crossing (ICS)*: the fluorophore undergoes a spin conversion to T_1; the transitions $T_1 \rightarrow S_0$ are forbidden and have the low rates typical of phosphorescence. However an alternative route to de-excitation of T_1 is possible. In times of the order of few microseconds, the triplet state T_1 may convert back to an excited vibrational substate of S_1, from which the molecule decays in few picoseconds to the ground vibrational state of S_1. The decay from S_1 to an excited vibrational state of S_0 occurs instead in the nanosecond time range and is followed by a picosecond transition to the ground vibrational state of S_0 [1].

- *Quenching*: deexcitation is a consequence of interactions with solute molecules, especially with O_2.

- *Energy transfer*: dipole-dipole interactions between molecules can occur if their distance is less than few nm, causing energy transfer between fluorophores.

A direct consequence of the Jablonski diagram (figure 2.1) is that the emission spectrum is the mirror image of the excitation one. Other two features of fluorescence emission spectra deserve consideration: the *Stokes shift* [4] and the *Kasha's rule* [5]. Looking at the Jablonsky diagram in figure 2.1, it is clear that between absorption and fluorescence emission there is a loss of energy due to the relaxation to the lower vibrational level of S_1 by internal conversion; moreover the transition $S_1 \rightarrow S_0$ involves higher vibrational levels of S_0 that rapidly relax to the ground state resulting in a further loss of energy; as a result the emission of light takes place at lower energy (higher wavelengths) with respect to excitation. This phenomenon is called Stokes shift and was first observed by Sir George Gabriel Stokes in 1852 [4]. Moreover, the emission spectra are independent from excitation wavelength (Kasha's rule) [5]; this is because after absorption the fluorophores rapidly relax to the lowest vibrational state of S_1 from which any transition to S_0 starts. The relaxation is probably the result of the overlapping among numerous states of nearly the same energy.

2.1.1 Fluorescence lifetimes and quantum yields

The fluorescence lifetime τ and quantum yield Q are perhaps the most important characteristics of a fluorophore. The fluorescence quantum yield is the ratio of the number of photons emitted to the number absorbed: substances with large Q, such as rhodamines, display also the bright emission. The lifetime determines the time available for the fluorophore excited state to interact with its environment, and hence the amount of information that would be available from its emission. The meaning of τ and Q is best represented by a simplified Jablonski diagram (Figure 2.2), where the attention is focused on those processes responsible for the relaxation to the ground state. In particular, we are interested in the radiative (Γ) and non-radiative decay rate to S_0 (k_{nr}). The processes governed by Γ and k_{nr} both depopulate the excited state. The fraction of fluorophores which decay through emission, and hence the quantum yield, is given by:

$$Q = \frac{\Gamma}{\Gamma + k_{nr}} \tag{2.1}$$

Q is always < 1 due to the Stokes losses of energy and becomes close to the unity when $k_{nr} << \Gamma$.

Because τ is defined as the time a molecule spends in the excited state before relaxing to S_0, it is determined by the rate of all the processes that depopulate S_1:

$$\tau_f = \frac{1}{\Gamma + k_{nr}} \tag{2.2}$$

Due to the fact that fluorescence is a random process, the decay obeys an exponenatial trend and only few molecules relax exactly at a $t = \tau$, therefore τ is the average value

of the time spent in S_1: for a single experimental decay the 63% relax at $t < \tau$ and 37% at $t > \tau$.

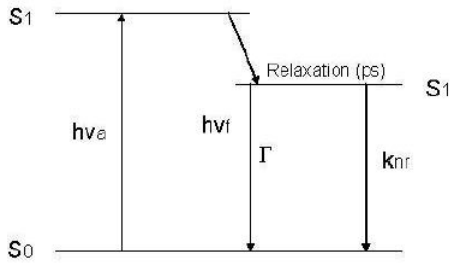

Figure 2.2: *A simplified Jablonski diagram.*

An opportunity to control the radiative rates arises from the interactions of fluorophores with nearby metallic surfaces or particles. Nearby metal surfaces can respond to the fluorophore oscillating dipole and modify the rate of emission and the spatial distribution of the radiated energy. The electric field felt by a fluorophore is affected by the interactions of the incident light with the nearby metal surface and also by interaction of the fluorophore oscillating dipole with the metal surface (excitation enhancement). Additionally, the fluorophores oscillating dipole induces a field in the metal (emission enhancement). These interactions can increase or decrease, depending on distance, the field incident on the fluorophore, its radiative decay rate and the spatial distribution of the radiated energy.

2.2 Radiative decay engineering

We refer to the interactions of fluorophores with metal particles as radiative decay engineering (RDE) because the radiative decay rates of the fluorophores are modified by placing them in close proximity to the metal [6] [7] [8].
Prior to describing the unusual effects of metal surfaces on fluorescence it is valuable to describe what we mean by Radiative Decay Engineering (RDE) and in particular spectral changes expected for increased radiative decay rates. Spectroscopists are accustomed to perform experiments using 5 to 10 Angstrom-sized fluorophores in macroscopic solutions, typically transparent to the emitted radiation. There may be modest changes in refractive index, such as for a fluorophore in a membrane, but such changes have only a minor effect on the fluorescence spectral properties. In such nearly homogeneous solution, the fluorophores emit into free space and are observed in the far field. The spectral properties are well described by Maxwells equations for an oscillating dipole radiating into free space. However, the interactions of electromagnetic radiation with physical objects can

be considerably more complex. Like a radiating antenna, a fluorophore is an oscillating dipole, whose near-field is characterized also by high spatial frequencies. The plasmonic resonances of nearby metal surfaces can couple to these components of the oscillating dipole and modify the rate of emission and the spatial distribution of the radiated energy. Therefore the electric field felt by a fluorophore is affected by interactions of the incident light with the nearby metal surface and also by interaction of the fluorophore oscillating dipole with the metal surface. In other words, the fluorophore-oscillating dipole induces a field in the metal. These interactions can increase or decrease the field incident on the fluorophore and the radiative decay rate. Depending upon the distance and the geometry, metal surfaces or particles can result in quenching or enhancement of fluorescence by factors of up to 1000 [9] [10] [11]. The effects of metallic surfaces on fluorophores are due to at least three mechanisms (figure 2.3).

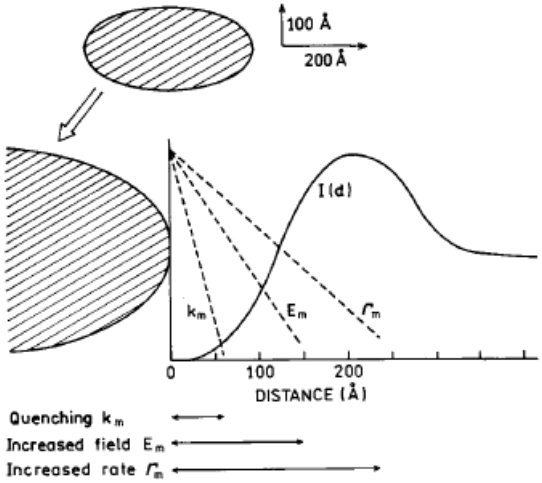

Figure 2.3: *Effects of a metallic particle on transitions of a fluorophore. Metallic particles can cause quenching (k_{nr}), can concentrate the incident light field (E_m), and can increase the radiative decay rate (Γ_m). Ref.[12]*

One is energy transfer quenching to these metals with a d^3 dependence (where d is the distance between the metal surface and the fluorophore) [10]. The quenching can be understood by damping of the dipole oscillators by the nearby metal. A second mechanism is an increase in emission intensity due to the extinction field amplification related to the so called 'tip effect' due to the surface roughness of the metal. However, another more important effect of the interaction between the metal surfaces and particles is possible. The nearby metal can increase the intrinsic radiative decay rate Γ of the fluorophore [12].

Assume that the presence of a nearby metal (m) surface increases the radiative rate

by an additional new term Γ_m (Fig. 2.4). In this case the quantum yield Q_m and lifetime τ_m of the fluorophore near the metal surface are given by

$$Q_m = \frac{\Gamma + \Gamma_m}{\Gamma + \Gamma_m + k_{nr}} \tag{2.3}$$

$$\tau_m = (\Gamma + \Gamma_m + k_{nr})^{-1} \tag{2.4}$$

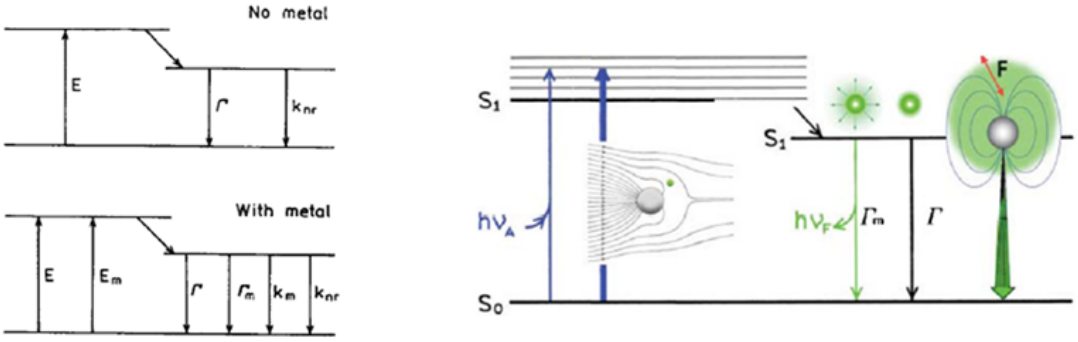

Figure 2.4: *Modified Jablonski diagrams which include metalfluorophore interactions. The thicker arrows represent increased rates of excitation and emission. Ref. [12]*

These equations result in unusual predictions for the fluorophore emission near a metal surface. As the value of Γ_m increases, the quantum yield increases while the lifetime decreases. We may observe then a variety of favorable effects due to metal particles, such as increased fluorescence intensities, increased photostability [1], and increased distances for FRET. We refer to these favorable effects as metal-enhanced fluorescence (MEF). The most dramatic relative changes are found for fluorophores with the lowest quantum yields. If Q = 1, then changing Γ_m has no effect. If Q is low, such as 0.1 in Fig. 2.5, the metal-induced rate Γ_m increases the quantum yield. At sufficiently high values of Γ_m, the quantum yields of all fluorophores approach 1. Examination of Fig.2.5 reveals that larger values of Γ_m/Γ are required to change the lifetime or quantum yield of low quantum yield fluorophores. This effect occurs because, for the same unquenched lifetime τ_0, lower quantum yields imply larger values of k_{nr}. Larger values of Γ_m are required to compete with the larger values of k_{nr}.

[1] less time at the excited state and as consequence lower bleaching

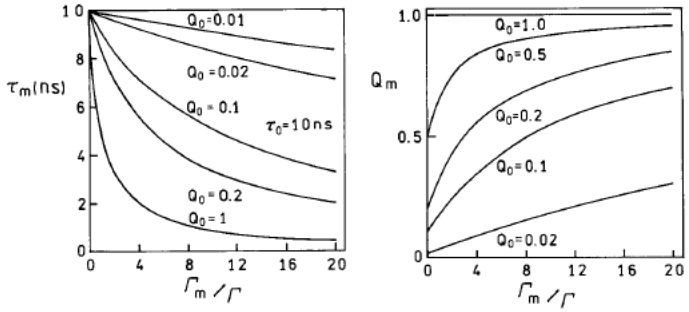

Figure 2.5: *Effect of an increase in the metal-induced radiative rate on the lifetime and quantum yields of fluorophores. To clarify this figure we note that for Q=0.5,* Γ*=5* 10^7*/s and* k_{nr}*=5* 10^7*/s. For Q=0.1,* Γ*=1·*10^7*/s and* k_{nr}*= 9·*10^7*/s. Ref.[12]*

2.2.1 Review of metallic surface effects on fluorescence

The possibility of altering the radiative decay rates, through the change of the excitation field phase, was demonstrated by measurements of the decay times of europium (Eu^{3+}) complex positioned at various distances from a planar silver mirror [13] [14] [15] [16]. The lifetime oscillates with distance but the decay remains a single exponential independent of the distance (Fig. 2.6). This effect can be explained by changes in the phase of the reflected field with distance and the effects of this reflected field on the fluorophore. A decrease in lifetime is found when the reflected field is in-phase with the fluorophores oscillating dipole. An increase in the lifetime is found if the reflected field is out-of-phase with the oscillating dipole. As the distance increases, the amplitude of the oscillations decreases. The effects of a plane mirror occur over distances comparable to the excitation and emission wavelengths. At short distances below 20 nm the emission is quenched. This effect is due to coupling of the dipole to oscillating surface plasmons.

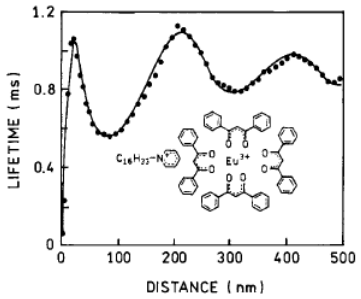

Figure 2.6: *Lifetime of* Eu^{3+} *ions in front of a Ag mirror as a function of separation between the* Eu^{3+} *ions and the mirror. The solid curve is a theoretical fit.Ref.[12]*

2.3 Two-photon excited fluorescence

Two-photon excitation was suggested for the first time by Maria Goppert-Mayer in 1931 [17]. Using the perturbation theory, she solved the quantum mechanical equations for light absorption and emission extending the quantum mechanical treatment to electronic processes that involve two annihilation (or two creation) operators: the two-photon absorption and emission processes. The transition probability of a two-photon electronic process was derived using second order, time-dependent, perturbation theory. The Maria Goppert-Mayer derivation proves that the probability of a two-photon absorption process is quadratically related to the excitation light intensity, and that it involves an interaction with a meta-stable intermediate state. This interaction occurs within the lifetime of this virtual state which is described as a non-linear superposition of all the vibro-electronic states. Both photons interact together to induce the transition from the ground state to the excited state (figure 2.7).

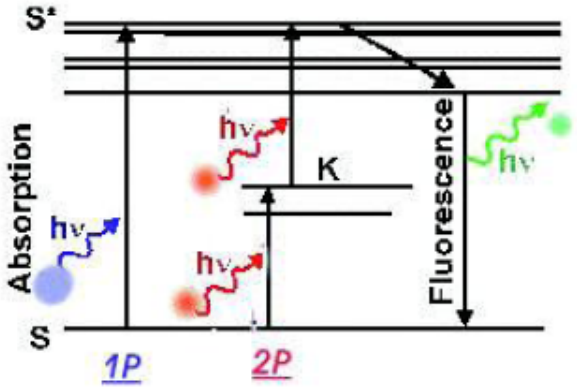

Figure 2.7: *Jablonski diagram for a two-photon absorption process, compared with one-photon absorption.*

Since this event depends on the fact that the two photons both interact with the molecule simultaneously (within 10^{-16} s), resulting in a quadratic dependence on the light intensity, rather than the linear dependence of conventional one-photon excitation, two photon excitation is often termed *non-linear*. The intensity-squared dependence guarantees the localized nature of two-photon excitation [18].
If the excited molecule is fluorescent, it can emit a single photon of fluorescence as if it were excited by a single higher energy photon: the fluorescence emission is independent of the excitation modality. The transition to an excited state is possible only if the energy of the exciting photon, hc=λ_1, is equal to the energy gap, ΔE, between the two states involved in the transition:

$$\Delta E = \frac{hc}{\lambda_1} \tag{2.5}$$

Since in TPE two photons are needed to induce the transition, they can combine and give rise to the absorption process only if they interact with the same molecule at the *same* time. The timescale for this process, given by the Heisemberg principle, is 10^{-15}-10^{-16} seconds [19] for photon energies in the visible-IR region. It is not necessary for the wavelengths of the two photons to be the same. They have just to satisfy the following relation:

$$\lambda_1 \approx \left(\frac{1}{\lambda_A} + \frac{1}{\lambda_B}\right)^{-1} \tag{2.6}$$

where λ_1 is the wavelength needed for OPE and λ_A and λ_B are the wavelengths of the photons involved in TPE. Usually, for practical reasons, the choice is to have $\lambda_A = \lambda_B = 2\lambda_1$ [20] (see Figure 2.7).
The application of multi-photon excitation to optical sectioning is based on the superlinear dependence of the molecular excitation rate on the laser irradiance. The probability for a molecule to absorb two or more photons depends on the probability, p_n, of finding two or more photons simultaneously in the volume occupied by the molecule. Let us suppose to have a cubic volume of side l completely filled by a laser beam of mean irradiance I and wavelength λ. If m is the mean number of photons in l^3, the mean energy in the cubic volume is given by:

$$\langle E_m \rangle = m\frac{hc}{\lambda} \tag{2.7}$$

since the cross sectional area is l^2 and the time required to a photon to pass through l^3 is l/c, the relation between the average number of photons m and the mean irradiance $\langle I \rangle$ is:

$$\langle I \rangle = \frac{\langle E_m \rangle}{l^2 l/c} = \frac{mhc^2}{\lambda l^3} \tag{2.8}$$

Since the interaction of the light with the molecule occurs on a volume of the order of the molecular volume which is related to the molar volume V_M and the Avogadro's number, N_A, as V_M/N_A, we can write the relation between the laser irradiance and the number of photons per molecular volume as:

$$I = \frac{mhc^2 N_A}{\lambda V_M} \tag{2.9}$$

or

$$m = \frac{\lambda V_M I}{hc^2 N_A} \tag{2.10}$$

This means that there exists a direct relation between I and m. If λ = 800 nm, I $\approx GW/cm^2$ and $V_M \approx 10^{-3} m^3$/ Mole we can estimate $m \approx 10^{-5}$.
A Poissonian distribution can then be used to calculate the probability to have a number n of photons per molecular volume at the same time, p_m(n):

$$p_m(n) = \frac{m^n}{n!} e^{-m} \tag{2.11}$$

Due to the low value of m the exponential function can be expanded in a Taylor series. For TPE, n = 2, and we compute:

$$p_2 = \frac{1}{2} m^2 \propto \Gamma I^2 \tag{2.12}$$

where Γ is a constant. This equation shows clearly the quadratic dependence of the excitation probability of a TPE process on the laser irradiance. The fluorescence emission (under TPE) depends quadratically on the excitation probability and linearly on the molecular (two-photon) cross section and is given by:

$$I_f(t) \approx \delta_2 I(t)^2 \approx \delta_2 P(t)^2 \left[\pi \frac{(N.A.)^2}{hc\lambda}\right]^2 \tag{2.13}$$

and thus

$$\langle I_f(t) \rangle = \frac{1}{T} \int_0^T I_f(t) dt = \delta_2 P(t)^2 \left[\pi \frac{(N.A.)^2}{hc\lambda}\right]^2 \frac{1}{T} \int_0^T P(t)^2 dt \tag{2.14}$$

where T is an arbitrary time interval for continuous wave (CW) excitation and T = $1/f_p$ for a pulsed laser and P(t) is the time shape of the pulse. For an IR square pulsed laser source with $\langle P \rangle = \tau_p f_p P(t) = \tau_p f_p P_{peak}$ we have:

$$\langle I_f(t) \rangle = \delta_2 \frac{< P >^2}{\tau_p^2 f_p^2} \left[\pi \frac{(N.A.)^2}{hc\lambda}\right]^2 \frac{1}{T} \int_0^{\tau_p} dt = \delta_2 \frac{< P >^2}{\tau_p f_p} \left[\pi \frac{(N.A.)^2}{hc\lambda}\right]^2 \tag{2.15}$$

while for a CW laser:

$$\langle I_f(t) \rangle = \delta_2 < P >^2 \left[\pi \frac{(N.A.)^2}{hc\lambda}\right]^2 \tag{2.16}$$

A comparison between equations 3.1 and 3.2 shows that, in order to operate at an excitation efficiency similar to that of a pulsed IR laser, a CW laser should operate at a power larger by a factor $(\tau_p f_p)^{-1/2}$. Thus an output of 10 W for a CW illumination

would correspond to 30 mW for a pulsed excitation with $f_p \approx 100$ MHz and $\tau_p \approx 100$ fs [21]. However this is not practically the case since the TPE cross-sections for fs pulsed excitation and for CW or picosecond, ps, excitation are not the same [2], and practically CW TPE has been reported also on biological samples [22]. We can compute the fluorescence rate by considering that the number of photon couples that a fluorophore absorbs per laser pulse is [23]:

$$n_a \propto \delta_2 \frac{< P >^2}{\tau_p f_p^2} \left[\frac{(N.A.)^2}{2\eta c \lambda} \right]^2 \tag{2.17}$$

where $\eta = h/2\pi$. The fluorescence rate is then theoretically given by 3.3 times the laser repetition rate. In order to obtain an optimal fluorescence rate and to keep at a minimum the ground state saturation, a laser repetition $f_p \approx 100$ MHz (i.e. ≈ 10 ns between two consecutive pulses) has to be used since the typical excited state life-time is $\tau_{lf} \cong 1$ ns. The ground state saturation occurs for the condition, $< I_f > \tau_{lf} \cong 1$. Moreover we must have $\tau_p \approx 10^{-13}$ s or $\tau_p << \tau_{lf}$ in order to minimize the probability of transitions from the first excited state to higher energy states [21].

2.3.1 One-photon and two-photon excitation Point Spread Functions

The three dimensional image plane distribution of the light collected from a point source in the focal plane, called Point Spread Function (PSF), is given by [24]:

$$h(u,v) = -i \frac{2\pi n A sin^2(\alpha)}{\lambda} exp\left(\frac{iu}{sin^2(\alpha)} \right) \int_0^1 J_0(v\rho) e^{-iu\rho^2/2} \rho d\rho \tag{2.18}$$

where λ is the light wavelength, n is the refractive index, N.A. = nsin(α) is the numerical aperture of the objective lens, A is the illumination area, J_0 is the zero-th order Bessel function and v and u are normalized optical coordinates defined respectively as:

$$\begin{aligned} v &= \frac{2\pi n r sin(\alpha)}{\lambda} \\ u &= \frac{2\pi n z sin^2(\alpha)}{\lambda} \end{aligned} \tag{2.19}$$

where r $=\sqrt{x^2 + y^2}$ is the distance from the z axis taken as the optical axis. Therefore the intensity PSF is:

[2] Under ps and CW excitation the molecule may suffer excitation to the first excited state and from this to a number of higher energy states.

$$PSF_{OPE}(u,v) = |h(u,v)|^2 = h(u,v)h^*(u,v) \tag{2.20}$$

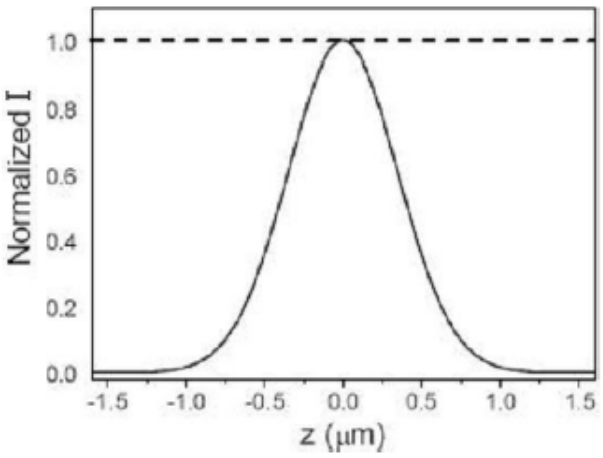

Figure 2.8: *Axial confinement of two-photon excitation PSF*

One-photon excitation does not provide optical sectioning capabilities since the total power released per cross-section of the laser beam along the optical axis is constant as can be verified from 2.20:

$$\int_{cross-section} |h(u,v)|^2 \, dv = constant \tag{2.21}$$

The optical sectioning is introduced by spatial filtering the emission in front of the detector. On the other hand, TPE is axially confined [25] since its intensity PSF is the square of 2.20:

$$PSF_{TPE}(u,v) = |PSF_{OPE}(u,v)|^2 \tag{2.22}$$

Therefore at fixed u, the integral over v assumes a half bell shape [26](see figure 2.8).

More precisely the excitation rate (proportional to PSF_{TPE}) falls off as the fourth power of the distance from the focal plane [21].

The TPE excited volume can be calculated by approximating the PSF_{TPE} as a three-dimensional Gaussian volume. This is not a volume with distinct walls but rather the volume over which most of the TPE laser excitation is released. Integrating over all space the three-dimensional Gaussian yields:

$$V_{TPE}^{G3D} = \pi^{3/2} \omega_{xy}^2 \omega_z \tag{2.23}$$

where ω_{xy} and ω_z are calculated as:

$$\omega_{xy} = \frac{0.320\lambda}{\sqrt{2NA}} \qquad if NA \leq 0.7$$
$$\omega_{xy} = \frac{0.325\lambda}{\sqrt{2NA^{0.91}}} \qquad if NA \succ 0.7 \tag{2.24}$$

$$\omega_z = \frac{0.532\lambda}{\sqrt{2}} \left[\frac{1}{n - \sqrt{n^2 - NA^2}} \right] \tag{2.25}$$

On the other hand, by integrating the Gaussian Lorentzian beam we obtain $V_{TPE}^{G-L} = \pi\omega_0^4/\lambda \cong 0.113\mu m^3$ for a 1.2 NA lens at $\lambda = 900$nm [27].

2.3.2 OPE versus TPE

For optical sectioning, i.e. for microscopy applications, the most important consequence of two-photon excitation, TPE, or non-linear excitation in general, is the fact that the molecular excitation is limited to a sub-femtoliter region around the focal plane. While in one-photon excitation, OPE, the excitation volume is not confined in the focal plane (see Figure 2.9).

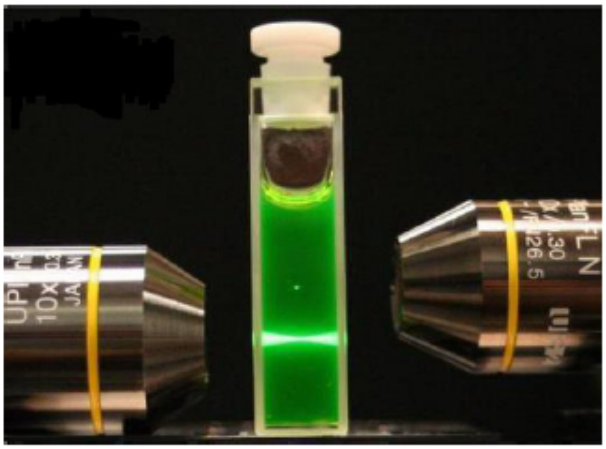

Figure 2.9: *Excited volumes by two photon laser source of λ= 760nm (upper) and by one photon laser source λ= 380nm (lower) in fluorescein solution.*

Under OPE the optical sectioning is obtained by spatial filtering the emission in front of the detector in the so called confocal detection scheme. The rejection of out of focus plane is achieved by placing a screen with a pinhole in front of the detector. The focal point of the objective lens forms an image onto the pinhole screen: the specimen plane and the pinhole screen are conjugated planes (and hence the name confocal). The ability of a confocal microscope to create sharp optical sections makes it possible to build 3D

renditions of the specimen.
The major drawback of using a lamp source when creating a point image onto the specimen is that only a minor fraction of the emitted photons are actually contributing to the image. Thus, to reduce the noise on the image, each pixel must be illuminated for a long time. In turn, this increases the length of time needed to create a point-by-point image and the photodamage. The solution is to use a light source of very high intensity. The modern choice is a laser light source, which has the additional benefit of being available in a wide range of wavelengths [28]. Unfortunately, fluorescence emission has not an infinite duration: molecules can undergo photobleaching. The phenomenon of photobleaching occurs when a fluorophore permanently looses the ability to fluoresce due to photon-induced chemical damage and covalent modification. Upon transition from an excited singlet state to the excited triplet state, fluorophores may interact with another molecule or with the light to produce irreversible chemical modifications. The triplet state is relatively long-lived with respect to the singlet state, thus allowing excited molecules more time to undergo chemical reactions with reactive components in the environment. This is the reason why reducing S_1-T transitions, inhibits photobleaching.
The average number of excitation and emission cycles that occur for a particular fluorophore before photobleaching is dependent upon the molecular structure and the local environment. The excitation power released per plane is independent of the focusing plane position along the optical axis. Thus, the major drawback of OPE confocal microscopy is the photobleaching of molecules in out of focus planes: when the focal plane moves to their plane they are no longer fluorescent. Since TPE requires the molecule to interact simultaneously with two photons (within 10^{-16}s), a high flux of photons (10^{24} photons cm^{-2} s^{-1} [21]) is needed at the focal plane. Only in the '90s, the development of mode-locked laser sources, that provide high peak power femtosecond pulses with a repetition rate of $\cong$ 100MHz and the introduction of high efficiency detectors (cooled photo-multiplier tubes, or single photon avalanche diodes), allowed laser scanning microscopy to take full advantage of TPE.
Non-linear excitation, in fact, offers a series of unique features that make TPE very suitable for many applications. First, the two-photon absorption bands of the dyes commonly used in biological studies are wider than their one-photon analogous, allowing the simultaneous excitation of multiple fluorophores with a single excitation wavelength [18]. Second, the TPE excitation light beam has a high penetration depth in thick specimens because IR radiation is scattered to a less extent than visible light by the tissues [21]. The scattering is the deflection of the light rays away from their original direction. Its angular distribution depends on the refractive index inhomogeneities, objects size and beam wavelength λ. For small objects in homogeneous media the scattering angu-

lar distribution is described by Rayleigh's law: it is isotropic and strongly λ-dependent $\propto \lambda^{-4}$ (for dipoles) $\propto \lambda^{-2}$ (for larger scatterer as in biological tissues). Third, excitation takes place only at the focal plane, due to the scaling of the probability of simultaneous photon absorption with the square of the light intensity. As a consequence TPE avoids the simultaneous absorption of photons outside the specimen drastically reducing both photo-toxicity and fluorophore bleaching [25]. Moreover the fact that excitation, and therefore emission, take place only in a tiny well defined volume, makes unnecessary to place a pin-hole aperture in front of the detectors for the purpose of rejecting the signal arising from out of focus region. This latter fact simplifes the optical set-up and reflects also in a remarkable reduction of the background noise [21].

Bibliography

[1] Lakowicz J.R. In principles of fuorescence spectroscopy. *Kluwer Academic Plenum Press, New York.*, 1999.

[2] Herschel Sir J.F.W. Uber den mechanisms des photolumineszenz von farbstoffphosphoren. *Phil. Trans. R. Soc. London*, 135:143–145, 1845.

[3] Jablonski A. On a case of superficial colour presented by an homogeneous liquid internally colourless. *Z. Phys.*, 94:38–46., 1935.

[4] Stokes G.G. On the change of refrangibility of light. *Phil. Trans.R. Soc. London*, 142:463–562., 1852.

[5] Kasha M. Characterization of electronic transitions in complex molecules. *Disc. Faraday Soc.*, 9:14–19., 1950.

[6] Geddes C.D.; Aslan K.; Gryczynski I.; Malicka J.; Lakowicz JR. Radiative Decay Engineering. *Topics in Fluorescent Spectroscopy*, 8:405448., 2005.

[7] Geddes C.D.; Aslan K.; Gryczynski I.; Malicka J.; Lakowicz JR. Noble-metal surfaces for metal enhanced fluorescence. *Topics in Fluorescent Spectroscopy*, 8:365401., 2005.

[8] Joseph R. Lakowicz. Plasmonics in Biology and Plasmon-Controlled Fluorescence. *Plasmonics*, 1:533., 2006.

[9] Glass A.M.; Liao P.F.; Bergman J.G. and Olson D.H. Interaction of metal particles with adsorbed dye molecules: Absorption and luminescence. *Optics Letts.*, 5(9):368370., 1980.

[10] Campion A.; Gallo A.R.; Harris C.B.; Robota H.J. and Whitmore P.M. Electronic energy transfer to metal surfaces: A test of classical image dipole theory at short distances. *Chem. Phys. Letts.*, 73(3):447450., 1980.

[11] Sokolov K.; Chumanov G. and Cotton T.M. Enhancement of molecular fluorescence near the surface of colloidal metal films. *Anal. Chem.*, 70:38983905., 1998.

[12] Joseph R. Lakowicz. Radiative Decay Engineering: Biophysical and Biomedical Applications. *Analytical Biochemistry*, 298:124., 2001.

[13] Drexhage K.H. Interaction of light with monomolecular dye lasers. *In Progress in Optics (Wolfe, E., Ed.)*, 70:161232., 1974.

[14] Amos R.M. and Barnes W.L. Modification of the spontaneous emission rate of Eu31 ions close to a thin metal mirror. *Phys. Rev. B*, 55(11):72497254., 1997.

[15] Barnes W.L. Fluorescence near interfaces: The role of photonic mode density. *J. Modern Optics*, 45(4):661699., 1998.

[16] Amos R.M. and Barnes W.L. Modification of spontaneous emission lifetimes in the presence of corrugated metallic surfaces. *Phys. Rev. B*, 59(11):77087714., 1999.

[17] Goppert-Mayer M. Uber elementarakte mit zwei quantensprunngen. *Ann. Phys. (Leipzig)*, 9:1273–295., 1931.

[18] C. Xu and W.W.Webb. *Journal of the Optical Society of America B*, 13(03):481., 1996.

[19] Louisell W.H. Quantum statistical properties of radiation. *Wiley New York*, 1973.

[20] Diaspro A. Methods in cellular imaging. *Oxford University Press, New York.*, 2001.

[21] Diaspro A. Confocal and two-photon microscopy: foundations, applications and advances. *John Wiley and Sons Inc., New York.*, 2002.

[22] Booth M.J. and Hell S.W. Continuous wave excitation two-photon fluorescence microscopy exemplified with the 647-nm ArKr laser line. *J Microsc*, 190:298–304, Jun 1998.

[23] Denk W.; Strickler J.H. and Webb W.W. Two-photon laser scanning fluorescence microscopy. *Science*, 248:73–76, Apr 1990.

[24] Born M. and Wolf E. Principles of optics. *Cambridge University Press, Cambridge.*, 1999.

[25] Nakamura O. Fundamental of two-photon microscopy. *Micr. Res. Tec.*, 47(3):165–171, 1993.

[26] Cannell M.B. and Soeller C. High resolution imaging using confocal and two-photon molecular excitation microscopy. *Proc. R. Microsc. Soc.*, 32:3–8., 1997.

[27] Williams et al. *Nature Biotechnology*, 21(11):1369–1377., 2003.

[28] Sheppard and Shotton. *Springer-Verlag New York Inc., New York*, 1997.

Chapter 3

Nano-bio sensors for protein detection

The interaction of the surface plasmons of gold nanoparticles (NP) a few nanometers in size with fluorophores can be used to engineer their fluorescence properties. This possibility can be exploited in principle to obtain nanodevices for protein-protein recognition. We studied different types of constructs based on gold NPs on which derivatives of fluorescein (FITC) were bound. The interaction of this fluorophore with the gold surface plasmon resonances, mainly occurring through quenching, affects its excited-state lifetime that is measured by fluorescence burst analysis. The binding of proteins to the gold NPs through antigen-antibody recognition further modifies the fluorophore excited-state lifetime. This change can therefore be used to measure the protein concentration.
In particular, we have tested the nanodevice by measuring the change of the fluorophore excited-state lifetime upon binding of a model protein, the bovine serum albumin (BSA); then we have applied the nanoassay in order to recognize the p53 protein, whose detection in the body is highly valuable as marker for early cancer diagnosis and prognosis, both in standard solutions and in total cell extracts.
The contents of this chapter are also reported in the publications:

- S.Freddi, L.D'Alfonso, M.Collini, M.Caccia, L.Sironi, G.Tallarida, S.Caprioli, G. Chirico, "Excited-state lifetime assay for protein detection on gold colloids-fluorophore complexes", J.Phys.Chem. C, 113:2722-2730, Jan 2009

- L.Sironi, S.Freddi, L.D'Alfonso, M.Collini, T.Gorletta, S.Soddu, G.Chirico "P53 detection by fluorescence lifetime on a hybrid fluorescein-isothiocyanate gold nanosensor", J.Biomedical nanotechnology, 5:683-691, 2009

- L.Sironi, S.Freddi, L.D'Alfonso, M.Collini, T.Gorletta, S.Soddu, G.Chirico

"In vitro and in-vivo detection of p53 by fluorescence lifetime on a hybrid FITC-gold nanosensor", Proceedings of SPIE, 7574:757403, 2010

3.1 Introduction

Biotechnology is pushing the minimum amount of detectable material toward lower and lower values [1]. The limiting values of detection depend on the experimental method, and they are of the order of 1-10 pM that, for a 60000 Da molecular weight protein, correspond to about 6-60 ng/L [2] [3]. One of the most promising properties that can be exploited in this field is related to the plasmonic resonances of noble-metal nanoparticles (NPs). These resonances, present also in bulk metals but shifted toward higher energy gaps with respect to the nanoparticle case, lie in the visible range of the spectrum and are due to excitation of surface waves of electrons on the nanoparticles or in a thin (<50 nm) layer of a noble metal. Plasmonic resonances have been detected in copper, gold, silver, and platinum in a spectral range that spans visible to infrared depending on the shape and kind of metal.

The plasmonic resonance is characterized by a very high extinction coefficient, on the order of $3{\cdot}10^{11} M^{-1} cm^{-1}$, and a resonant Rayleigh scattering efficiency similar to that of a large number of fluorophores (10^6). Concerning sensor applications, this effect is also very sensitive to the dielectric constant of the nanoparticle surface [4]. One of the best known detection methods based on these properties is the so-called surface plasmon resonance (SPR) assay [5]. This method is based on the change of the position of the plasmonic band induced by the binding of a biomolecule to a complementary molecule attached to the surface of a thin gold layer. The shift is measured by detecting the angular dependence of the reflectivity of the thin gold layer. The sensitivity in the concentration measurement is related to the amplitude of the shift of the reflectivity minimum. It has been also shown that gold NPs coverage of the SPR chip enhances the detection sensitivity [6].

Recently it has been suggested that biorecognition on the surface of gold and silver NPs can provide large sensitivity [7], also depending on the NPs form anisotropy [7]. However, the majority of sensors that use nanoparticle SPR have exploited the sensitivity of the surface plasmons themselves to the interparticle coupling. The dipole-dipole interaction mechanism [8], which can occur at distances up to 2.5 times the diameter of the particles [8] [9], broadens and red shifts the plasmon resonance components. This phenomenon has been primarily exploited for detecting binding [8]-[10].

It is noteworthy that the plasmon resonance can interact with the fluorescence emission of dyes and substantially modify their brightness and excited-state lifetime. Depending on the fluorophores-NP distance and the NPs anisotropy one can obtain fluorescence

enhancement or quenching [9],[11]. Emission enhancement effects can be due, for metal colloids, to local field enhancement and to coupling between the molecular dipole and the plasmonic excitations that can then radiate in the far field. Quenching, on the other hand, is related to the nonradiative coupling of the high spatial frequency components of the dye excitation to the plasmonic resonances that cannot radiate into the far field [12] and dominates the dipole-metal interactions for a reciprocal distance of 2-4 nm. Few examples of fluorescence based assays have been reported [13],[14], which exploit either the metal-induced fluorescence enhancement [15],[7] (MEF), tipically due to field enhancement on small aggregates of particles [7], or the fluorescence quenching [16]-[17]. In particular a relevant effort has been done for exploiting fluorescence quenching induced by nonradiative resonant energy transfer to quantum dots and gold nanoparticles for detection of proteins [18]-[19]. Plasmonic resonances depend on the difference between the metal dielectric permittivity and that of the surface layer [12],[20], similarly to the energy-transfer mechanism, that is maximum at the frequency at which the real part of the metal dielectric permittivity equals that of the layer on the interface [16]. Therefore, for both fluorescence enhancement and quenching, due to metal, we expect that any change in the dielectric constant of the NP surface, induced for example by a biorecognition process that occurs on the surface itself, can produce a change in the emission properties of the fluorophores [15], [9].

With this putative mechanism in mind, we studied the effect of the binding of proteins to the surface of gold NPs on the fluorescence emission properties (brightness and excited-state lifetime) of fluorescein bound to the NP itself.
This process can be in principle applied to any protein. Due to its relevance in cancer diagnosis, we have focused here on the p53 protein. The aim of the experiments reported hereafter is therefore to assess the possibility to detect traces of p53 protein by exploiting the fluorescence emission of the dye bound to the NPs.

The tumor suppressor p53 has been indicated as a tumor antigen, as an oncogene product or as a tumor marker [21]. It is one of the most commonly mutated proteins found in human cancers and its mutated forms may have specific functions [22],[23] alternative to original one. This property is the main reason why to p53 have been assigned widely different roles in the past years [24]. Wild type p53 (wt-p53) acts as a transcription factor that activates the expression of proteins that regulate the cell cycle, either halting the cycle until damage can be repaired, or in more extreme cases, causing the cell to die. Mutations in the TP53 gene are among the most common genetic alterations in human cancer. These alterations are usually associated with accumulation of mutant

p53 forms in cancer cells, due to the longer half-life of the p53 mutants with respect to the wtp53. Thus, the early detection of p53 in cell extracts and its quantification can be an extremely valuable tool in cancer prevention [25]. Since antibodies for an enormous variety of p53 mutated forms are available [23],[26], immuno-recognition is the candidate method to accomplish this goal. The limitations of the actual detection methods (changes in the optical response of thin gold layers [4],[9] or in the fluorescence signal on antibody functionalized surfaces by total internal reflection methods [27], [28], or colorimetric assays based on immuno-driven aggregation of gold colloids [29],[30]) are mainly related to the implementation of immuno-recognition on surface immobilized molecules, a process that is intrinsically slow, being diffusion limited. It would then be interesting to devise all-solution methods to enhance and fasten the recognition process which occurs on the nano-constructs and that could be used also for intracellular detection.
A hybrid nanodevice is proposed here, in which the protein detection occurs on the surface of an organic-metal hybrid complex: a gold nanocrystal functionalized by a fluoresceine derivative and the specific protein antibody. The detection of the protein is based on the measure of the dye excited state lifetime during the short fluorescence bursts that are due to the diffusion of the complexes through the excitation volume and it appears to be fairly insensitive to the dye photo-bleaching. This construct would be suitable for intracellular detection by choosing a capping layer that fosters the internalization of the NPs.
First the new metal-organic system has been tested for the recognition of a protein model system (bovine serum albumine, BSA). Then the feasibility of the detection of p53 in solutions and in total cell extracts (TCEs) has been addessed together with the selectivity of the proposed nano-constructs for p53 with respect to other globular proteins.
Before treating the experimental details and the results we briefly discuss the known properties of p53 protein.

3.2 p53 protein properties

Cancer is a serious disease caused by defective control of cell proliferation. The inactivation of tumor suppressor genes and deregulated expression of oncogenes is often the cause of cellular transformation. The multistep process of cancer development requires several genetic changes over a long period of time. Each cell contains the genetic information that has to be replicated and passed to the next progeny in the process of cell cycle [22]. This hereditary code is, however, altered constantly due to external pressure and the DNA in most of the cells experience numerous mutations every day. To support the precise genetic code from one cell generation to the next one, the cells have developed a number of regulatory pathways to monitor the entire process. Despite the high fidelity

of this machinery, some occasional mistakes can be passed by this system and be further transferred to the progeny. Errors in the control of the damage response may lead to the accumulation of genetic lesions and multiple phases of clonal selection eventually results in uncontrolled growth and predisposition to cancer [22][23].
One of the key proteins in the regulation of the genomic integrity is tumor suppressor protein p53. p53 can prevent accumulation of harmfull mutations, inhibiting tumor-promotion. Upon exposure to various kind of damage, p53 protein is activated and halts the cell cycle to give the repair machinery some time to solve the errors in the hereditary material. In case of excessive damage, however, the DNA may be in an unrepairable condition and the cell may have to choose a cell death pathway instead of the growth arrest to ensure maintenance of the genome. The ability of p53 to induced this programmed cell death, apoptosis, is probably its major function in preventing the neoplastic transformation [21]. The early events leading to cellular p53 response are not totally understood, even though they have been studied extensively over the past two decades. Inactivation of the p53 pathway is very common in cancers and reactivation a potential key factor in killing tumor cells. Although preventing the incidence of cancer by eliminating the risk factors would probably be the most effective way of reducing the number of cancer cases, new therapeutic possibilities are required [21][23]. Activation of the p53 pathway may have an important role in this process. Thus, knowing the factors that affect the function of p53 are critical to understand in detail.

Activities that have been attributed to p53 include: regulation of gene expression, DNA syntheis and repair [31][32], control of DNA replication[33], DNA damage response and cell cycle control. p53 acts also in cellular differentiation [34], senescence [35], inhibition of angiogenesis [36], and in programmed cell death [21][37]. p53 has gained special interest due to its activation in response to cellular stress to mediate a variety of anti-proliferative processes. p53 protein is a sensor of diverse forms of stress such as genotoxic stress (UV and IR, cytotoxic drugs, carcinogens), various non genotoxic stress (hypoxia, temperature changes, redox changes) and oncogenic stress [38][39]. Disruption of p53 function promotes checkpoint defects, cellular immortalization, genomic instability, and appropriate survival, allowing the continued proliferation and evolution of damaged cells [40].

3.2.1 P53 structure

Human p53 is a nuclear phosphoprotein of MW 53 kDa encoded by a 20 Kbp gene containing 11 exons interrupted by 10 introns [41], which is located in a single copy on the short arm of chromosome 17. This gene belongs to a highly conserved gene family

containing at least two other members, p63 and p73. Wild-type p53 protein contains 393 amino acids and is composed of several structural and functional domains: a N-terminus containing an amino-terminal domain (residues 1-42) and a proline rich region with multiple copies of the PXXP sequence (residues 61-94, where X is any amino acid), a central core domain (residues 102-292), and a C-terminal region (residues 301-393) containing an oligomerization domain (residues 324-355), a strongly basic carboxylterminal regulatory domain (residues 363-393), a nuclear localization signal sequence and 3 nuclear export signal sequence.

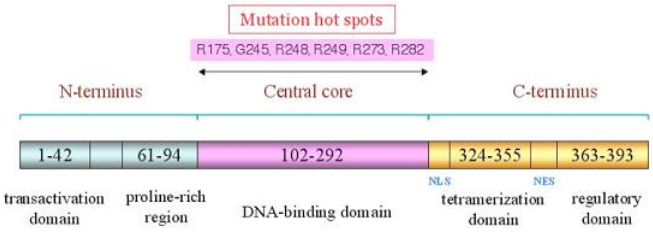

Figure 3.1: *Schematic representation of the p53 structure. p53 contains 393 amino acids, consisting of three functional domains, i.e. an N-terminal activation domain, DNA binding domain and C-terminal tetramerization domain. The N-terminal domain includes transactivation subdomain and a PXXP region that is a proline-rich fragment. The central DNA binding domain is required for sequence-specific DNA binding and amino acid residues within this domain are frequently mutated in human cancer cells and tumor tissues. The C-terminal region is considered to perform a regulatory function. Residues on this basic C-terminal domain undergo posttranslational modifications including phosphorylation and acetylation. Numbers indicate residue number. NLS, nuclear localization signal sequence; NES, nuclear export signal sequence.*

The amino terminal region

The first 42 amino acids of p53 make up an acidic region called transcription-activation domain, because this region regulates gene expression and interacts with various transcription factor including acetyltransferases and Mdm2 (murine double minute 2, which in humans is identified as Hdm2)[42]. Later, second transcription activation domain has been described (between amino acids 43 and 73)[43]. p53 has a proline rich region (amino acids 63-97) necessary for transcriptional repression by p53 and is required for (transcription-independent) growth suppression by p53-mediated apoptosis[44]. The activity of p53 is modulated by the interaction of the N-terminal part with other proteins and several posttranslational modifications take place in this part of p53.

The core domain

The sequence specific DNA binding domain is an antiparallel β sheet that serves as scaffold for 2 α helix loops that physically bind DNA. The DNA-binding domain or core domain spans form amino acid 102 to 292 and forms a separate independently folding structure that binds to the DNA sequence specifically [45][32]. In human tumors, the p53 protein is often mutated and mutant proteins have principally lost the growth suppression functions. 95% of tumor-related mutations map to the residues of the DNA binding region and among them certain "hot spots" of mutations have been described. These mutations occur as residues essential for DNA-binding and therefore inactivate the transcriptional activation function of p53, giving an example how p53 is inactivated in tumors [21]. The core domain contains also region necessary for the binding of p53 with the negative regulators of apoptosis. Altogether, these findings confirm how important this region is for the function of p53 as a tumor suppressor.

The C-terminal region

The central core domain is connected to the C-terminal region with the flexible linker region (amino acids 300-318) [46].
p53 requires nuclear localization for the function [47], which is ensured by three nuclear localization sequences in the C-terminal region (amino acids 316-325, 369-375, 379-384) [48]. The p53 export from the nucleus has been shown to be mediated by two nuclear export signal sequences located in the activation domain (amino acids 11-27) and in the tetramerization domain (amino acis 339-352) of p53 [49]. Full length p53 protein forms stable tetramers and the tetramerization domain including amino acids 324-355 is responsible for the oligomerization of p53 [46]. Although monomeric p53 is able to bind DNA, activate transcription, and suppress growth [50], p53 is believed to function much more efficiently as a tetramer probably due to the greater DNA binding affinity [51].

Normal p53 funcion also relies on proper conformation and oligomerization of the protein, a process that is regulated by the tetramerization domain. Two monomers associate to form an antiparallel double stranded sheet, known as a dimer. The tetrameric form of p53, a dimer of dimers, has enhanced ability to interact with either DNA or various proteins. Although relatively uncommon, mutations in the tetramerization domain (4%) prevent tetramerization, DNA binding and tumor cell growth inhibition. Finally, the C-terminus contains 9 basic amino acids that specifically bind DNA and RNA, and appear important in p53 regulation of DNA repair processes.

Studies of the regulation of p53 tertiary structure have provided ideas for the conformation model for the functioning of p53. According to this model, mutations that deregulate the normal control of p53 conformation may lead to cancer [52]. It has been

shown that one of the two alleles of the p53 gene is mutated in the cell, the mutant p53 protein can inactivate the wild type p53 in a dominant-negative manner. This dominant-negative activity has been explained with the ability of the mutant p53 protein having different conformation to form mixed tetramers with wild type p53 driving the latter into the mutant conformation [52]. These kinds of hetero-oligomers lack the growth suppression function [53]. Due to such dominant negative effect over wild type protein, the wild type p53 cannot avoid malignant growth if it co-expresses with the mutant p53 protein.
Next to the oligomerization domain is the basic region (amino acids 363-393), named regulatory domain, which is required for regulation of the p53 activity. p53 is unusual among transcription factors, because it has also non-specific DNA-binding ability in addition to the sequence-specific DNA binding [54].

A model for the activation of p53 has been proposed according to which the C-terminus of p53 interacts with the core domain. This interaction locks the core domain into a conformation keeping p53 in a latent, low-affinity DNA-binding form that is inactive for DNA binding [55]. The core domain is able to adopt an active conformation (efficient DNA-binding) after the modification or deletion of C-terminus, or protein-protein interaction. The binding of ssDNA ends or short ssDNA fragments to C-terminal domain may also stabilize p53 in a conformation, active for binding to target DNA sequences [56]. Furthermore, the proline-rich region at the N-terminus of p53 has been suggested to cooperate with C-terminus for the maintenance of the latent, low affinity DNA-binding conformation of p53. Thus, p53 requires a structural change for the activation of sequence specific DNA binding and this occurs through boh N-terminal and the basic C-terminal domain.

3.2.2 Control of the p53 protein half-life

The p53 protein level in the cell is determined by the rates of its synthesis and degradation. p53 has a short half-life of only about 20 minutes in normal cells due to rapid degradation [57]. When active as a transcription factor, p53 encourages the synthesis of Mdm2- the agent of its own destruction. This creates a negative-feedback loop that usually functions to ensure that p53 molecules are degraded soon after their synthesis [58], resulting in the very low steady-state levels of p53 protein observed in normal, unperturbed cells. The operations of this p53-Mdm2 feedback loop explain a bizzarre aspect of p53 behavior [58]. In human cancer cells that carry mutant, defective p53 alleles, the p53 protein is almost invariably present in high concentrations, in contrast to its virtual absence from normal cells. At first glance, this might appear paradoxical, since high levels of a growth-suppressing protein like p53 would seem to be incompatible

with malignant cell proliferation. The paradox is resolved by the fact, mentioned above, that the great majority of the mutations affecting the p53 gene cause the p53 protein to lose its transcription-activating powers. As a direct consequence, p53 is unable to induce Mdm2 transcription and thus Mdm2 protein synthesis. In the absence of Mdm2, p53 escapes degradation and accumulates to very high levels. This means that many types of human cancer cells accumlate high concentrations of essentially inert p53 molecules.

3.2.3 p53 induction

Three well-studied monitoring systems have been found to send alarm signals to p53 in the event that they detect damage or signaling imbalances [59][60]. The first of these responds to double-strand breaks in chromosomal DNA, notably those that are created by ionizing radiation such as x-rays [60][61]. Indeed, a single dsDNA break occurring anywhere in the genome seems sufficient to induce a measurable increase in p53 levels. A second signaling pathway is activated by a wide variety of DNA damaging agents, including certain chemotherapeutic drugs and UV radiation [61]; certain inhibitors of protein kinases also stimulate this pathway [21][24]. A third pathway leading to p53 activation is triggered by aberrant growth signals [60]. The mechanisms by which other physiologic stresses or imbalances, such as hypoxia, trigger increases of p53 levels remain poorly understood. These converging signaling pathways reveal a profound vulnerability of the mammalian cells. The funnelling of these diverse signals to a single protein would seem to represent an elegant and economic design of the cellular signaling circuitry. But it also put cells at a major disadvantage, since loss of this single protein from a cell's regulatory circuitry results in a catastrophic loss of the cell's ability to monitor its own well-being and respond with appropriate countermeasures in the event that certain operating systems malfunction. In one stroke (actually, the two strokes that cause successive inactivation of the two p53 gene copies), the cell becomes blind to many of its own defects. It thereby gains the ability to continue active proliferation under circumstances that would normally cause it to call a halt to proliferation or to enter into apoptotic death [60][21]. In addition, loss of the DNA repair and genome-stabilizing functions promoted by p53 will make descendants of a $p53^{-/-}$ cell more likely to acquire further mutations and advance more rapidly down the road of malignancy. All three pathways inhibit the degradation of p53 protein, thus stabilizing p53 at high concentration. The increased concentration of p53 allows the protein to carry out its major function: to bind to particular DNA sequences and activate the expression (transcription) of adjacent genes. These genes, directly or indirectly, lead ultimately to cell death or the inhibition of cell division [60]. In the event that DNA is successfully repaired, the signals that have protected p53 from destruction will disappear. The consequence is that the levels

of p53 collapse. This allows cell cycle progression to resume and the DNA replication to proceed. By preventing cell cycle advance and DNA replication while chromosomal DNA is damaged and by inducing expression of DNA repair enzymes, p53 can reduce the rate at which mutations accumulate in cellular genomes. Conversely, cells that have lost p53 function may proceed to replicate damaged, still-unrepaired DNA, and this can cause them, in turn, to exhibit relatively mutable genomes, that is, genomes that accumulate mutations at an abnormally high rate per cell generation [60][62].

3.2.4 P53 often ushers in the apoptotic death program

p53 can opt, under certain conditions, to provoke a response that is far more drastic than the reversible halting of cell cycle advance. In response to massive, essentially irreparable genomic damage, anoxia (extreme oxygen deprivation), or severe signaling imbalances, p53 will trigger apoptosis [21][62]. The cellular changes that constitute the apoptotic program proceed according to a precisely coordinated schedule. Within minutes, patches of the plasma membrane herniate to form structures known as blebs; indeed, in time-lapse movies, the cell surface appears to be boiling. The nucleus collapses into a dense structure- the state termed pyknosis- and fragments as the chromosomal DNA is cleaved into small segments. Ultimately, usually within an hour, the apoptotic cell breaks up into small fragments, sometimes called apoptotic bodies, which are rapidly injested by neighboring cells in the tissue or by itinerant macrophages. In the specific context of cancer pathogenesis, the organism uses p53-triggered apoptosis as a means of weeding out cells that have the potential to become neoplastic, including some cells that have sustained certain types of growth-deregulating mutations and others that have suffered widespread damage of their genome [62][59] .
To summarize, the various observations cited here indicate that the biological actions of p53 fall into 2 major categories. In certain circumstances, p53 acts in a cytostatic fashion to halt cell cycle advance. In other situations, p53 activates a cell's previously latent apoptotic machinery, thereby ensuring cell death. The choice made between these alternative modes of action seems to depend on the type of physiologic stress or genetic damage, the severity of the stress or damage, the cell type, and the presence of other pro and anti-apoptotic signals operating in a cell. At the biochemical level, it remains unclear how p53 decides between imposing cell cycle arrest and triggering apoptosis [59].

3.3 Experimental details

3.3.1 Sample preparation

Chemicals, Proteins, and Nanoparticles

Gold colloids 10 and 5 nm in size, functionalized by streptavidin, were purchased from Ted Pella Inc. (Redding,CA, code 15840 and 15841) and purified by two steps of 13000 rpm centrifugation. As reported on the product data sheets, the 10 nm and 5 nm gold NPs have an average number of 20 and 5 streptavidins and a concentration of 28 and 280 nM, respectively (stock solutions). The p53 protein, its monoclonal antibody and the monoclonal antibody of BSA protein were obtained from Abcam (Cambridge, UK, P53, ab43615-50, mAb to p53 (biotinylated) ab27696-100, RbpAB to BSA (BIOTIN) ab7636-1) and the biotinylated fluorescein isothiocyanate (FITC) dye from Pierce (Rockford, IL, code 22030). Bovine serum albumin (BSA), beta-lactoglobulin (BLG) and lysozyme proteins were purchased from Sigma-Aldrich (codes A-0281, L-8005, L-6876) and used without further purification. After the NP-fluorophores binding reaction, all the solutions of gold colloids were dialized (15000 D molecular weight) against phosphate buffer in order to get rid of the unlabeled fraction of the fluorescent molecules. The solutions were then centrifuged twice at 13000 rpm before use. For the fluorescence experiments, the stock solutions were diluted 1:1000 in phosphate buffer at pH 7.5.

Nanoparticle-Dye Complexes

In order to understand the changes in the fluorescence emission of the dye when coupled to the gold NPs we devised a series of constructs all based on the strong streptavidin-biotin interaction. The basic sensor construct (NP-FITC-Ab) is obtained by binding biotin-FITC and the protein biotinilated antibody (Ab) to the gold NP functionalized with streptavidin (Sav), as shown in Figure 3.2.

As reported on the product data sheets, the 10 and 5 nm gold NPs have an average number of 20 and 5 Sav, respectively. The binding of the two components, FITC and Ab, to the Sav-NP was performed in a single step in order to avoid saturation of the binding sites on the NP with either the Ab or the FITC. All binding reactions were performed overnight in the dark under mild stirring conditions in phosphate buffer. The ratio, $R_{FITC} = [Ab] : [FITC]$, of the sites on the gold NPs occupied by the antibodies to those occupied by FITC was tuned by changing the stoichiometric ratio of the two components during labeling. We performed preliminary tests on various R_{FITC} ratios and found that the best sensitivity in terms of the relative change in the FITC excited state lifetime and limited reduction of the FITC fluorescence signal when bound to the gold NP (see par. 3.9) corresponds to a ratio [Ab]:[FITC] = 3:1 (construct A in Figure

3.2). The ratio R = [Ab]:[protein] was varied in the experiments as detailed in par. 3.9.

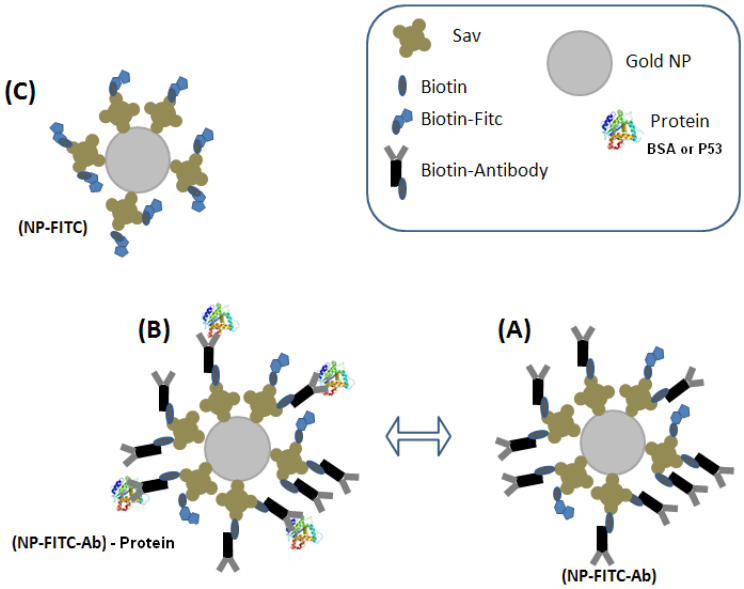

Figure 3.2: *(A-C) Basic constructs used to investigate the possibility of fluorescence detection of proteins at picomolar concentrations. The symbols refer to Streptavidin (Sav), gold nanoparticles (NP), fluorescein isothiocyanate (FITC). Relative sizes are not drawn to scale. The constructs are (A) the gold NP conjugated to the biotinilated FITC through the Sav-biotin binding (NP-FITC); (B) gold NP coupled to the biotin-FITC and the protein antibody at a ratio [Ab]:[FITC]=3:1 (NP-FITC-Ab); (C) construct B after reaction with the protein BSA or P53 (NP-FITC-Ab-protein).*

Cell Lines, Culture Conditions and Treatments

Human HCT116 colon cancer cells (wild type p53, wtp53) and H1299 lung cancer cells (homozygous partial deletion of the TP53 gene [1] [63]) were maintained as monolayers in DMEM supplemented with 10% heat-inactivated fetal calf serum, 2 mM L-Glutamine, Penicillin-Streptomycin (EuroClone) at 37°C in a 5% CO_2 atmosphere. The HCT116 line expresses the wild-type p53 (wtp53) protein. The H1299 cells have a homozygous partial deletion of the TP53 gene and as a result do not express the tumor suppressor p53 protein, which in part accounts for their proliferative propensity [63]. For DNA damage induction, sub-confluent cells were UV irradiated with 20 J/cm^2 for 30 seconds and harvested 18 h later. Cell pellets were stored at -80°C until lysed for further analysis. TCEs were obtained by incubating the cells for 30 min with lysis buffer [50 mM Tris HCl (pH 7.5), 5 mM EDTA, 250 mM NaCl, 1% NP-40, 0.5% sodium deoxycholate,

[1] kind gift of Dr. Silvia Soddu, Experimental Oncology Department, Molecular Oncogenesis Laboratory, Regina Elena Cancer Institute, Rome

0.1% SDS] supplemented with a protease inhibitor mix.

3.3.2 Experimental methods

Spectral characterization

Spectrophotometric measurements were performed on a Jasco V570 spectrophotometer (Jasco, Japan). The fluorescence emission spectra were acquired on a Varian Eclipse spectrofluorimeter (Varian, U.K.).

Dynamic light scattering characterization

For Dynamic Light Scattering (DLS) a home-made setup [18] for variable angle measurement of the scattered light autocorrelation function has been used with a He-Ne 30 mW polarized laser source. The correlator board was an ISS (Urbana Champaign, IL) single photon counting acquisition board and the data were analyzed as described below.
For the constructs based on model protein BSA, the normalized intensity autocorrelation functions (ACFs) were fit to a multiexponential decay

$$G(\tau) = \frac{\langle I(t+\tau)I(t)\rangle_t}{\langle I\rangle^2} = 1 + f_{coh}(\sum_k A_k exp[-D_k q^2 t])^2 \tag{3.1}$$

where D_k is the translational diffusion coefficient of the k-th species of the NPs or NP aggregates, q is the wave vector, q $=(4\pi n)/(\lambda)sin(\theta/2)$, n is the solution (water) index of refraction, and λ is the laser light wavelength (633 nm). The parameter f_{coh} is an indication of the ratio of the detector to the coherence area and was left as a free fitting parameter, typically in the range 0.15-0.35. The pre-exponential factors, A_k, which are proportional to the product of the square of the molecular mass M_k times the number concentration n_k, can be used as an estimate of the relative concentration of the particles according to

$$A_k \approx n_k M_k^2 \approx n_k V_k^2 \tag{3.2}$$

where V_k is the hydrated volume of the k-th species. The cumulant analysis of the data was performed by fitting the ACFs (maximum lag time = 600-800 μs) to a third-order cumulant function

$$G(\tau) = \frac{\langle I(t+\tau)I(t)\rangle_t}{\langle I\rangle^2} = Aexp[-2(tD_{cum}q^2 - \frac{t^2}{2}(D_{cum}q^2)^2\sigma + \frac{t^3}{6}(D_{cum}q^2)^3\mu_3)] \tag{3.3}$$

The polydispersity of the samples, σ, depends on the NP construct as discussed later.

The analysis of p53 protein based constructs was performed both with cumulant analysis and, in a more exhaustive way, with the Maximum Entropy method, through the procedure described in the following. The second order autocorrelation functions (ACFs) of the scattering light were first converted into the first order ACFs, G(t), and the first order ACFs were analyzed by means of the Maximum Entropy method [64] obtaining the distribution of relaxation times according to the relation:

$$G(t) = A \int_{-\infty}^{\infty} dlog(\tau) P_{\tau}(log(\tau)) exp[-t/\tau] \tag{3.4}$$

The relaxation time τ is inversely proportional to the particle diffusion coefficient, D, and the exchanged wave vector, q, by the relation $\tau = 1/(Dq^2)$.

D is related to the particle average hydrodynamic radius, R_h, as $D = K_B T/(6\pi\eta R_h)$. We assume here an average globular shape of the bare and the protein coated nanoparticles. Therefore the linear relation between the relaxation time and the hydrodynamic radius, $\tau = R_h(6\pi\eta)/(K_B T q^2) = R_h/\rho$, can be used to compute the number distribution of particles with radius R_h by fitting the P_τ distributions to a sum of log-normal functions of the type:

$$P_R(log(R_h)) = \frac{1}{\tau} P_{\tau}(log(\tau)) \tag{3.5}$$

$$P_R(log(R_h))|_{R_h=\rho\tau} = A \sum_j \alpha_j \langle R \rangle_j^6 exp\left[-\frac{(log(R_h) - log(\langle R \rangle_j))^2}{2\sigma_j^2} \right] \tag{3.6}$$

where $\langle R \rangle_j$ and σ_j are the average values of the hydrodynamic radius and the width of the distribution component and α_j is the number fraction of the j-th component ($\sum_j \alpha_j$=1) in the distribution. The number distribution of size shown in section 3.7 is given by the computation of the function:

$$P_{n,R}(log(R_h))|_{R_h=\rho\tau} = A \sum_j \alpha_j exp[-\frac{(log(R_h) - log(\langle R \rangle_j))^2}{2\sigma_j^2} \tag{3.7}$$

with the parameters obtained by the best fit of the experimental distribution of the relaxation times.

3.4 Fluorescence Spectroscopy

The fluorescence spectroscopy and lifetime measurements were performed on a custom-made micro-spectrometer based on a Nikon TE300 microscope equipped with a mode-

locked Ti:Sapphire laser (Tsunami, Spectra Physics, Mountain View, CA) with pulses of 230 fs full width at half-maximum on the sample and 80 MHz repetition frequency. In all experiments on FITC the fluorescence emission (band pass filter HQ515/30) was primed by Two Photon Excitation (TPE) at λ_{exc}=800 nm, in order to achieve a small excitation volume that was typically 0.8 μm^3, as estimated from Fluorescence Correlation Spectroscopy measurements on reference dyes [65]. The average laser power was 40 mW for 10 nm and 80 mW (before the entrance of the microscope) for 5 nm NP samples. The fluorescence emission was acquired by a Single Photon Avalanche Diode (SPCM-AQR15 Perkin-Elmer, USA) whose signal was fed to a digital TimeHarp 200 (Picoquant, Berlin, D) board. The analysis was performed either with a dedicated software written in CVI (National Instruments, USA) or with the SymphoTime program by Picoquant in order to compute the rate trace at the desired sampling time and the lifetime histograms. For the lifetime histogram analysis the setup impulse response function (IRF), close to 350 ps, was measured by collecting the signal scattered from the pure solvent. The IRF and the decays were then deconvoluted by means of the SymphoTime program. The normalized ACFs were acquired by a ALV5000E (ALV, Langen, D) board and analyzed by means of the non-least square routine of the Origin 7.0 (OriginLab Inc., Northampton, MA) software.
In the fluorescence traces, distinct photon bursts approximately 10-200 ms wide were detected and ascribed to the passage of the NP constructs through the excitation beam waist (fig. 3.3). The diffusion coefficient of the constructs can be evaluated as D$\cong$ $\omega_0^2/8\tau_D$, where the diffusing time, τ_D, is taken here as the FWHM of the burst. The lifetime histograms were computed on the selected bursts and, for comparison, on the background, as detailed in the par. 3.9.

The lifetime histograms have been fitted to a multiexponential decay according to

$$I(t) = \sum_i \alpha_i exp(-t/\tau_i) \tag{3.8}$$

where α_i are the pre-exponential factors of the i-th component with lifetime τ_i. The prexponetial factors are related to the fractional intensities f_i by

$$f_i = \alpha_i \tau_i / \sum_i \alpha_i \tau_i \tag{3.9}$$

For a double-exponential decay the average lifetime can be defined as

$$\langle \tau \rangle = f_1 \tau_1 + (1 - f_1)\tau_2 \tag{3.10}$$

since $f_2 = 1 - f_1$.

The fitting of the FCS autocorrelation function, G(t), was performed according to a 3D diffusion model with a Gaussian-Lorentzian beam profile described by the function

$$G(t) = \frac{0.076}{\langle N \rangle} \left(1 + \frac{t}{\tau_D}\right)^{-1} \left(1 + \left(\frac{\lambda}{\sqrt{2}\pi\omega_0}\right)^2 \frac{t}{\tau_D}\right)^{-0.5} \tag{3.11}$$

where $\langle N \rangle$ is the average number of molecules in the excitation volume, τ_D is the diffusion time, and ω_0 is the beam waist, typically 0.67 μm. The typical excitation volume, at an excitation wavelength λ= 800 nm, was $V_{exc} = \pi\omega_0^4/\lambda = 0.8 \pm 0.1\ \mu m^3$. The translational diffusion coefficient, D=$(\omega_0^2)/(8\tau_D)$, is related, for a spherically symmetric diffusing object, to the hydrodynamic radius by

$$\langle R_h \rangle = \frac{k_B T}{6\pi\eta D} \tag{3.12}$$

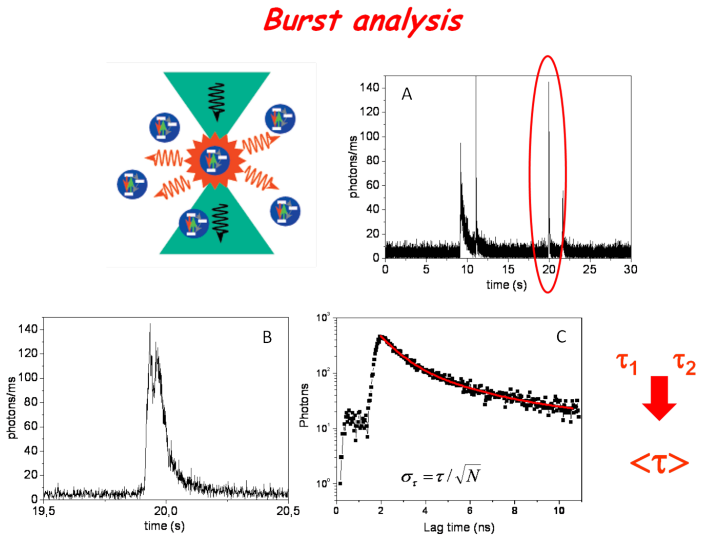

Figure 3.3: *The passage of the constructs, which recognized the protein, through the excitation beam waist produces fluorescence burst ≈ 10-200 ms wide (panel A). Panel B shows a zoom of the burst in panel A. The lifetime histogram in panel C is computed by SymphoTime sofware and analized as described in the text.*

3.5 Photon Counting Statistics

In order to estimate the particle brightness we have computed the first two moments of the photon counting distribution according to the Photon Counting Histogram (PCH) method [66] and its subsequent modification to Photon Counting Moment Analysis (PCMA) [67], [68]. The photon counting was computed over 50 μs sampling time, much

shorter than the diffusion time both of the free FITC dye and the gold NPs, and the average number of particles per observation volume, N, and the average brightness, ϵ, were computed according to the relations:

$$\langle k \rangle = \langle N \rangle \, \epsilon \tag{3.13}$$

$$\frac{\langle k^2 \rangle - \langle k \rangle}{\langle k \rangle} - 1 = 0.076\epsilon \tag{3.14}$$

Dead-time and afterpulsing corrections were applied as is [68].

3.6 Measurements

The aim is to exploit changes of the dye excited-state lifetime and brightness induced by its interaction with the gold surface plasmons for detection of tiny amounts of protein in solution under physiological conditions. The system we investigated is based on 10 and 5 nm diameter gold NPs coupled (via a biotin-streptavidin linker) to the FITC dye and to a specific protein antibody (Figure 3.2, panels A-C). The interaction of the fluorophore with the gold surface plasmon resonances, mainly occuring through quenching, affects the excited state lifetime that is measured by fluorescence burst analysis in standard solutions. The binding of protein to the gold NPs through antigen-antibody recognition further modifies the dye excited-state lifetime. This change can therefore be used to measure the protein concentration.

At first the system composed of a gold NP 5 or 10 nm in size, functionalized with a fluoresceine derivative (FITC), the specific protein antibody and the protein (BSA or P53) has been characterized through Dynamic Light Scattering (constructs NP-FITC-Ab_{BSA}-BSA and NP-FITC-Ab_{P53}-P53). In particular the construct NP-FITC-Ab_{BSA}-BSA was analized through cumulant analysis, whereas the assay NP-FITC-Ab_{P53}-P53 was also characterized in a more exhaustive way through Maximum Entropy analysis.
Then the nanodevice has been analized through Fluorescence Spectroscopy and used as a test for the recognition of the model protein BSA. At last, the feasibility of the detection of the p53 protein in solution and in total cell extracts (TCEs) has been addressed together with the selectivity of the construct with respect other globular proteins.

3.6.1 Dynamic Light Scattering: cumulant analysis

In order to know the degree of aggregation of the constructs in detail, dynamic light scattering studies have been performed.
The effective radii of the constructs can be estimated by taking into account the size of

the streptavidin (4.5 x 4.5 x 5.0 nm) [69], of the BSA specific antibody (hydrodynamic radius of 5.5 nm) [19], and of the BSA itself (hydrodynamic radius of 3.4 nm) [20]. Since the Sav completely covers the gold nanoparticle surface we can estimate the NP-Sav radius as $R_{mon} \cong (5 + 4.5 + 4.5)/2 \cong 7$ and $(10 + 4.5 + 4.5)/2 \cong 9.5$ nm for the 5 and 10 nm diameter NPs, respectively. Upon antibody addition the maximum radius that can be obtained at the highest degree of saturation is $R_{mon} = 12.5$ and 15 nm for the 5 and 10 nm diameter NPs, respectively. When BSA is also added these values become $R_{mon} = 15.9$ and 18.4 nm, at most, for the 5 and 10 nm diameter NPs, respectively. We notice that the size of the monomer NP with its Sav and antibody layer cannot be easily obtained from DLS analysis due to the polydispersity of the solutions.
The high scattering cross-section of the gold NPs [4] allowed us to perform experiments on the same diluted solutions ($n_{10nm} \cong 100$ pM; $n_{5nm} \cong 50$ pM) used in the fluorescence experiments. Typical ACFs of the scattered light collected from 5 and 10 nm NP-FITC-Ab-BSA at R = 1:1 are reported in Figure 3.4. The cumulant analysis (shown in the inset) of the ACFs according to eq 3.3 yields a polydispersity $\sigma \cong 0.6$ for the 5 nm NPs and $\sigma \cong 1.6$ for the 10 nm NPs. For the smaller constructs a continuous mass distribution is present, whereas for the 10 nm NPs the contribution of larger aggregates gives rise to a separate component in the ACF decay. The average hydrodynamic radius obtained by the cumulant analysis is $R_{cum} = D_{cum}/(k_B T) = 55 \pm 5$ and 100 ± 10 nm for the 5 and 10 nm gold NPs solutions, respectively. The aggregation number N_{agg} scales according to the metal colloids fractal dimension [[70],[30]] d_f=1.9 and is related to the aggregate and monomer size by:

$$N_{agg} = (\frac{R_{cum}}{R_{mon}})^{d_f} \tag{3.15}$$

Therefore from the R_h data reported in table 3.1 we can estimate $N_{agg}^{DLS} \cong 10 \pm 3$ and 25± 5 for the 5 and 10 size gold NPs, respectively (Table 3.1).

NPs	$\mathbf{A}_1$	D_1 (μm^2/s)	$R_{h1}(nm)$	$\mathbf{A}_2$	D_2 (μm^2/s)	$R_{h2}(\mu m)$	$\mathbf{R}_{cum}$ **(nm)**
5 nm	0.22±0.02	52±5	82±8	0.76±0.02	9.3±0.3	0.45±0.02	55±5
10 nm	0.30±0.05	19.5±0.7	215±15	0.59±0.07	1.4±0.1	3±0.2	100±10

Table 3.1: *Analysis of the DLS ACFs. Fitting parameters of the DLS ACFs. The scattering angle was 90°, and the laser wavelength was λ=633 nm. The binding ratio was R=[Ab]:[BSA]=1:1. The ACFs were analyzed by fitting the data to eq 3.1 with two average components. The radii R_{h1} and R_{h2} are obtained through eq 3.12. The aggregation number is evaluated by comparing the average hydrodynamic radius to the estimate of the monomeric gold NP (eq 3.18). The first cumulant analysis was performed according to eq 3.3, and it provides the value of the first cumulant particle radius, R_{cum}.*

A fit of the whole ACFs decay can be performed by a double exponential analysis

according to eq 3.1, and it provides the average diffusion coefficients for each component together with their amplitudes, summarized in Table 3.1. The faster component corresponds to an average hydrodynamic radius of $\langle R_{h1} \rangle \cong 82$ nm for the 5 nm NPs and $\langle R_{h1} \rangle \cong 215$ nm for the 10 nm NPs, while the slower component corresponds to a size $\langle R_{h2} \rangle \cong 0.45$ μm for the 5 nm NPs and $\langle R_{h2} \rangle \cong 3$ μm for the 10 nm NPs. As derived from eq 3.2 the molar concentration of each species is proportional to $n_i = (A_i)/(\langle R_{hi} \rangle^{2d_f}$. Therefore, the concentration ratio of the two populations can be estimated as $n_1/n_2 \cong 200$ for the 5 nm gold NPs and $n_1/n_2 \cong 10^4$ for the 10 nm gold NPs. This finding indicates the presence of less than 1% in number of very large aggregates. Since $n_1 \cong 100$ pM, the corresponding number concentration of these large aggregates should be $n_2 \cong 0.5$-0.01 pM. It must be noted that the size derived from DLS is related to the mass average through the relation

$$\frac{1}{\langle R \rangle} = \frac{\sum_i (\frac{1}{R_i} n_i M_i^2)}{\sum_i (n_i M_i^2} \tag{3.16}$$

Therefore, more massive aggregates give a larger contribution to the ACFs, thus explaining the more marked presence of the larger aggregate component for 10 nm NPs ACFs in spite of their lower number concentration compared to the 5 nm constructs.

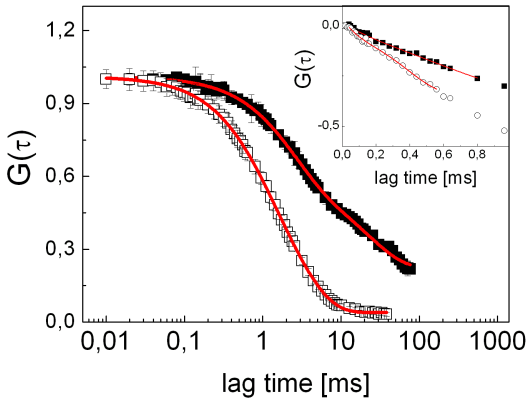

Figure 3.4: *ACFs of the light scattered by the 5 (open squares) and 10 nm (full squares) NP-FITC-Ab-BSA constructs at [Ab]:[BSA]= 1:1. Lines represent best fit to a two-component decay as discussed in the text. The inset shows the cumulant analysis expressed by a log-lin plot of the field correlation function* $\approx \sqrt{G(\tau)}$ *together with a third-order polynomial fit (solid lines). The symbols are as in the main panel. The best fit polynomials are as follows: -0.25-135t+11243t*^{2}*-570842t*^{3} *(5 nm NPs) and -0.61-47.4t+3801t*^{2}*-129334t*^{3} *(10 nm NPs). DLS parameters are reported in Table 3.1.*

3.7 Dynamic Light Scattering of p53 construct: MEM analysis

The estimate of the average size of the antibody and the streptavidin is not straightforward. From the pdb data bank (www.pdb.org) we evaluate radii of about 4 and 8 nm for the Streptavidin (entry 2IZJ, http://www.rcsb.org/) and the antibody (entry 1 IGT, http://www.rcsb.org/), respectively. We then estimate an average radius $R_{mon}^{(5)} \cong 2.5 + 8 + 16 \cong 26.5$ nm for a 5 nm diameter gold colloid and $R_{mon}^{(10)} \cong 29$ nm for the 10 nm size gold colloid.
The MEM analysis of the first order scattered light ACFs (Figs. 3.5) indicates the presence of at least two populations with widely different number concentrations and sizes (Table 3.2). For the NP-FITC-Ab_{p53} construct in the absence of p53, the major population in terms of number concentration has an average radius $\cong 45\pm$ 20 nm, independently of the size of the NP used for the construct (Table 3.2).

Construct	**10 nm** R=∞	**10 nm** R=5:1	**5 nm** R=∞	**5 nm** R=5:1
$\langle R_{h,1} \rangle$ [nm]	130± 30	166±70	45±24	210±60
$\langle R_{h,2} \rangle$ [nm]	1100± 400	1400±600	700±400	1200±450
$\alpha_2(\%)$	≅0.003	0.01±0.005	≅0.001	0.5±0.3

Table 3.2: *MEM analysis of the photon correlation spectroscopy autocorrelation functions. The hydrodynamic radii, $\langle R_{h1} \rangle$ and $\langle R_{h2} \rangle$, and the number fractions, α_2, were obtained by fitting the MEM distributions of the relaxation times to Eq.3.6 as described in the text. R = [Abp53]:[p53]=∞ indicates that no p53 was added to the sample.*

This is consistent with the observation that most of the size of the NP-FITC-Ab_{p53} construct is due to the streptavidins and to the antibodies. The MEM analysis indicates also the presence of tiny amounts ($< 0.1\%$ in number concentration) of larger aggregates in the sample, that correspond to sizes $\geq$ 500-600 nm. If we assume that the NP-FITC-Ab_{p53} aggregates have a fractal shape and that the aggregation number scales as $N_{agg} = (R_{ave}/R_{mon})^{d_f}$, where $d_f \cong 1.9$ is the fractal dimension of the aggregates, we can estimate, from the average size $\langle R_h \rangle \cong 45$ nm, aggregation numbers of the order of 2.8 ± 0.8 and 2.3 ± 0.8 for the 5 and the 10 nm NP constructs in the presence of p53. When the NP-FITC-Ab_{p53} constructs interact with the p53, we measure, through the MEM analysis of DLS autocorrelation functions, that the major component of the size distribution has an average hydrodynamic radius, $\langle R_{5nm} \rangle = 200\pm$ 60 nm and $\langle R_{10nm} \rangle = 170\pm$ 70 nm, for a 1:1 stochiometric ratio between the protein and the NP-FITC-Ab_{p53} construct. In the computation of the aggregation number we can also take into account

the small increase of the monomer size due to the p53 binding, ≅ 2 nm (entry 2J0Z, http://www.rcsb.org/), and evaluate N_{agg}= 5 ± 0.8 and 7 ± 0.6 for the 5 and 10 nm NP constructs. It should however be noted that for such low aggregation numbers the fractal aggregation assumption may fail.

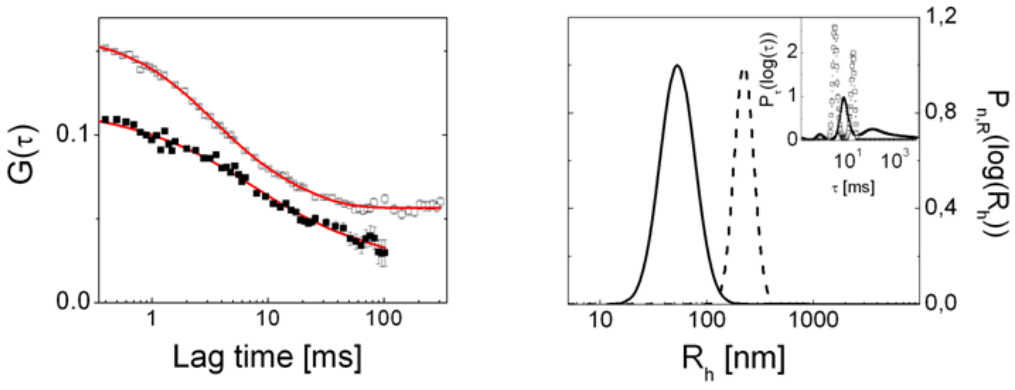

Figure 3.5: *Left: the ACFs of the light scattered by solutions of 5 nm NP-FITC-Ab_{p53} constructs without (filled symbols, R=∞) and with (open symbols, R=5:1) p53, together with their MEM best fit functions (red solid lines). Right: the number distributions of the hydrodynamic radii, Rh, computed from the best fit parameters of the relaxation time distribution functions (MEM analysis). The solid and dashed lines refer to the R=∞ and R = 5:1 cases (NP size 5 nm), respectively. The relaxation time distribution functions are reported in the inset with the same symbols as in panel on the left.*

3.7.1 Absorption spectra

The absorption spectrum of both the 10 and 5 nm size colloids is well superimposed on the dye absorption and emission spectra (Figure 3.6), and therefore, we expect a substantial interaction of the plasmon resonance with the dye transitions [66] in both cases. The absorption spectra of the 5 and 10 nm gold NPs can be fit to a single Lorentzian peak superimposed on a smooth $1/\lambda^4$ scattering law according to:

$$y = b + \frac{2A_1}{\pi}\frac{\Gamma_1}{(4(\lambda-\lambda_1)^2+\Gamma_1^2)} + \frac{B_{scatt}}{\lambda^4} \tag{3.17}$$

as shown in Figure 3.6 and Table 3.3.

	$\mathbf{A_1}$	Γ_1 **(nm)**	$\lambda_1(nm)$	$B_{scatt}(nm^{-4})$	**b**
10 nm NPs	8.3±0.5	116±1	530±0.2	1.7 10^9	0.001
5 nm NPs	4.0±0.1	112±2	536±0.2	5.7 10^8	0.001

Table 3.3: *Analysis of the Sav-NP Absorption Spectra.*

The plasmon peak occurs at slightly different wavelengths, 530 and 536 nm (Table 3.3) for the two size of NPs, due to the dependence of the resonance on the particle size and the effect of the surface dielectric constant (here affected by the presence of Sav) on the plasmon peak wavelength [71],[72].

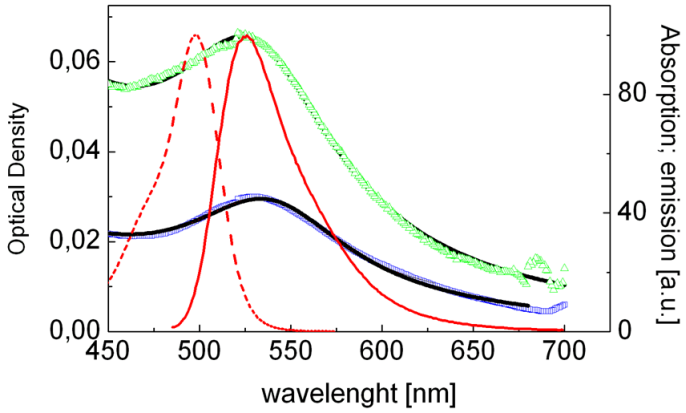

Figure 3.6: *Absorption spectra of the solutions of Sav-NP. Blue squares and green triangles refer to the 10 and 5 nm diameter gold NPs, respectively. The solid lines superimposed on the data are the best fit functions to eq 3.17. The thick dashed and solid red lines refer to the biotin-FITC absorption and emission spectrum.*

3.7.2 Characterization of complexed FITC in solution

We characterized the fluorescence response of biotinilated FITC (pH $\cong$ 7.5) in solution in terms of its fluorescence brightness and excited-state lifetime. In order to reach low limit of detection values, highly diluted (nanomolar to picomolar) solutions were investigated by performing single-particle detection. The excitation mode used here, based on two-photon absorption, allows reducing the contribution of the Rayleigh and Raman scattering to the dye fluorescence emission. Negligible direct absorption of the spherically symmetric gold NPs in the near-infrared (800-1000 nm) is expected for isotropic gold NPs [2] [73], though the nonlinear cross-section of fluorophores bound to the gold surface [9] may be enhanced by the plasmon-fluorophore interaction [74]. The fluorescence

[2]This is not true for non spherically symmetric gold NPs, see chapter 4

traces of 10 nM solutions of FITC coupled to biotin at pH=7.5 are relatively uniform, and the excited-state lifetime histogram can be fit to a single-exponential decay finding $\tau_{FITC} = 3.50\pm$ 0.05 ns (computed over 10 measurements of 10^5 photons each) as shown in Figure 3.8. The brightness (fluorescence rate per molecule) can be obtained, by FCS measurements, from the average fluorescence rate divided by the number of molecules in the excitation volume, $\epsilon = \langle F(t)\rangle \,/\, \langle N\rangle$. The diffusion time and average number of molecules per excitation volume are derived from the fitting of the fluorescence ACFs to eq 3.11 [75],[76]. This procedure provides the value $\tau_D \cong 85 \pm 15\mu s$ that corresponds to a translational diffusion coefficient D = 300 $\pm 30\mu m^2/s$, in agreement with literature results [18]. The FITC brightness at an average excitation power of 100 mW is $\epsilon \cong 4.2\pm$ 0.9 KHz/molecule.

Hereafter the characterization of the constructs based on gold NPs decorated with the FITC dye and the specific protein antibody is reported. The constructs have been first tested for the detection of the model protein BSA and then it has been applied to the recognition of the p53 protein.

3.8 Detection of the model protein BSA

3.8.1 Gold NP-FITC complexes in the absence of BSA

When the biotin-FITC is bound to the gold NP (NP-FITC-Ab, Figure 3.2) the fluorescence fluctuations correlate over relaxation times systematically longer than that of free FITC diffusion (Figure 3.7) that correspond to the best fit values D=9 $\pm$ 4 μm^2/s (5 nm gold NP constructs) and 11 $\pm$ 4 μm^2/s (10 nm gold NP constructs). In the case of monomeric NP constructs the diffusion coefficients should be $D_{5nm} \cong 13.3\mu m^2$/s and $D_{10nm} \cong 11.5\mu m^2$/s. [3] If we additionally take into account some aggregation ($N_{agg} \cong$ 10) as suggested by DLS data, we can estimate the average aggregation number from the average size by assuming a fractal shape for the NP aggregates [4]. The aggregation number N_{agg} scales according to the metal colloids fractal dimension [[70],[30]] d_f=1.9 and is related to the aggregate and monomer size by:

$$N_{agg} = (\frac{R_{ave}}{R_{mon}})^{d_f} \tag{3.18}$$

According to the relation $D \cong (k_BT)/(6\pi\eta R_{ave}) = (k_BT)/(6\pi\eta R_{mon})(Nagg)^{-1/d_f}$, we obtain $\langle D_{5nm}\rangle_{agg} \cong 4.2\mu m^2/s$ and $\langle D_{10nm}\rangle_{agg} \cong 3.7\mu m^2$/s. The ACFs fitting (Figure

[3] The dimensions of the NPs, FITC and BSA protein are reported in section 3.6.1.

[4] AFM data (not shown) substantially confirm this hypothesis

3.7) is then compatible with a distribution of sizes ranging from the monomer to small aggregates with N_{agg} = 10-15.

The histograms of the excited-state lifetime of NP-FITC-Ab constructs (Figure 3.8) can be fit by two exponential decays (see Table 3.4) where the weight of the shortest component (0.6-0.8 ns) is $f_2 = 4 - 6\%$. The corresponding average lifetime values are $\langle\tau\rangle \cong 3.1 \pm 0.3$ and 3.2± 0.3 ns for FITC complexed to the 5 and 10 nm gold NPs, respectively.

Construct	$\tau_1(ns)$	$\mathbf{f_2}$	$\tau_2(ns)$	$\langle\tau\rangle\,(ns)$
Biotin-FITC	3.50± 0.05			
NP-FITC-Ab (10 nm)	3.3± 0.1	0.06±0.04	0.8±0.1	3.2±0.3
NP-FITC-Ab (5 nm)	3.2± 0.1	0.04±0.02	0.6±0.1	3.1±0.3

Table 3.4: *Excited-State Lifetime Values for the FITC and NP-FITC-Ab Constructs.*

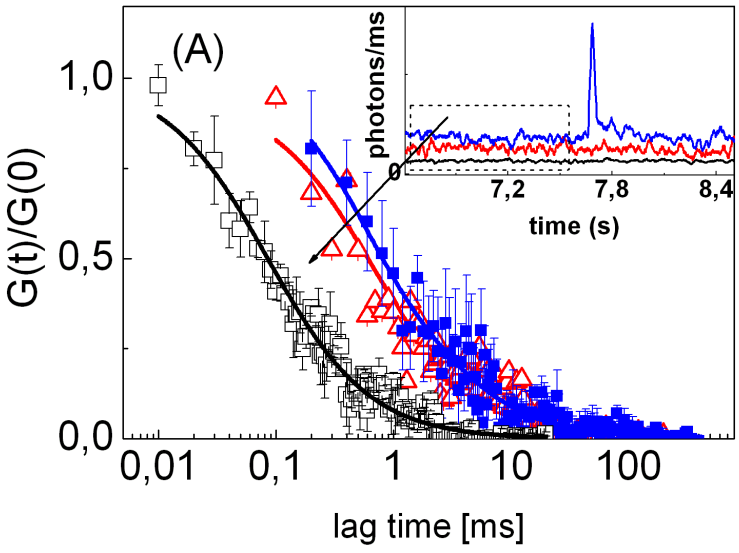

Figure 3.7: *Normalized ACFs of the fluorescence fluctuations measured on a diluted solution of biotin-FITC (open squares) and NP-FITC-Ab constructs for the 5 (open triangles) and 10 nm (filled squares) size in PBS pH 7.5. The lines are the best fit to eq 3.11 with D=300 (black line), 13 (red line), 11 $\mu m^2/s$ (blue line). In the inset the fluorescence traes are shown.*

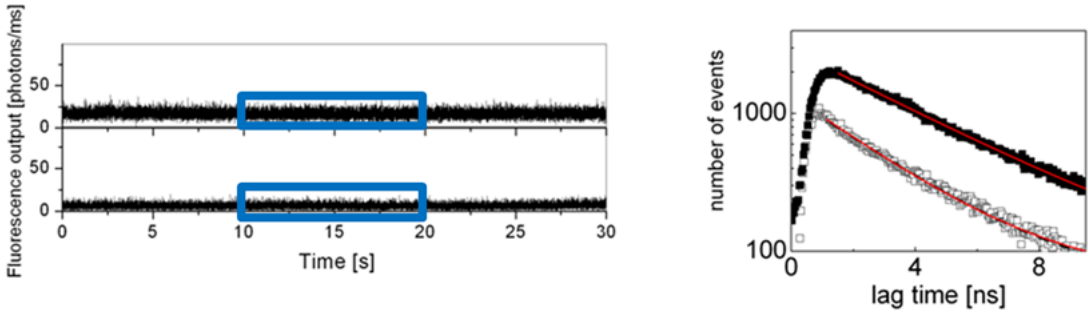

Figure 3.8: *Left: Fluorescence traces of the biotin-FITC (upper trace) and NP-FITC-Ab for the 5 nm NP (lower trace). Right: Excited-state lifetime decays of the biotin-FITC (upper curve) and NP-FITC-Ab for the 5 nm NP (lower curve). Solid lines represent fits obtained with eq 3.8, and the fitting parameters are reported in Table 3.4.*

3.8.2 Protein interactions with the FITC gold NP complexes

We investigated the effect of the binding of BSA to the gold NPs through its specific antibody (Ab) on the FITC lifetime and brightness. These parameters of FITC were monitored as a function of the ratio R = [Ab]:[BSA], in the range 5:1 to 1:1, and with an average concentration of antibodies $\cong$ 1500 and 180 pM for the 10 and 5 nm gold NP, respectively. The concentration of protein was varied in the range 60-1500 pM, and the ratio R_{FITC} between the antibodies and the biotinilated FITC dyes on the gold NPs was kept at 3:1 in all experiments reported hereafter unless otherwise explicitly stated.

3.9 Fluorescence Spectroscopy: Burst analysis

3.9.1 Aggregates size estimate

The time fluorescence traces of (NP-FITC-Ab-BSA) (construct C in Figure 3.2) are shown in figure 3.9 and 3.10 for the 5 and 10 nm NPs at the maximum [Ab]:[BSA] ratio R = 1:1. Several fluorescence bursts are evident. The average width of the fluorescence bursts during the BSA titration experiments can give information on the average aggregate size, and from each burst, the number of photons emitted and the lifetime histogram can be computed. For the maximum ratio R = 1:1 typical burst width values are $\approx$ 150 and 90-100 ms for the 10 (under 40 mW excitation power) and 5 nm (under 100 mW excitation power) gold NPs, respectively. The diffusion coefficients for NPs in the presence of BSA are $D_{5nm} \cong 13.3\mu m^2/s$ and $D_{10nm} \cong 11.5\mu m^2/s$. These values imply average diffusion times of the NPs through the excitation volume, $V_{exc} \cong 0.8\mu m^3$, of approximately $\tau_{D,5nm}$= 4.2 ms and $\tau_{D,10nm}$ 4.9 ms, much smaller

than the observed value of the burst width ≅ 100-60 ms. If we additionally take into account the aggregation number (Table 3.1) we compute values of the diffusion coefficients $\langle D_{5nm}\rangle_{agg} \cong 4.0\mu m^2/\text{s}$ and $\langle D_{10nm}\rangle_{agg} \cong 2.3\mu m^2/\text{s}$, yielding diffusion times $\tau_{D,5nm} = 13.4\pm$ 3 ms and $\tau_{D,10nm} = 25\pm$ 4 ms, still smaller than the experimental data. However, the burst width depends on the excitation power, as shown in Figure 3.9, suggesting the occurrence of optical trapping for the gold NPs. In fact, by performing experiments at decreasing laser excitation power on the 5 nm gold NPs constructs we found that the average burst width decreases linearly with the excitation power (inset of Figure 3.9) and reaches, in the limit of vanishing excitation power, a value of the width ≅ 18 ± 3 ms, in good agreement with the theoretical estimate made above for an average aggregate size of approximately 10 NPs.

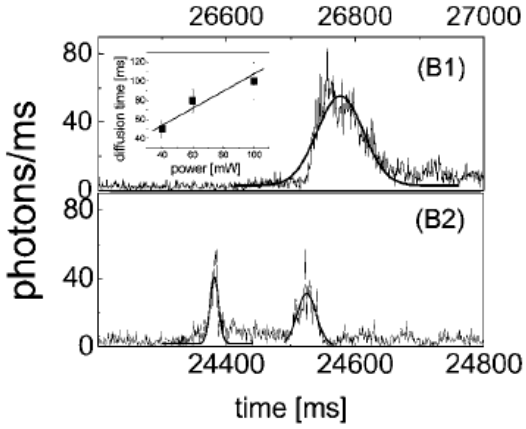

Figure 3.9: *Zoom of fluorescence bursts in a time trace for the NP-FITC-Ab-BSA constructs at R=1:1, excitation power P=100 (B1) and 40 mW (B2). (Inset) Power dependence of the peak FWHM width for the same constructs.*

A further indication in this sense comes from measurements of the recurrence frequency of the fluorescence bursts, $\gamma_R \cong 0.1\pm$ 0.06 Hz (Figure 3.10). A similar value can be recovered by employing the expression

$$\gamma_R \cong 4\pi\omega_0((n)/(N_{agg}))((k_BT)/(6\pi\eta R_{mon}))(N_{agg})^{-1/d_f} \tag{3.19}$$

with a number concentration n ≅ 70-100 pM, a laser beam waist $w_0 = 0.67$ μm, and an aggregation number N_{agg} = 10-20. Therefore, DLS and burst width analysis indicate that, in the presence of BSA, the aggregation is similar to that found for the NP-FITC-Ab constructs, as probed also by FCS. Besides the burst width we can also consider the average value of the total number of photons collected per burst, $\langle N_{BP}\rangle$. In the case of 5 nm NP constructs, we obtain an increase of the average value of N_{BP} when raising the BSA concentration. The value $\langle N_{BP}\rangle \cong 3000\pm$ 300 photons/burst found for

the ratio R=[Ab]:[BSA]= 5:1 increases to $\langle N_{BP} \rangle \cong 7200 \pm 900$ photons/burst for the ratio R=[Ab]:[BSA]=1:1 (100 mW of laser power). The value of $\langle N_{BP} \rangle$ for the 10 nm gold NPs, on the contrary, is almost independent of the stoichiometric ratio R giving $\langle N_{BP} \rangle \cong 6350 \pm 500$ photons/burst at a power of 40 mW.

3.9.2 Excited state lifetime in the presence of BSA

When BSA is added to the NP-FITC-Ab constructs, sharp burst are observed in the fluorescence traces (Figure 3.10, red boxes), indicating that this protein is recognized by the constructs. The excited-state lifetime of FITC was then measured on these fluorescence bursts. We checked that the presence of the bursts should not be ascribed to photons coming from scattering bleeding through the green band-pass filter since control experiments, performed on unlabeled gold NPs observed through the same emission filter (band-pass 535/50 nm), have not shown any fluorescence burst (data not shown). The excited-state fluorescence decay appears to be affected by the protein binding to the NP-FITC-Ab constructs, as seen by comparing Figure 3.8 and Figure 3.10(right panels). Upon BSA addition the fractional intensity of the faster component of the lifetime values derived from the histograms calculated on the bursts increases to $f_2 = 30\%$ depending on the [Ab]:[BSA] ratio. On the other hand, the lifetime values computed on the histograms obtained from the fluorescence background signal detected in between the bursts are close to those obtained without BSA. The lifetime decay has been systematically investigated for the NP-FITC-Ab constructs based on the 5 and 10 nm gold NPs as a function of the BSA concentration in standard buffer solutions, and the average time distributions are shown in Figure 3.11. For comparison, the distribution in the absence of protein has been reported on the same plot.

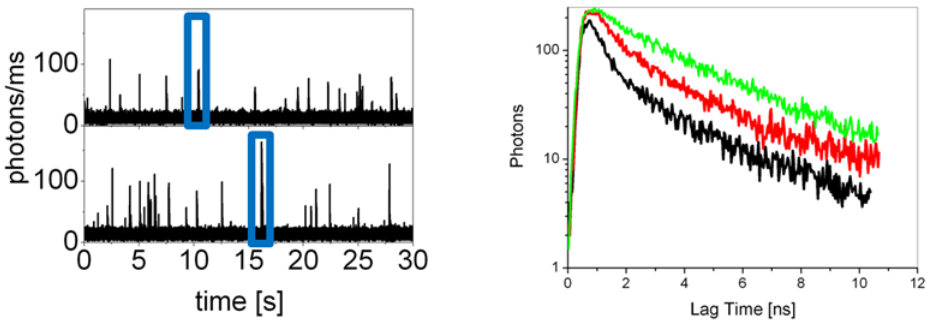

Figure 3.10: *Left: Fluorescence traces of the NP-FITC-Ab-BSA constructs at a molar ratio R=[Ab]:[BSA]=1:1 for the 10 (upper trace, 40 mW excitation power) and 5 nm (lower trace, 100 mW excitation power) NPs. Right: Excited-state lifetime decays calculated on the bursts of NP-FITCAb-BSA 5 nm NPs at R=1:1, bottom curve, and 5:1, middle curve, and calculated on the background (top curve).*

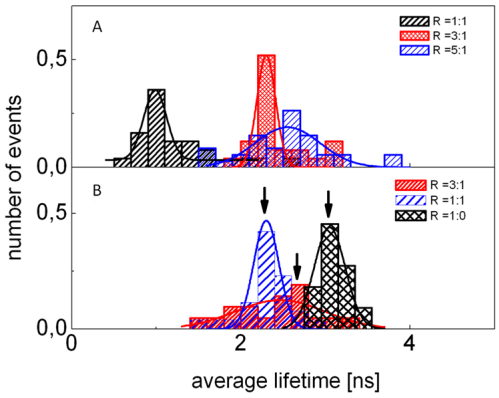

Figure 3.11: *Distribution of FITC average excited-state lifetimes for the NP-FITC-Ab-BSA based on the 5 (A) and 10 nm (B) gold NPs (at the ratio [Ab]:[FITC]=3:1). The solid lines correspond to the Gaussian best fit of the histograms. The stoichiometric ratio R=[Ab]:[BSA] is indicated in the figures.*

The distribution center shifts toward shorter average lifetimes at increasing BSA concentration for both construct sizes due to the increase in the fractional intensity of the shorter component. The result of the data analysis reported in Table 3.5 and figure 3.12 indicates that the 5 nm gold NP construct displays larger sensitivity to the protein-antibody binding than the 10 nm constructs. The change of the protein concentration from ≈ 40 to ≈ 180 pM induces a decrease in the mean excited-state lifetime for the 5 nm gold NP constructs from 2.7 ± 0.1 to 0.9 ± 0.2 ns, mostly due to metal induced quenching of FITC dyes. These are in fact bound to an estimated distance from the gold surface of the order of 3-4 nm and therefore lie in a region where the quenching mechanism due to nonradiative energy transfer is dominant though metal-enhanced fluorescence (MEF) may begin to play a role [77],[78] as indicated by the slight anticorrelation between $\langle N_{PB} \rangle$ and $\langle \tau \rangle$ (Figure 3.13), which can be considered as a MEF fingerprint.
For the 10 nm sized NPs, contrary to the 5 nm constructs, the average number of photons emitted does not show appreciable changes, in agreement with the constant value found for the mean lifetime that reaches a 'saturation' value of $\overline{\langle \tau \rangle} = 2.3 \pm 0.2$ ns, already at the lowest protein to antibody ratio explored (Table 3.5). It should be noticed that a change in the lifetime is indeed occurring also for the 10 nm constructs upon BSA binding for [BSA] $<$ 100-150 pM though with a reduced sensitivity since the maximum change in the lifetime is ca. -30% compared to the ca. -70% decrease found for the 5 nm constructs. Therefore, the parameter that appears to be the most robust and sensitive to the protein concentration is the average lifetime of FITC on the 5 nm constructs that is linearly dependent on the BSA concentration in solutions (Figure 3.12). This behavior can be exploited as a calibration for detection of unknown BSA concentration in solution.

The experimental uncertainty of 0.1 ns on the mean lifetime limits the sensitivity of the technique to a protein concentration of ≈ 5 pM, thereby allowing detection of traces of protein in solution.

$\overline{\langle\tau\rangle}$ **(ns)**	$\langle N_{BP}\rangle$	**R=[Ab]:[BSA]**	**[BSA] (pM)**
10 nm diameter			
2.3±0.1	6700± 400	1:1	1500
2.3±0.1	8400± 1200	2:1	1000
2.5±0.2	6050±350	3:1	500
5 nm diameter			
0.9±0.2	7200± 900	1:1	180
2.3±0.1	7200± 1000	3:1	60
2.7±0.1	3000±300	5:1	36

Table 3.5: *Excited-State Lifetime values for the NP-FITC-Ab-BSA constructs. Effect of the binding of BSA to NP-FITC-Ab on the excited-state lifetime of FITC: the data reported refer to the constructs B in Figure 3.2 with [FITC]:[Ab]=1:3. The binding of BSA is performed at different stoichiometric ratios R=[Ab]:[BSA]. The reported excited-state lifetimes of FITC are the mean of the average lifetime distributions.*

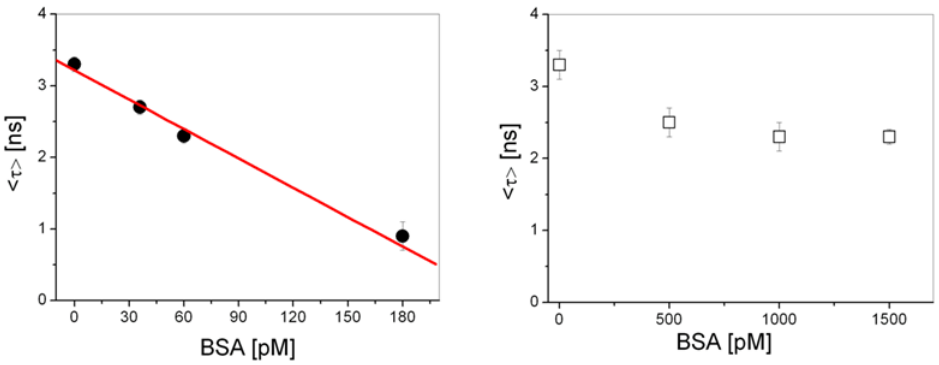

Figure 3.12: *Left: Mean lifetime of FITC in NP-FITC-Ab-BSA constructs for 5 nm NPs versus the concentration of protein in solution. The solid line is a linear fit of the data leading to* $\langle\tau\rangle = 3.2(\pm0.1) - 0.026(\pm0.002)$ *ns* pM^{-1} ** [BSA]. The point at [BSA]=0 corresponds to the value measured on the NP-FITC-Ab construct (Table 3.4). Right: Mean lifetime for the 10 nm constructs versus BSA concentration.*

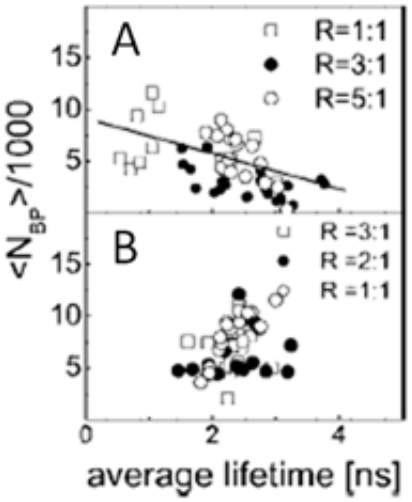

Figure 3.13: *Average number of fluorescence photons per burst versus the average excited-state lifetime of NP-FITC-Ab-BSA constructs for the 5 (A) and 10 nm (B) NPs. The solid line is a linear fit to the data. The stoichiometric ratio R=[Ab]:[BSA] is indicated in the figures.*

A possible rationale for the observed phenomenon, i.e., the marked sensitivity of the FITC lifetime on the BSA bound to the 5 nm constructs (larger than that found for the 10 nm constructs), can be drawn starting from a few considerations of the metal-dipole interaction theory [77],[78],[79] and the experimental observations reported in the literature [80],[11]. The interaction between a metal surface and a molecular dipole is a complex interplay of different phenomena. First, we recognize the enhancement of the absorption and emission due to the increase in the local field, related to the field reflection on the gold surface [81], and to the surface roughness.[82] In this case we expect a substantial increase in the emission rate with a limited change in the excited-state lifetimes. Actually a slight increase of the lifetime with the amplitude of the surface electric field has been reported [80]. Second, metal-dye interactions also include quenching of the molecular emission due to dipole energy transfer to the surface plasmons and electron-hole couples within the metal (nonlocal effects) which results in a decrease of the dye lifetime and brightness. Third, the dye emission may be enhanced due to the radiation in the far field of a fraction of the energy transferred to the surface plasmons, basically that corresponding to high spatial frequencies in the near field emission of the molecule.[77] In this case we expect to observe an anticorrelation of the excited-state lifetime and the number of emitted photons. In those cases when the chromophores and gold NPs are separated by bulky spacers, such as antibodies that correspond approximately to a distance > 7 nm, the fluorescence is actually less quenched [83]. Quenching is dominating for distances up to a few nanometers [84],[11],[81], and it is largely deter-

mined by the shape of the metal structure, by the dipole orientation with respect to the surface, by the size of the metal particle [78] and by the difference between the dielectric permittivities of the metal and the surface layer [77],[85]. Since in our case the distance between the metal and FITC is only ca. 3-4 nm, we believe that the main result reported here, namely, the change in the FITC lifetime upon BSA-NP binding, is mostly due to a change of quenching efficiency rather than to an effective emission enhancement. To partially support this hypothesis, we can bring the observation of the initial decrease in the lifetime of FITC upon binding to the gold surface (Table 3.4) and of the additional larger decrease induced by the BSA binding (Table 3.5). The tiny increase of the emitted photons per burst, $\langle N_{BP} \rangle$, at rising BSA concentrations (Figure 3.13), on the other hand, can be taken as an indication of the presence of high (and heterogeneous) local electric fields on the surface of the nanoclusters that produces a concomitant increase in the molecular brightness. The gold-induced quenching of FITC is directly related to the Fresnel coefficients at the metal-surface boundary [77]. Their change upon binding of proteins to the surface is determined then by the change in the surface layer dielectric permittivity related to the protein relative concentration on the surface layer. For this reason, we tried to keep larger the concentration of BSA on the surface, while keeping the FITC signal per gold NP cluster at measurable levels. This reasoning has also driven our choice of the ratio [Ab]:[FITC]= 3:1 reported above. As cited in the section 3.3.1, the choice of the ratio [Ab]:[FITC] = 3:1 has provided us with the better sensitivity. FITC bound to constructs prepared at the lower value of [Ab]:[FITC]=1:1 displays a reduced average excited-state lifetime already at [BSA]:[Ab] = 0 with respect to the case [Ab]:[FITC] = 3:1. For example, we found $\langle \tau \rangle = 2.1 \pm 0.3$ ns for the 10 nm constructs prepared at [Ab]:[FITC]= 1:1, more than 30% lower than the [Ab]:[FITC]=3:1 case. Moreover, upon BSA addition the FITC average lifetime increases in the [Ab]:[FITC] = 1:1 constructs up to 30% but with very large uncertainty ($\pm$ 22%). This behavior, which makes the construct prepared at [Ab]:[FITC] = 1:1 less adequate than the case [Ab]:[FITC] = 3:1 for protein assay applications, is due to the interplay of the different mechanisms that have been discussed above. In particular, we find that the increase in the FITC lifetime measured in the [Ab]:[FITC] = 1:1 case is due to a marked increase of the long lifetime component which is also affected by a large variability (data not shown). This behavior is probably related to the increase in the local surface field [80] and its inhomogeneity on the surface of the larger gold NP nanoclusters [86] present in the 10 nm gold-dye constructs. These issues may be also at the basis of the observed reduced sensitivity of the 10 nm gold NPs constructs with respect to the 5 nm constructs. In fact, small colloids are expected to quench fluorescence more efficiently than larger ones since the absorption component of the extinction coefficient is dominant over the scattering

one, which is responsible for the plasmon-induced fluorescence enhancement [78],[15] and this would result in a reduced lifetime. On the other hand, the local field enhancement is expected to be larger and more inhomogeneous on larger, possibly aggregated, structures, such as those expected for the 10 nm NPs constructs, and this would result in an increase of the FITC lifetime [80] for these larger constructs. The fine balancing of these two opposite behaviors would then determine the reduced sensitivity of the 10 nm particles constructs compared to those based on the 5 nm gold NPs described here.

3.10 Basic gold nanocrystal protein sensor

Up to this stage of the project, we reported a detailed analysis of the effect of binding the FITC dye to gold NPs of size in the 5-10 nm range and explored the possibility of using the fluorescence emission of FITC bound to their surface in order to monitor traces of proteins in standard solutions at pH = 7. The data presented and discussed here indicate that the FITC excited-state lifetime is a very sensitive parameter in order to detect tiny amounts of protein in solution with an estimated limit of detection of ca. 5 pM, mostly determined by the statistical accuracy of the lifetime measurement. This value, compatible with the sensitivity of most nanotechnology-based assays, encourages application of this method to other protein systems.
For a direct application of the devised sensor to a protein detection in cellular extracts we should also evaluate its specificity. We expect that the degree of specificity is largely determined by the aspecific protein binding to the gold NP surface with respect to the antibody-protein recognition. It is clear that a better understanding of the fine balance of metal-induced quenching and enhancement that occurs on constructs of different sizes and extent of aggregation would be invaluable for the possibility to design specific protein or DNA assays.
The next steps will then be to devise a sensor sensitive to p53 and to test its specificity against this protein. We first investigate the possibility to sense tiny amount of p53 proteins in buffer solutions and move then to experiments in Total Cell Extracts (TCEs). Finally we test specificity against several globular proteins beside BSA. In fact BSA sensing and specificity may be affected by the high stickyness of all serum proteins.

3.11 p53 protein detection

A modification of the protein sensor construct, called hereafter NP-FITC-Ab_{p53}, has been created on a gold nanoparticle on whose surface we have bound the specific anti-p53 antibody and the FITC dye with R_{FITC}= [Ab]:[FITC]=3:1 (Figura 3.2)

In the fluorescence assay presented here picomolar concentration of the constructs was used and therefore we could discern distinct fluorescence bursts on a much lower background. The diffusion time of the construct through the laser beam waist fall in the tens of millisecond range allowing us to collect several thousands of photons per burst, enough to estimate the lifetime of the fluorophore with a few percent of uncertainty on a single burst. This is actually found in the fluorescence traces acquired on the NP-FITC-Ab_{p53} constructs as shown in Figure 3.14 (inset of panel B). The bursts that occur as multiple peaks were analyzed by multi-component Gaussian fit and the most likely value of their FWHM, assumed here as the diffusion time, was $\langle \tau_D \rangle$=60 ± 10 ms. These values correspond to an average hydrodynamic radius $\langle R_h \rangle$ = 230± 50 nm and to a most likely value $R_h \cong$ 170 nm, substantially larger than the estimated monomer radius, indicating that some degree of aggregation must be present at least when the protein is interacting with the gold constructs.

3.12 Fluorescence burst analysis in solution

The FITC fluorescence emission can be characterized on the fluorescence bursts in terms of the particle brightness and the fluorophore lifetime. As described in the section 3.3.1, the ratio R_{FITC} between the Abs and the FITC dyes on the gold NPs was kept constant at 3:1 in all experiments, with an average constant concentration of Ab ≅ 1000 and 510 pM for the 5 and 10 nm NP, respectively. The fluorescence brightness can be computed by means of PCH methods [67], [68] and the average lifetime is evaluated through the analysis in terms of one or two of exponential components of the FITC fluorescence decay. The size of the constructs was further characterized by the average burst width, Δt, analyzed as a Gaussian function (Figs. 3.14).

It is important to notice that when no protein is added to the NP-FITC-Ab_{p53} constructs solutions, rare if any fluorescence bursts were detected (figure 3.15A) and the lifetime of FITC was determined on the background that we ascribed to the NP-FITC-Ab_{p53} constructs. The average fluorescence brightness is in this case 4.4 ± 1.7 photons/ms. The average brightness of the NP-FITC-Ab_{p53} constructs in the presence of p53, computed by PCH method on the fluorescence bursts, increases to ≅ 50 photons/ms (Fig. 3.14(A), inset), that would correspond to approximately an aggregate of 8 to 10 NPs. This result is in qualitative agreement with the light scattering analysis of the size of the NP constructs reported in section 3.7. The uncertainty in the size measurement and therefore aggregation number, does not allow to draw quantitative conclusions on any possible change in the FITC molecular brightness upon protein binding to the NP surface.

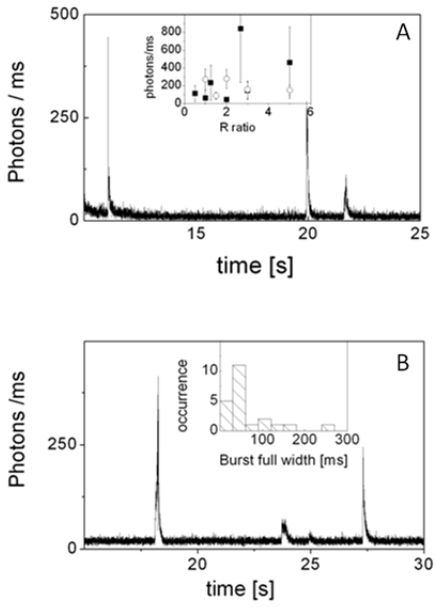

Figure 3.14: *Fluorescence traces collected from R = 1:1 solutions of p53 and 5 nm (panel A) or 10 nm (panel B) NP-FITC-Ab$_{p53}$ constructs. Inset of panel A reports the average particle brightness measured on the bursts for the 5 (open squares) and the 10 nm (filled squares) NP-FITC-Ab$_{p53}$ constructs. Inset of panel B reports the distribution of the bursts full width measured through a multi-component Gaussian fit to the bursts.*

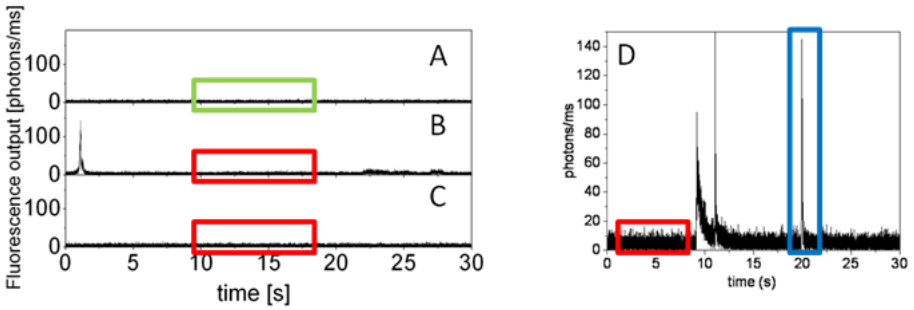

Figure 3.15: *A: Fluorescence traces of the FITC solution. Panels B and C show the fluorescence traces of the constructs NP-FITC-Ab for the 5 and 10 nm size nanoparticles respectively. D: Fluorescence trace in case protein p53 is added to the constructs NP-FITC-Ab for 5 nm size nanoparticles. The lifetime decays are determined on the area selected: $\langle\tau\rangle_{FITC}$ is computed on the green, $\langle\tau\rangle_{FITC-NP-Ab}$ on the red and $\langle\tau\rangle_{FITC-NP-Ab-p53}$ on the blue area.*

We have then analyzed the effect of the protein-antibody recognition on the value of the average FITC lifetime measured on the fluorescence bursts. In the control case in which no protein is added to the solutions the fluorescence decay is well described by a single exponential component (Fig. 3.17(A)) and we measure $\overline{\tau}$=3.4 ± 0.2 and 3.5 ± 0.2 ns for the 5 and 10 nm NP-FITC-Ab$_{p53}$ constructs, respectively. This value is close to that found in solution and reported above, for the biotynilated form of FITC, $\overline{\tau}$= 3.5 ± 0.05 ns (Table 3.6). When p53 is added to the solutions of NP-FITC-Ab$_{p53}$ constructs, the FITC lifetime decreases substantially. Actually, when fitting the histogram decay, a faster component in addition to the ≅ 3.5 ns one is required (Fig. 3.17 (B)). Since the fitting procedure involves the deconvolution of the decay with the system IRF and is therefore affected by some uncertainty, we describe the overall fluorescence decay by the average lifetime $\langle\tau\rangle$, as defined in Eq. 3.10. The average of $\langle\tau\rangle$ over a sample of fluorescence bursts will be indicated as $\langle\overline{\tau}\rangle$.

Construct	$<\overline{\tau}>(ns)$
Biotin-FITC (uncomplexed)	3.50± 0.05
NP-FITC-Ab$_{p53}$ (10 nm)	3.5± 0.2
NP-FITC-Ab$_{p53}$ (5 nm)	3.4± 0.2

Table 3.6: *Excited-state lifetime values for the FITC and NP-FITCAb$_{p53}$ constructs.*

3.13 Dependence of the FITC Lifetime on the p53 Concentration

The effect of p53 concentration on the FITC lifetime has been investigated by changing the ratio R =[Ab$_{p53}$]/[p53] in the range 5:1 to 1:2 (figure 3.16). The protein concentration for these experiments was varied in the range 180-1000 pM for 5 nm NPs and 90-510 pM for 10 nm NPs. The result of the data analysis reported in Figures 3.17(C, D) indicates that both constructs display large sensitivity to protein-Ab binding and that a range of protein concentrations, up to 200-250 pM, can be selected in which the FITC lifetime varies linearly with the protein concentration. The sensitivity of the p53 detection is related to the slope of the linear dependence of $\langle\overline{\tau}\rangle$ upon the p53 concentration, that is:

$$-\delta\langle\overline{\tau}\rangle/\delta[p53] = 0.0014 \pm 10^{-4}[ns/pM] \tag{3.20}$$

and

$$-\delta\langle\overline{\tau}\rangle/\delta[p53] = 0.005 \pm 0.001[ns/pM] \tag{3.21}$$

for the 5 and the 10 nm NP-FITC-Ab$_{p53}$ constructs, respectively. The 10 nm NP constructs appear therefore to be at least five times more sensitive to the p53 detection.

NPs 5 nm

<τ (ns)>	[Ab_p53]/[p53]	[p53] (pM)
3.40±0.2		0
2.99±0.2	5:1	180
2.83±0.2	3:1	275
2.75±0.1	2:1	360
2.70±0.1	3:2	450
2.70±0.1	1:1	1000

NPs 10 nm

<τ (ns)>	[Ab_p53]/[p53]	[p53] (pM)
3.50±0.2		0
3.07±0.1	5:1	90
2.89±0.1	3:1	127
2.78±0.1	4:1.5	140
2.65±0.1	2:1	170
2.63±0.2	1:2	340
2.65±0.2	1:3	382
2.75±0.1	1:1	510

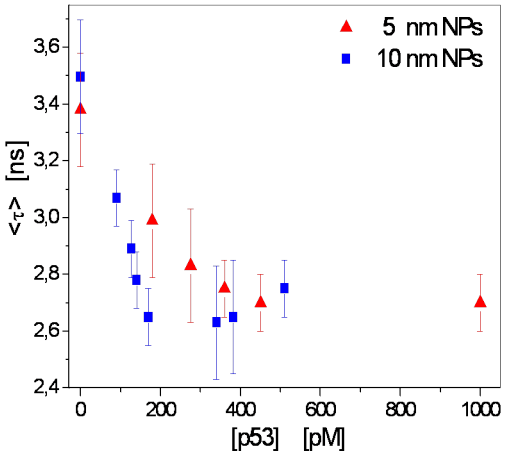

Figure 3.16: *The figure reports the trend of the average lifetime as a function of the p53 concentration and refer to the 5 nm (red symbols) and 10 nm (blue symbols) constructs, respectively.*

As discussed above, due to the uncertainty on the measurement of the FITC molecular brightness and the degree of aggregation of the NP constructs, it is not clear whether the mechanism leading to the observed decrease of the excited state lifetime is related to fluorescence enhancement or rather to aggregation induced quenching. The signature of such a mechanism, related to the metal-mediated increase of the radiative rate of the dye, would be a parallel increase in the molecular brightness and decrease of the lifetime of FITC. As for the data presented here, the molecular brightness is not decreasing upon the dye binding to the metal surface, though we are not in the position to obtain a quantitative evaluation of the possible, metal induced, brightness increase. The presence of two decay components seem to be related to a tight interaction of the dye with the metal or with the streptavidin and antibody layer, with a consequent perturbation of the electronic levels of the dye. These are indeed affected by the subsequent binding of the protein. In fact, the relative fraction of the faster component show only a slight increase when R decreases and the observed decrease in the average lifetime is closely related the decrease of both the relaxation times (Fig.3.18).

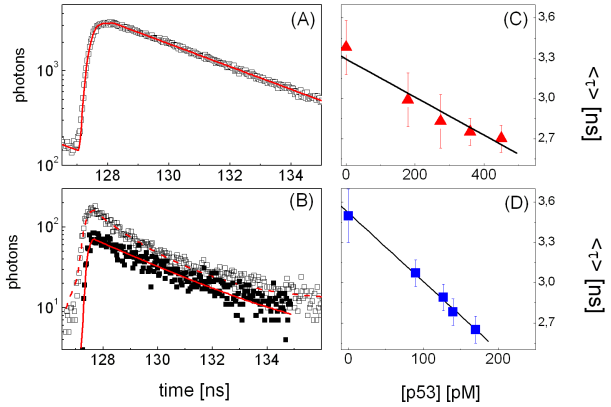

Figure 3.17: *Panel (A): lifetime decays of the NP-FITC-Ab$_{p53}$ construct for the 5 nm NPs in the absence of p53. The solid line corresponds to the best fit of the data to a single exponential decay, τ= 3.5 ns. Panel (B): lifetime decays of the NP-FITC-Ab$_{p53}$ construct for the 5 nm NPs in the presence of p53 at a stochiometric ratio R = 1:1 (upper curve, open symbols) and R = 5:1 (lower curve, filled symbols). The solid lines represent the double exponential decay fit of the data. The fit to the R = 1:1 data gives an average lifetime $\langle\tau\rangle$= 2.2 ns. Panels (C) and (D) report the trend of the average lifetime as a function of the p53 concentration and refer to the 5 nm and 10 nm constructs, respectively. The solid lines are the linear best fit of the data.*

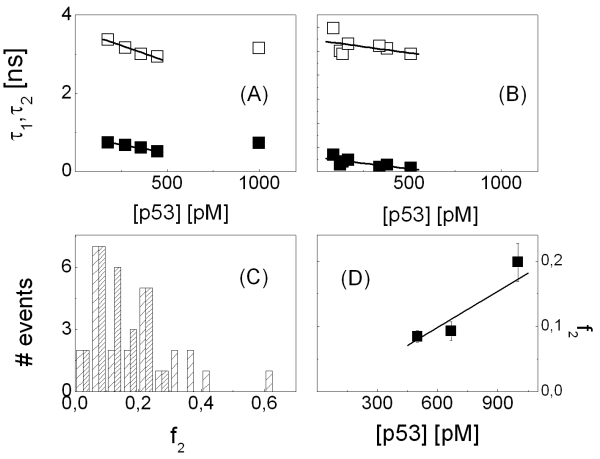

Figure 3.18: *Analysis of the two relaxation components in the fluorescence decay of FITC dyes as a function of the protein concentration in solution. Panels A and B report the lifetimes of the two components with which the fluorescence decay has been analyzed (open symbols τ_1, filled symbols τ_2) for the 5 nm and 10 nm gold NP constructs respectively. Panel C reports the distribution of the fraction, f_2, of the faster component (5nm NP construct) for the stechiometric ratio R=1:1 (sparse pattern) and R=5:1 (dense pattern). Panel D reports the average value of the faster component fraction, f_2, as a function of the protein concentration. The solid lines in all the panels are the best linear fit to the data.*

3.14 In Vitro Selectivity of the p53 Assay

In order to verify the possible use of the proposed p53 assay for in-vivo screening, we must check first for possible false positive results induced by recognition of other proteins present in cell extracts. Regarding the issue of the protein selectivity, we have tested the 5 nm NP-FITC-Ab$_{p53}$ constructs for recognition of small globular proteins that may compete with p53 by specific or aspecific binding to the NPs. p53 is a mainly nuclear protein that can be also found in the cytoplasm [87]. Therefore the possible competitiveness of serum proteins with p53 should not hinder the application of this NP based p53 assay to in vivo tests. We have then tested the competitive binding of BLG and lysozyme, used here as reference globular proteins, for the p53 antibody on the NPs. As a reference for the serum proteins we have taken BSA. Indeed when we add BSA to the NP-FITC-Ab$_{p53}$ constructs we observe large and wide ($\cong$ 3 s) bursts on which sharper bursts are superimposed (Fig. 3.19 (upper panel)).

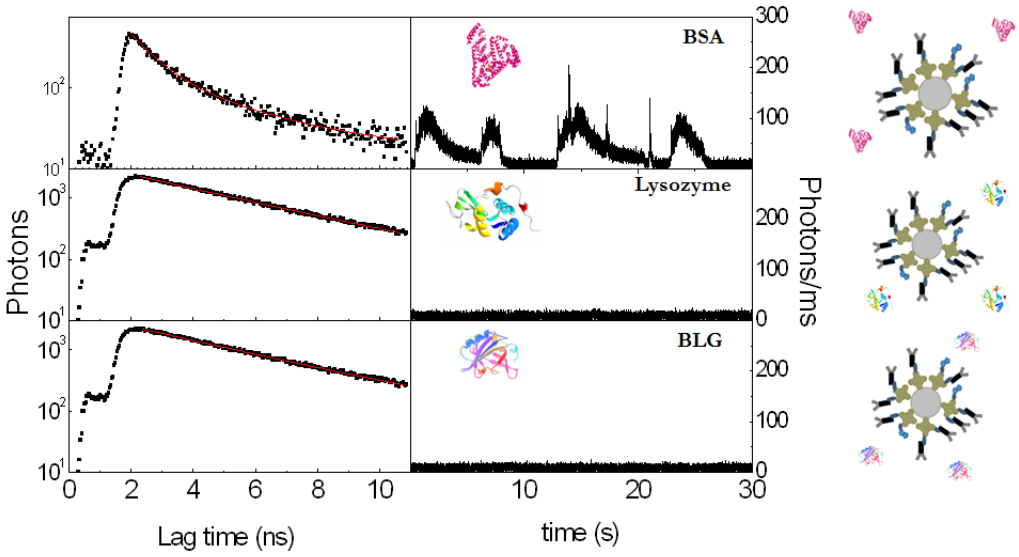

Figure 3.19: *Fluorescence time decay of FITC bound to the NP-FITC-Ab$_{p53}$ constructs (5 nm in size) in the presence of BSA , lysozyme and BLG. All proteins were added to the solution in order to obtain R=1:1. The laser excitation power was 40 mW. The panels on the right report exemplary fluorescence traces for the three proteins.*

This behavior can be taken as an indication of a massive aggregation of the constructs. However, the average FITC lifetime computed on these bursts is definitely smaller ($\langle\overline{\tau}\rangle \cong$ 2.7$\pm$ 0.2 ns) than the reference value of $\tau \cong$ 3.5 ns (Fig. 3.19 (upper panel)). BSA can therefore interfere with p53 detection by the NP-FITC-Ab$_{p53}$ construct. On the contrary, we were not able to observe fluorescence bursts in the case of lysozyme and BLG over

repeated 30 s long traces (Figs. 3.19 (middle and lower panel)), indicating that there is little or no recognition of these proteins by the NP-FITC-Ab$_{p53}$ construct. Moreover, from the single exponential analysis of the fluorescence decays (Figs. 3.19 (middle and lower panel)), we obtained an average FITC lifetime $\overline{\tau} = 3.4\pm$ 0.2 ns for the case of both BLG and lysozyme. These observations indicate that, apart from probably aspecific binding of BSA, the NP-FITC-Ab$_{p53}$ constructs are highly specific for p53 in vitro.

3.15 In Vivo Test of the p53 Assay

The ability of the NP-FITC-Ab$_{p53}$ constructs to recognize p53 in vivo has been tested on extracts from HC116 (p53 positive) and H1299 (p53-null) cell lines. We have first checked the pure TCEs for fluorescence emission at 515 nm finding an average emission of 7.5 $\pm$ 3 photons/ms and a single exponential decay of the fluorescence with average time $\overline{\tau} = 2.6\pm$ 0.1 ns (Fig. 3.20). Also in this case we detected no evident burst over 120 s of measurement (Fig. 3.20 (inset)). This signal is probably due to the auto-fluorescence of the protein bound coenzyme NADH present in the TCEs [88], [89]. When we mixed the p53-null TCEs (p53$^{-/-}$) with the NP-FITC-Ab$_{p53}$ constructs at a 1:1 volume ratio, we found rare bursts with width Δt = 200 ms or larger (Fig. 3.21 A, filled triangles). The distribution of the excited state lifetime indicates the presence of two populations with $\langle\tau\rangle \cong 3.2\pm$ 0.2 ns and $\langle\tau\rangle \cong 2.3\pm$ 0.15 ns (Fig. 3.21 A, patterned bars) with a clear anticorrelation to the burst size (Fig. 3.21 A). We ascribe the two lifetime populations to the emission of FITC bound to the NP-FITC-Ab$_{p53}$ constructs that have not recognized p53 proteins ($\tau \cong 3.1$ ns, as found in the in-vitro experiments) and to the cell proteins auto-fluorescence ($\tau \cong 2.6$ ns). When monitoring the FITC lifetime in a 1:1 (volume ratio) solution of p53$^{+/+}$ TCEs and NP-FITC-Ab$_{p53}$ constructs (Fig.3.21 B), sharp and large bursts appear in the fluorescence traces showed in the inset of Figure 3.20 together with an example of the fluorescence decay. We detect a population of fluorescence bursts characterized by even shorter lifetime values, $\tau \cong 1$ ns, that we ascribe to the complexes of p53 with NP-FITC-Ab$_{p53}$ nano-constructs. Actually, the analysis of the lifetime histogram in terms of a sum of Gaussian functions (Fig.3.21 B, histograms) corresponds to the three values $\langle\tau\rangle = 1.0\pm$ 0.3 ns, 2.0 $\pm$ 0.3 ns and 2.7 $\pm$ 0.3 ns. The two longest ones agree quite well with the values obtained in the p53$^{-/-}$ TCEs (Fig.3.21 A, patterned bars). This conclusion is supported by the control experiments performed by adding free p53 protein to the solution of p53$^{-/-}$ TCEs in the presence of NP-FITC-Ab$_{p53}$ gold constructs. Also in this case we observed sharp and intense fluorescence peaks (Fig. 3.20). As seen in Fig.3.21 A (open symbols), we find three components at $\langle\tau\rangle = 1.1\pm$ 0.2 ns, 1.7 $\pm$ 0.5 ns and 3.2 $\pm$ 0.1 ns (Fig.3.21 A, dashed curves, white bars).

Regarding the possibility to develop a quantitative assay for p53 detection in cell extracts, we suggest that, instead of searching a linear relationship between the average FITC lifetime and the p53 concentration, we should focus on the fraction of bursts that corresponds to the smallest FITC lifetime values ($\cong$ 1 ns). In the data reported in Fig. 3.21 A ($p53^{-/-}$ with addition of p53 in a 1:1 stoichiometry between the antibodies and the p53 protein) and Fig. 3.21 B ($p53^{+/+}$ in a 1:1 ratio between TCE and the NP-FITC-Ab_{p53}), the lifetime component that corresponds to cell auto-fluorescence falls at an average value of FITC lifetime $\langle\tau\rangle_{autof} = 1.9\pm 0.2$ ns. We can therefore count the number of events (fluorescence bursts) that correspond to FITC lifetime $\tau < 1.5$ ns, that corresponds to a 2σ standard deviations from $\langle\tau\rangle_{autof}$. The corresponding fraction is F = 43$\pm$13 % and F = 45 $\pm$ 10 % for the $p53^{-/-}$ (with addition of p53) and for the $p53^{+/+}$ TCEs, respectively. The uncertainty on F is only indicative since it has been evaluated by computing the fractions of events with deviation of one, two and three standard deviations from $\langle\tau\rangle_{autof}$ and taking these as independent measurements. The relatively small uncertainty on the F parameter suggests moreover that F can be used as a measure of the amount of p53 in the TCEs. The close values found in the two experiments indicates that the concentration of p53 in the $p53^{+/+}$ TCEs is of the order of the anti-p53 antibodies in the TCEs, and therefore $\cong$ 500 pM.

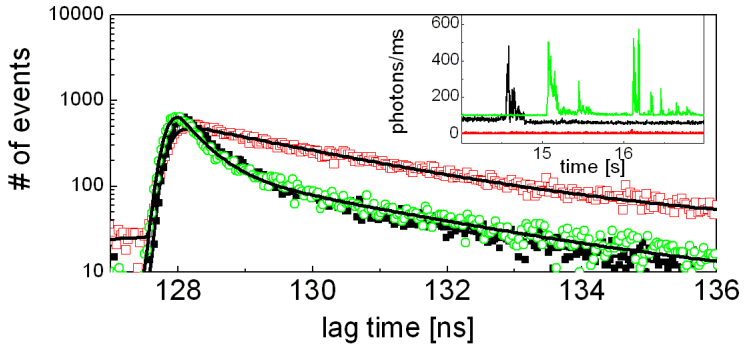

Figure 3.20: *Experiments on TCEs. Fluorescence decay measured from pure TCEs (open squares, red), p53 positive TCEs in the presence of 5 nm NP-FITC-Ab_{p53} constructs (filled squares, black), p53-null TCEs in the presence of 5 nm NP-FITC-Ab_{p53} constructs and with the addition of p53, R = 1:1 (open circles, green). The solid lines are the best fit decays convoluted with the IRF and they correspond to a single exponential decay with τ= 2.6 ns (pure TCEs) and to double exponential decays with $\langle\tau\rangle$=1.5 ns and $\langle\tau\rangle$=1.7 ns for the p53 positive and the p53-null plus p53 cases, respectively. Inset: fluorescence traces for the three cases reported in the main panel: pure TCEs (red), p53 positive TCEs (black) and p53-null TCEs with the addition of p53 protein (green). For sake of clarity two traces have been displaced by 50 and 100 units (photons/ms), respectively.*

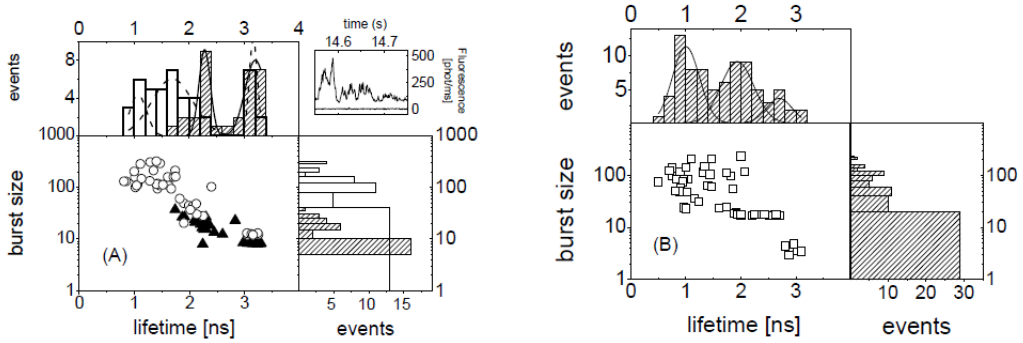

Figure 3.21: *Panel A: number of photons collected per burst as a function of the lifetime for the solutions (1:1 volume ratio) of NP-FITCAb$_{p53}$ constructs and p53$^{-/-}$ TCEs in the absence (filled triangles) and in the presence of (1:1 antibody to p53 stechiometry) p53 protein (open circles). The solid and dashed lines on the lifetime distributions are best fit Gaussian functions of the components. The up-right panel reports a short stretch of fluorescence traces (photons/ms) collected in the absence (lower trace) and in the presence of p53 protein (upper trace). Panel B: number of photons collected per burst as a function of the lifetime for the NP-FITC-Ab$_{p53}$ constructs in p53$^{+/+}$ TCEs (open squares). The solid lines on the lifetime distribution are best fit Gaussian functions of the three components.*

3.16 Conclusion

We have discussed the possibility to use a hybrid nanodevice composed of spherically symmetric gold NPs decorated with specific antibodies to detect tiny amounts of proteins. Focusing on the p53 wt recognition and using FITC dyes (ratio [Ab]:[FITC] = 3:1), we have shown that p53 in vitro detection can be performed by this device by exploiting the linear decrease of the FITC excited state lifetime, measured on the fluorescence bursts, with the p53 concentration. The nanodevice proposed has been also tested for specificity with respect to some exemplary globular proteins and applied to p53 detection in p53 positive and p53 null cell lines. The analysis reported here suggests that the gold NP-FITC-Ab$_{p53}$ nano-constructs can be used to detect the presence of traces of p53 proteins in TCEs opening the way to their application to in-vivo studies. In particular, we suggest to take into account the observed anti-correlation between the burst size and the FITC lifetime value in order to single out the p53-(NP-FITC-Ab$_{p53}$) complexes from auto-fluorescence and un-bound NP-FITC-Ab$_{p53}$ crystals, and to measure the fraction of the small lifetime events to get an estimate of the p53 concentration in the TCEs.

Bibliography

[1] Anker J. N.; Hall W. P.; Lyandres O.; Shah N. C.; Zhao J.; Van Duyne R. P. *Nat. Mater.*, 7:442453, 2008.

[2] Pita M.; Cui L.; Gaikwad R. M.; Katz E.; Sokolov I. *Nanotechnology*, 19:375502, 2008.

[3] Bizzarri A. R.; Cannistraro S. *Nanomed. Nanotechnol. Biol. Med.*, 3:306310, 2007.

[4] A. J. Haes; R. P. van Duyne. A unified view of propagating and localized surface plasmon resonance biosensors. *Anal. Bioanal. Chem.*, 379:920–930, 2004.

[5] Malmqvist M. *Nature*, 361:186–187, Jan 1993.

[6] He L.; Musick M. D.; Nicewarner S. R.; Salinas F. G.; Benkovic S. J.; Natan M. J.; Keating C. D. *J. Am. Chem. Soc.*, 122:90719077., 2000.

[7] Aslan K.; Lakowicz J. R.; Geddes C. D. *Anal. Bioanal. Chem.*, 382:926933., 2005.

[8] Hutter E.; Fendler J. H. *AdV. Mater.*, 16:16851706., 2004.

[9] Lakowicz J. R.; Gryczynski I.; Malicka J.; Gryczynski Z.; Geddes C. D. *J. Fluoresc.*, 12:299302., 2002.

[10] Stuart D. A.; Haes A. J.; Yonzon C. R.; Hicks E. M.; Van Duyne R. P. *IEE Proc. Nanobiotechnol.*, 152:1332., 2005.

[11] Dulkeith E.; Morteani A. C.; Niedereichholz T.; Klar T. A.; Feldmann J.; Levi S. A.; van Veggel F. C. J. M.; Reinhoudt D. N.; Moeller M.; Gittins D. I. *Phys. ReV. Lett.*, 89:1203002., 2002.

[12] Barnes W. L. *J. Mod. Opt.*, 45:661699., 1998.

[13] Aslan K.; Lakowicz J. R.; Szmacinski H.; Geddes C. D. *J. Fluoresc.*, 14:677679., 2004.

[14] Gueroui Z.; Libchaber A. *Phys. ReV. Lett.*, 93:166108., 2004.

[15] Aslan K.; Lakowicz J. R.; Geddes C. D. *Curr. Opin. Chem. Biol.*, 9:538544., 2005.

[16] Ruppin R. *J. Chem. Phys.*, 76:16811684., 1981.

[17] Rachel A. O. *Rep. Prog. Phys.*, 71:076501., 2008.

[18] Chirico G.; Beretta S. *Phys. ReV. E.*, 60:21482153., 1999.

[19] Prosperi D.; Morasso C.; Tortora P.; Monti D.; Bellini T. *ChemBioChem.*, 8:10211028., 2007.

[20] Flecha F. L. G.; Levi V. *Biochem. Mol. Biol. Educ.*, 31:319322., 2003.

[21] A. J. Levine; J. Momand; C. A. Finlay. The p53 tumour suppressor gene. *Nature*, 351:453, 1991.

[22] C. Whibley; P. D. P. Pharoah; M. Hollstein. p53 polymorphisms: Cancer Implications. *Nature*, 9:95, 2009.

[23] J. C. Bourdon. p53 and its isoforms in cancer. *Brit. J. Cancer*, 97:277, 2007.

[24] B. Vogelstein; D. Lane; A. J. Levine. Surfing the p53 network. *Brit. J. Cancer*, 408:307, 2000.

[25] S. Kumar; A. Mohan; R. Guleria. Prognostic implications of circulating anti-p53 antibodies in lung cancera review. *Eur. J. Cancer Care*, 18:248, 2009.

[26] T. Soussi. p53 Antibodies in the sera of patients with various types of cancer: A review. *Cancer Res.*, 60:1777, 2000.

[27] E. M. Tan; S. J. S. Smolen; J. S. Mcdougal; B. T. Butcher; D. Conn; R. Dawkins; M. J. Fritzler; T. Gordon;J. A. Hardin; J. R. Kalden; R. G. Lahita; R. N. Maini; N. F. Rothfield; R. Smeenk; Y. Takasaki; W. J. Van Venrooij; A. Wiik; M. Wilson; and J. A. Koziol;. A critical evaluation of enzyme immunoassays for detection of antinuclear autoantibodies of defined specificities. *Arthritis and Rheumatism*, 42:455, 1999.

[28] N.-S. Lai; C.-C. Wang; H.-L. Chiang; L.-K. Chau. Detection of antinuclear antibodies by a colloidal gold modified optical fiber: Comparison with ELISA. *Anal. Bioanal. Chem.*, 388:901, 2007.

[29] B. A. Du; Z. P. Li;Y. Q. Cheng. Homogeneous immunoassay based on aggregation of antibody-functionalized gold nanoparticles coupled with light scattering detection. *Talanta*, 75:959, 2008.

[30] Y. Liu; Y. Liu; R. L. Mernaugh; X. Zeng. Single chain fragment variable recombinant antibody functionalized gold nanoparticles for a highly sensitive colorimetric immunoassay. *Biosens. Bioelectron.*, 24:2853, 2009.

[31] Ford J.M.; Hanawalt P.C. Li-Fraumeni syndrome fibroblasts homozygous for p53 mutations are deficient in global DNA repair but exhibit normal transcription-coupled repair and enhanced UV resistance. *Proceedings of the National Academy of Sciences of the United States of America*, 92(19):8876, 1995.

[32] D.-S. Wang; F.-Y. Hsu; C.-W. Lin. Surface plasmon effects on two photon luminescence of gold nanorods. *Opt. Exp.*, 17:11350, 2009.

[33] Cox LS; Hupp T.; Midgley CA; Lane DP. A direct effect of activated human p53 on nuclear DNA replication. *The EMBO Journal*, 14(9):2099, 1995.

[34] A.; Goldfinger N. Rotter V.; Aloni-Grinstein R.; Schwartz D.; Elkind NB; Simons A.; Wolkowicz R.; Lavigne M.; Beserman P.; Kapon. Does wild-type p53 play a role in normal cell differentiation? In *Seminars in cancer biology*, volume 5, page 229, 1994.

[35] Wynford-Thomas D. Cellular senescence and cancer. *The Journal of pathology*, 187(1):100–111, 1999.

[36] Bouck N. P53 and angiogenesis. *Biochim. Biophys. Acta*, 1287:63–66, May 1996.

[37] Oren M. p53: the ultimate tumor suppressor gene? *The FASEB Journal*, 6(13):3169, 1992.

[38] Ko L.J. and Prives C. p53: puzzle and paradigm. *Genes and development*, 10(9):1054, 1996.

[39] Levine A.J. p53, the cellular gatekeeper for growth and division. *Cell*, 88:323–331, Feb 1997.

[40] Hollstein M.; Sidransky D.; Vogelstein B.; Harris C.C. p53 mutations in human cancers. *Science*, 253(5015):49, 1991.

[41] Harlow ED; Williamson NM; Ralston R.; Helfman DM; Adams TE. Molecular cloning and in vitro expression of a cDNA clone for human cellular tumor antigen p53. *Molecular and cellular biology*, 5(7):1601, 1985.

[42] Lu H.; Levine A.J. Human TAFII31 protein is a transcriptional coactivator of the p53 protein. *Proceedings of the National Academy of Sciences of the United States of America*, 92(11):5154, 1995.

[43] Venot C.; Maratrat M.; Dureuil C.; Conseiller E.; Bracco L.; Debussche L. The requirement for the p53 proline-rich functional domain for mediation of apoptosis is correlated with specific PIG3 gene transactivation and with transcriptional repression. *The EMBO Journal*, 17(16):4668–4679, 1998.

[44] Walker K.K.; Levine A.J. Identification of a novel p53 functional domain that is necessary for efficient growth suppression. *Proceedings of the National Academy of Sciences of the United States of America*, 93(26):15335, 1996.

[45] Bargonetti J.; Manfredi J.J.; Chen X.; Marshak D.R.; Prives C. A proteolytic fragment from the central region of p53 has marked sequence-specific DNA-binding activity when generated from wild-type but not from oncogenic mutant p53 protein. *Genes Dev.*, 7:2565–2574, Dec 1993.

[46] Arrowsmith C.H.; Morin P. New insights into p53 function from structural studies. *Oncogene*, 12(7):1379, 1996.

[47] Shaulsky G.; Goldfinger N.; Ben-Ze'ev A.; Rotter V. Nuclear accumulation of p53 protein is mediated by several nuclear localization signals and plays a role in tumorigenesis. *Molecular and cellular biology*, 10(12):6565, 1990.

[48] Dang C.V.; Lee W.M. Nuclear and nucleolar targeting sequences of c-erb-A, c-myb, N-myc, p53, HSP70, and HIV tat proteins. *J. Biol. Chem.*, 264:18019–18023, Oct 1989.

[49] Stommel J.M.; Marchenko N.D.; Jimenez G.S.; Moll U.M.; Hope T.J.; Wahl G.M. A leucine-rich nuclear export signal in the p53 tetramerization domain: regulation of subcellular localization and p53 activity by NES masking. *The EMBO journal*, 18(6):1660–1672, 1999.

[50] Friedman P.N.; Chen X.; Bargonetti J.; Prives C. The p53 protein is an unusually shaped tetramer that binds directly to DNA. *Proceedings of the National Academy of Sciences of the United States of America*, 90(8):3319, 1993.

[51] Pellegata N.S.; Cajot J.F.; Stanbridge E.J. The basic carboxy-terminal domain of human p53 is dispensable for both transcriptional regulation and inhibition of tumor cell growth. *Oncogene*, 11(2):337, 1995.

[52] Milner J. Forms and functions of p53. In *Seminars in cancer biology*, volume 5, page 211, 1994.

[53] Kern S.E.; Pietenpol J.A.; Thiagalingam S.; Seymour A.; Kinzler K.W.; Vogelstein B. Oncogenic forms of p53 inhibit p53-regulated gene expression. *Science*, 256(5058):827, 1992.

[54] Ahn J.; Prives C. The C-terminus of p53: the more you learn the less you know. *Nat. Struct. Biol.*, 8:730–732, Sep 2001.

[55] Hupp TR; Meek DW; Midgley CA; Lane DP. Regulation of the specific DNA binding function of p53. *Cell*, 71(5):875–886, 1992.

[56] Yakovleva T.; Pramanik A.; Kawasaki T.; Tan-No K.; Gileva I.; Lindegren H.; Langel U.; Ekstrom T.J.; Rigler R.; Terenius L.; Bakalkin G. p53 Latency. C-terminal domain prevents binding of p53 core to target but not to nonspecific DNA sequences. *J. Biol. Chem.*, 276:15650–15658, May 2001.

[57] Ashcroft M.; Kubbutat M.H.G.; Vousden K.H. Regulation of p53 function and stability by phosphorylation. *Molecular and cellular biology*, 19(3):1751, 1999.

[58] Wu X.; Bayle J.H.; Olson D.; Levine A.J. The p53-mdm-2 autoregulatory feedback loop. *Genes Dev.*, 7:1126–1132, Jul 1993.

[59] Shen Y.; White E. p53-dependent apoptosis pathways. *Advances in cancer research*, 82:55–84, 2001.

[60] Selivanova G. p53 induction as an indicator of DNA damage. *METHODS IN MOLECULAR BIOLOGY-CLIFTON THEN TOTOWA-*, 203:279–288, 2002.

[61] Khanna K.K.; Lavin MF. Ionizing radiation and UV induction of p53 protein by different pathways in ataxia-telangiectasia cells. *Oncogene*, 8(12):3307, 1993.

[62] Vousden K.H.; Lu X. Live or let die: the cell's response to p53. *Nature Reviews Cancer*, 2(8):594–604, 2002.

[63] Lin D. L.; Chang C. p53 is a mediator for radiation-repressed human TR2 orphan receptor expression in MCF-7 cells, a new pathway from tumor suppressor to member of the steroid receptor superfamily. *J. Biol. Chem.*, 271:14649–14652, Jun 1996.

[64] P. J. Steinbach; R. Ionescu;C. R. Matthews. Analysis of kinetics using a hybrid maximum-entropy/nonlinear-least-squares method: Application to protein folding. *Biophys. J.*, 82:2244, 2002.

[65] S. Freddi; L. DAlfonso; M. Collini; M. Caccia; L. Sironi; G. Tallarida; S. Caprioli; G. Chirico. Excited-state lifetime assay for protein detection on gold colloids-fluorophore complexes. *J. Phys. Chem. C*, 113:2722, 2009.

[66] Y. Chen; J. D. Mueller; P. T. C. So; E. Gratton. The photon counting histogram in fluorescence fluctuation spectroscopy. *Biophys. J.*, 77:553, 1999.

[67] J. D. Mueller. Cumulant analysis in fluorescence fluctuation spectroscopy. *Biophys. J.*, 86:3981, 2004.

[68] M. Caccia; E. Camozzi; M. Collini; M. Zaccolo; G. Chirico. Photon moment analysis in cells in the presence of photo-bleaching. *Appl. Spec.*, 59:227, 2005.

[69] Arakaki A.; Hideshima S.; Nakagawa T.; Niwa D.; Tanaka T.; Matsunaga T.; Osaka T. *Biotechnol. Bioeng.*, 88:543546., 2004.

[70] O. Malcai; D. A. Lidar; O. Biham; D. Avnir. Scaling range and cutoffs in empirical fractals. *Phys. Rev. E*, 56:28172828., 1997.

[71] Link S.; El-Sayed M. A. *Int. ReV. Phys. Chem.*, 19:409453., 2000.

[72] Ung T.; Liz-Marzan L.; Mulvaney P. *J. Phys. Chem. B*, 105:34413452., 2001.

[73] N. J. Durr; T. Larson; D. K. Smith; B. A. Korgel; K. Sokolov; A. Ben-Yakar. Two-photon luminescence imaging of cancer cells using molecularly targeted gold nanorods. *Nano Letters*, 7:941945., 2007.

[74] Gryczynski I.; Malicka J.; Shen Y.; Gryczynski Z.; Lakowicz J. R. *J. Phys. Chem. B*, 106:21912195., 2002.

[75] Berland M.; So P. T.; Gratton E. *Biophys. J.*, 68:694701., 1995.

[76] Berland K. M.; So P. T. C.; Chen Y.; Mantulin W. W.; Gratton E. *Biophys. J.*, 71:410420., 1996.

[77] Maxwell D. J.; Taylor J. R.; Nie S. *J. Am. Chem. Soc.*, 124:96069612, 2002.

[78] Gersten J.; Nitzan A. *J. Chem. Phys.*, 75:11391152., 1981.

[79] Das P.; Metiu H. *J. Phys. Chem.*, 89:46804687., 1985.

[80] Pibrik R.; Aslan K.; Zhang Y.; Geddes C. D. *J. Phys. Chem.*, 112:1796917973, 2008.

[81] Amos R; Barnes W. L. *Phys. ReV. B*, 55:72497254., 1997.

[82] Liao P. F.; Wokaun A. *J. Chem. Phys.*, 76:751752., 1982.

[83] Powell R. D.; Halsey C. M. R.; Hainfeld J. F. *Microsc. Res. Technol.*, 42:212., 1998.

[84] Huang C. C.; Chiang C. K.; Lin Z. H.; Lee K. H.; Chang H. T. *Anal. Chem.*, 80:14971504, 2008.

[85] Hohenau A.; Leitner A.; Aussenegg F. R. *In Surface Plasmon Nanophotonics, Springer: The Netherlands*, 2007.

[86] Podolskiy V. A.; Shalaev V. M. *Laser Phys.*, 11:2630., 2001.

[87] M. Li; C. L. Brooks; F. Wu-Baer; D. Chen; R. Baer; W. Gu. Mono-versus polyubiquitination: differential control of p53 fate by Mdm2. *Science*, 302:1972, 2003.

[88] H. Schneckenburger; M. Wagner; P. Weber; W. S. L. Strauss; R. Sailer. Autofluorescence lifetime imaging of cultivated cells using a UV picosecond laser diode. *J. Fluor.*, 14:649, 2004.

[89] K. Konig; P. T. C. So; W. W. Mantulin; B. J. Tromberg; E. Gratton. Two-photon excited lifetime imaging of autofluorescence in cells during UVA and NIR photostress. *J. Micros.*, 183:197, 1996.

Chapter 4

Non-spherically simmetric nanoparticles

4.1 Introduction

In the last two decades several groups have investigated the changes of chemical and physical properties of materials whose dimensions are reduced to nanometric scales [1][2][3]. These studies highlighted a number of possible applications for nanostructures, which are now employed in biology and medicine for imaging, diagnosis, and therapy, owing to the combination of their unique shape/size-dependent properties, strong absorption/scattering of light with stability and low citotoxicity [4][5][6][7][8]. Among all, gold nanorods and non spherically symmetric NPs in general are found to be more popular and useful for potential applications such as biochemical sensing, biomedical diagnostics, and therapeutics due to possible tuning of their surface plasmon resonance (by increasing their aspect ratio) in the visible and near-infrared region, which is the potential window of the electromagnetic spectrum for in-vivo applications [9][10][5][11][12]. Gold nanoparticles not spherically symmetric can efficiently convert optical energy into heat via nonradiative electron relaxation dynamics [8][13], endowing them with intense photothermal properties. Such localized heating effects can be directed toward the eradication of diseased tissue, providing a noninvasive alternative to surgery [14].
Gold is not the only noble metal with such properties when reduced to nanoparticle size. Silver and Platinum are also used for similar reason though the spectral window is blue shifted. Moreover, a wide field of applications in thermal therapy of cancer involves the use of paramagnetic (superparamagnetic) nanoparticles excited by radiofrequency waves. Engineering of gold nanorods (NRs) with novel properties by controlled synthesis for potential applications is very important, particularly because of the NP toxicity

and interaction with cells. The most popular method for synthesizing gold nanorods involves the seed-mediated approach using cetyltrimethylammonium bromide (CTAB) surfactant as the shape-directing agent [1][8].

In this chapter we report the characterization of asymmetric branched gold nanoparticles obtained using for the first time in the seed growth method a zwitterionic surfactant, laurylsulphobetaine (LSB). LSB concentration in the growth solution allows to control the size of the NPs and the SPR position, that can be tuned in the 700-1100 nm Near Infrared range [15]. The synthesis procedure has been devised by the group of Prof. P.Pallavicini of the University of Pavia (General Chemistry Department).

The samples synthesized with CTAB and LSB have been analyzed with several techniques in order to obtain a complete characterization: from the data obtained through the absorption spectra in the UV-Visible region, the TEM images of the solutions, FCS and DLS experiments, we reached information on the nanoparticles shapes and dimensions.

The second part of the spectroscopic characterization has been performed by employing two photon excitation (TPE), which affects greatly the luminescence quantum yield of the nanorods. In fact, non-linear phenomena such as the TPE, enhance the luminescence intensity of corrugated surface and NPs by many orders of magnitude with respect to the single photon excitation of flat surfaces, improving then the impact of these nanoparticles for cell imaging.

Gold NRs exhibit a high photon to thermal conversion efficiency, with a larger absorption cross-section at NIR frequencies per unit volume than most other types of nanostructures [12]. Based on this feature, anisotropic nanoparticles can be used for diagnostic purposes, by optical imaging, and for therapeutic purposes, by thermal phototherapy [5][11]. It is clear that in order to apply thermal phototherapy in medical field is essential to know the temperature at which colloids interact with cells.
In order to measure the local temperature's rise on the particles surface, induced by the absorption of infrared radiation, a novel sensor was designed based on the conjugation of Rhodamine-B fluorophores to non spherically simmetric gold nanoparticles, at controlled nanometric distances.
The Rhodamine-B lifetime decreases gradually when the value of the temperature is changed by the laser irradiation showing that the sensor is able to play the role of molecular thermometer and it can be applied in vivo for imaging and therapeutic purposes.

4.2 Gold nanoparticles luminescence

The gold metal photoluminescence in the visible range was first reported in 1969 by Mooradian [16]. Although suggested as a band-structure probe, the photoluminescence of noble metals remained relatively unexplored for nearly two decades until 1986, when Boyd [17] reported multiphoton induced luminescence on roughened noble metal surfaces. In recent years, there has been a renewed interest in photoluminescence from metal surfaces, primarily in the photoluminescence from noble metal nanoparticles, generated by their potential biomedical applications.

This may seem counter-intuitive at first, as gold is well known to quench the emission of nearby fluorophores due to back-electron transfer [18]. However, gold itself is able to produce a weak photoemission via interband transitions, and this can be enhanced by many orders of magnitude when it couples with an appropriate plasmon excitation [16][17]. For example, linear photoluminescence from gold NRs can be enhanced by a factor of over a million compared with bulk gold [19], and NRs subjected to pulsed laser excitation are able to emit a strong TPL [20][21][22].

In the above studies the origin of the photoluminescence was attributed to the radiative recombination of an electron-hole pair. Visible photoluminescence process in gold metal begins when an electron in the d band is excited to an unoccupied state in the conduction band (figure 4.2). This creates a hole in the d band, which after some time will recombine with an electron [19][23]. The recombination occurs generally through nonradiative mechanisms, but the hole can also radiatively recombine with electrons from the conduction band. Since the photon absorption will necessarily create d holes at points in the Brillouin zone where the conduction band is vacant, interband radiative relaxation is only efficient when intraband scattering processes move the holes closer to the Brillouin zone coordinate that corresponds to the Fermi level in the conduction band. The peak energy of emitted photons is therefore strongly connected to the energy separation between d holes and the Fermi surface, which near X is roughly 1.8 eV, and near L, 2.4 eV. Due to these separations, visible photoluminescence is generated when the hole recombines with electrons near the Fermi surface (figure 4.2) [21].

Although the quantum efficiency of the photoluminescence from bulk noble metal is very low, tipically of the order of 10^{-10} [16], the luminescence, excited by single photon, was found to be enhanced by several order of magnitude on rough or curved metal surfaces due to the lightning rod effect conventionally described as the crowding of the electric field lines at a sharp metallic tip) [17][24]. A similar enhancement has recently been found for the luminescence of gold nanorods. The luminescence efficiency is six orders of magnitude greater than that found in the bulk because of the lighning rod effect [8]. According to the theoretical studies of the photoinduced luminescence from rough sur-

face of noble metals, the incoming and outgoing fields are proposed to be enhanced via coupling to the local plasmon resonances.

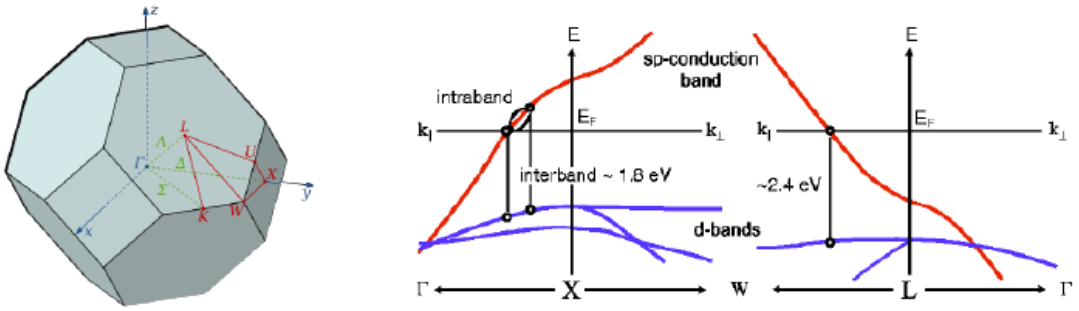

Figure 4.1: *Left: Symmetry points in the first Brillouin zone of gold. Right: Regions of the band structure near X and L close to the Fermi surface. Ref. [25]*

4.2.1 Two-photon luminescence (TPL)

Luminescence primed by multiphoton absorption can be enhanced by many orders of magnitude when coupled to an appropriate plasmon excitation. Multiphoton-induced luminescence was first observed as a broadband background in second-harmonic-generation (SHG) measurements on roughened noble metals [17].
Because the multiphoton luminescence was observed from a roughened metal surface, it is expected a direct involvement of the surface plasmon resonances in the interpretation of the TPL spectra. In particular, the multiphoton luminescence is more sensitive to the local fields (and surface properties) than the single-photon luminescence. Since the local fields are strongest just outside the metal surface, multiphoton-induced emission from the surface atoms dominates over that from the bulk [8].
For two-photon excitation processes, two different schemes have been proposed in literature: a sequence of one-photon excitations and a coherent two-photon excitation. These two cases are distinguished by different behavior on the incident polarizations.
In the first theory, two-photon absorption in gold is a two-step process consisting of two successive one-photon steps, as recently proposed by Imura et al.,[21][26] with the lifetime of the intermediate state, after the first photon absorption, ruling TPL dynamics [27]. The analysis by Imura et al. was supported by the TPL polarization dependence, which was, however, questioned by later experimental results, [22][7][28], so that a strong support to their interpretation is still missing. The excitation mechanism can be hence described as follows (Figure 4.2): upon the optical excitation, the first photon excites an electron in the sp conduction band located below the Fermi surface to the sp conduction

band above the Fermi surface via an intraband transition. At the same time, a hole is created in the sp conduction band below the Fermi level. This transition is resonant with photons with a polarization along the long axis of the nanorod. After the excitation, the memory of the polarization is rapidly lost. Then, the second photon excites a d-band electron to the sp conduction band, where the hole was created by the first photon. The transition by the second photon is not sensitive to the polarization. The second photon generates a hole in the d band. As a consequence, an electron-hole pair is generated, which can recombine to radiate later (10-100 ps) [21] [26].

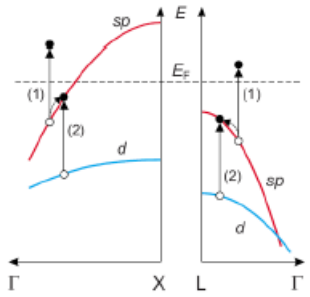

Figure 4.2: *Excitation schemes of sequential one-photon absorptions near the X and L symmetry points. Open and closed circles denote holes and electrons, respectively. Ref. [21][27]*

In the second scheme, two-photon induced photoluminescence in gold is generally considered as a three-step process. Electrons from occupied d-bands are excited by two-photon absorption to unoccupied state of the sp-conduction band. Subsequent intraband scattering processes move the electrons closer to the Fermi level. The relaxation of the electron-hole pair can then recombine either through non-radiative processes or by emission of luminescence. Radiative relaxation energies are therefore strongly connected to the interband separation, and for bulk material these energies are ≅1.5-2.4 eV and occurs around the X and L points of the Brillouin zone [22].

Much of the interest is generated by the potential biomedical applications of nanoparticles [4][5][22][6]. TPL can be spectrally separated from tissue autofluorescence and the power densities required for TPL imaging are orders of magnitude below the damage threshold of biological tissue.
The nanorods' intrinsic TPL properties are useful for real-time imaging in vitro and in vivo, as demonstrated by characterization of their uptake into cells [5] [7] and by monitoring their blood residency in animal models [22]. Most recently, it has been found that gold nanorods are powerful agents for mediating the photothermal destruction of tumor cells, and the TPL can be used to obtain insights into their ability to inflict photoinduced injury [5].

4.3 Experimental details: synthesis and characterization

4.3.1 Nanoparticles synthesis

In a typical preparation [1] gold nanoparticles (NPs) seed solution is obtained by mixing 5 mL of $5{\cdot}10^{-4}$ M $HAuCl_4{\cdot}\ 2H_2O$ with 5 mL 0.20 M LSB (Laurylsulphobetaine N-dodecyl-N', N"-dimethyl-3-ammonio-1-propane-sulphonate) in water, and by adding 600 μL of $NaBH_4$ 0.01 M, obtaining the typical brownish colour of a few-nm sized Au NP dispersion. TEM (Transmission Electron Microscopy) reveals the formation of spherical NP with d<4nm. Growth solutions were prepared with 5 mL of LSB of varying concentration (0.2-0.6 M range), 180-550 μL 0.004 M $AgNO_3$, 5 mL 0.001 M $HAuCl_4{\cdot}\ 2H_2O$ and 70 μL ascorbic acid. After the addition of ascorbic acid, the solution became colorless. Addition of 12 μL of seed solution made the growth solution to become first grey, then to develop a deep blue-violet color. The concentrations and volumes are identical to those that, with 0.2 M CTAB instead of LSB, were reported to produce nanorods (NR) (AR<4.5, LSPR < 850nm) [29].
In order to obtain pegylated gold NPs, the sample obtained with 0.2 M CTAB was ultracentrifuged (13000 RPM for 20 min), the surnatant solution was removed and the obtained pellet was redissolved in 10 mL of bidistilled water. The dispersion was then treated with 1.0-1.1 mg of PEG2000-SH polymer (Iris Biotech, MeO-PEG-SH, MW:2000Dalton), corresponding to $\approx$ 1:10 Au/PEG2000-SH molar ratio, with respect to the total starting Au moles [15].

4.3.2 Cell culture

Cellular uptake experiments have been performed on HEK293 and macrophages cells. 24 hours before the experiments, 10^6 cells per well have been plated on tissue 6 wells plates in Dulbecco's modified Eagle's Medium (DMEM) supplemented with 10% heat-inactivated fetal calf serum, 2 mM LGlutamine, Penicillin-Streptomycin (EuroClone), at 37 °C in a 5% CO_2 atmosphere. The culture medium has been replaced with phosphate buffer solution (PBS) at pH 7.2-7.4 30 minutes before the start of the measurements.
The MTT assay, MTT [3-(4,5-dimethylthiazol-2-yl)-2,5-diphenyl tetrazolium bromide], has been used to test cytotoxicity of reagents and cell viability. The MTT Cell Viability Assay is a safe, sensitive, in vitro assay for the measurement of cell proliferation or, when metabolic events lead to apoptosis or necrosis, a reduction in cell viability. Cells are cultured in flat-bottomed, 12-well tissue culture plates. The tetrazolium compound MTT is added to the wells and the cells are incubated. MTT is reduced by metabolically

[1] collaboration with the group of Prof. P.Pallavicini of the University of Pavia (General Chemistry Department, Pavia)

active cells to insoluble purple formazan dye crystals; then DMSO is added to the wells, solubilizing the crystals so the absorbance can be read using a spectrophotometer at the absorbance wavelength of 570 nm. The formazan concentration is a parameter related to cell viability.

Spectral characterization

Spectrophotometric measurements were performed on a Jasco V570 spectrophotometer (Jasco, Japan).

Dynamic light scattering characterization

For Dynamic Light Scattering (DLS) a home-made setup for variable angle measurement of the scattered light autocorrelation function has been used with a He-Ne 30 mW polarized laser source. The correlator board was an ISS (Urbana Champaign, IL) single photon counting acquisition board and the data were analyzed as described in section 4.5.

Fluorescence Spectroscopy: FCS measurement

A brief description of the set-up is reported in section 3.4.
The excitation polarization was modified using half and quarter waveplates. The fluorescence signal was split by a polarizing or non-polarizing beamsplitter cube and detected by two SPAD. Using linearly or circularly polarized excitation light (denoted as X or C), we derived auto-correlation and cross-correlation functions from two channels that detect linearly polarized or non-polarized emission light (denoted as XX, XY, or NP, depending on the configuration of the polarization for each channel). We measured FCS curves for all investigated samples. They all displayed two distinct decays: one correlation contribution with a characteristic relaxation time on the order of milliseconds, which is attributed to translational diffusion through the confocal observation volume; and a second contribution decaying on shorter time scales, and which is strongly dependent on the polarization configuration.
In order to study the dependence of the TPL signal on the excitation polarization an half-wave plate was inserted in the optical path right below the objective in order to rotate the polarization of the incident radiation.

The TPL emission spectra were recorded by means of a CCD (DV420A-BV, Andor, IRL) based spectrometer (MS125, Lot-Oriel,UK), connected to the backport of the microscope. The excitation wavelength is variable in the range 730-920 nm with a constant average power on sample of about 2 mW. Each of the spectra is the result of the accumulation of 10-20 1 s time acquisitions.

Fluorescence Microscopy

The laser source is a mode-locked Ti:Sapphire laser (Mai Tai, Spectra Physics, CA) pumped by a solid state laser at 532 nm that produces pulses with $\cong$ 100 fs FWHM, repetition rate = 80 MHz and average power $<P> \cong$ 2.8 W at λ= 800 nm at the output of the laser source. The optical set-up is built around a confocal scanning head (FV300, Olympus, Japan) mounted on an optical microscope (BX51, Olympus, Japan) modified for direct (non de-scanned) detection of the signal. The laser beam is sent to the scanning head and is driven on the sample by means of two galvanometric mirrors and a scan lens: the galvos are responsible for the specimen scan while the lens assures that the back aperture of the objective (N.A. = 0.95, 20X, water immersion, Olympus, Japan) is overfilled during the entire scan process. The objective simultaneously focuses the laser beam on the sample and collects, in epifluorescenc geometry, the harmonic or fluorescence signal through either the descanned (FV300) or the non-descanned detection unit. TPL emission is filtered through a short-pass 670 nm filter (Chroma Inc., Brattelboro, VT) and selected by a band-pass filter at 535 nm (Chroma Inc., Brattelboro, VT, full width = 50 nm).

4.4 Results

4.4.1 UV-Vis characterization

The extinction spectra of the NPs are shown in figure 4.3 : seven sample were synthesized according to the method described in section 4.3.1 with LBS concentration variable in the range 0.2-0.6 M, as shown in the panel.

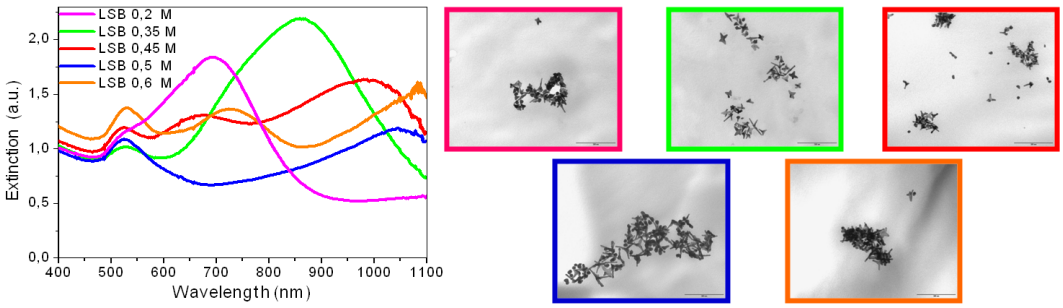

Figure 4.3: *Left: UV-Vis spectra of samples synthesized with LSB surfactant. Right: TEM images; the color of the frames correspond to the absorption spectra.*

Observation of UV-Vis spectra revealed presence of three bands:

1. a major band at λ_{max} 700-1100 nm, depending on LSB concentration ("long" band)
2. a less intense band at 520-530 nm ("short" band)
3. a third band with λ_{max} positioned in the 650-750 nm range, depending on LSB concentration ("intermediate" band)

The 'intermediate band' appears as single peak or a shoulder, depending on the position of the long band. Moreover, its absorbance varied randomly from negligible to comparable to that of the long band. Attribution of the three bands was obtained by TEM images, as descibed in the following paragraphs.
The position of the long LSPR band scales linearly with the LSB concentration (Figure 4.4) and its origin can be assigned by investigating the NR spectrum.

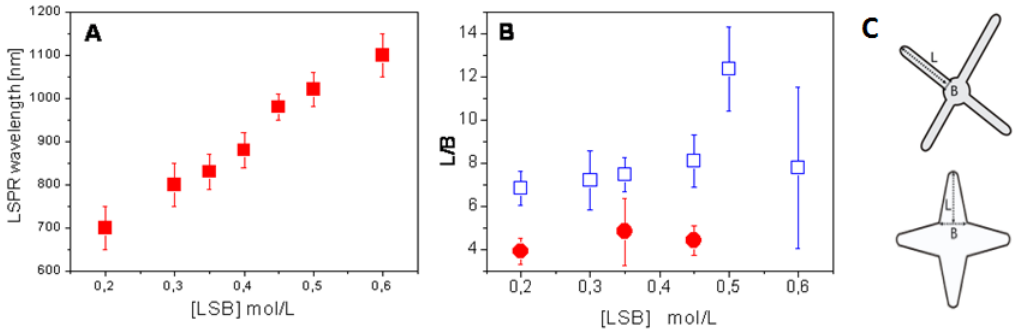

Figure 4.4: *Variation of different parameters as a function of the LSB molarity added to the growth solution. A: LSPR position. B: L/B for type C (blue squares) and type B (red circles) nano-objects. C pictorially represents the ideal shape features of the nanoobjects (L=branch length, B = branch base width)*

In figure 4.5 the extinction spectrum of the sample obtained with 0.2 M CTAB is reported; in this case the solution is homogeneous and presents a single kind of NPs, named nanorods and the spectrum presents only the long and short bands. Therefore we can ascribe the "long" and "short" band to the SPR parallel and perpendicular (which is close to the nanosphere spectrum SPR) to the rod axis.

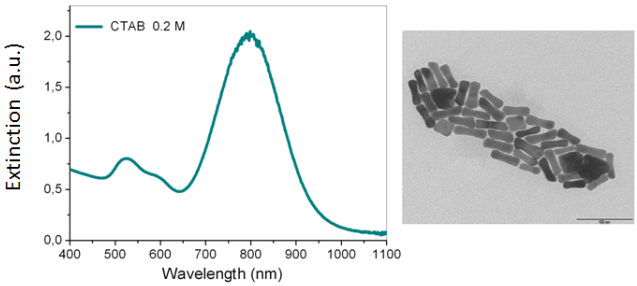

Figure 4.5: *Left: UV-Vis spectra of samples synthesized with 0.2 M CTAB surfactant. Right: TEM image.*

4.4.2 Transmission Electron Microscopy (TEM) characterization

For LSB growth the situation is more complex therefore the structure of the nanoparticles was studied by TEM and correlated to the visible spectrum. Figure 4.6 shows the comparison between the TEM images acquired for nanoparticles synthesized with CTAB and variable concentration of LSB surfactant. The CTAB growth method provides nanorods with well defined aspect ratio; instead, the constructs obtained with LSB exhibit a prevalent star-like structure with thin fingers.

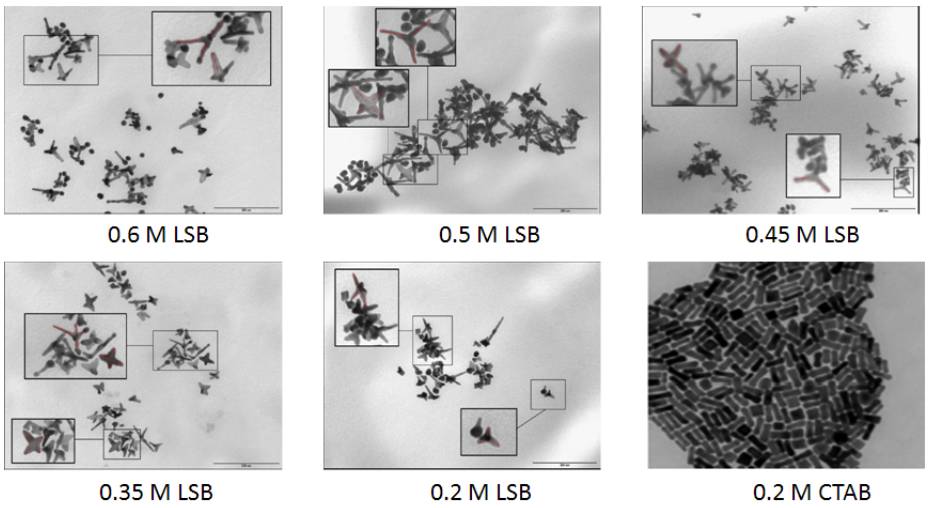

Figure 4.6: *The panels show the comparison between NPs synthesized with LSB or CTAB surfactants.*

In particular, in the image (i) in Figure 4.7, taken on a dispersion from a 0.6M LSB growth solution, three kinds of objects are present: A) nanospheres (< 20 nm diameter); B) nanostars, with large trapezoidal branches (intermediate band); C) branched asymmetric NP, with narrow, long branches (long band) of high aspect ratio AR (Figures

4.7(iii)-(v) display isolated and magnified images of the three typologies).

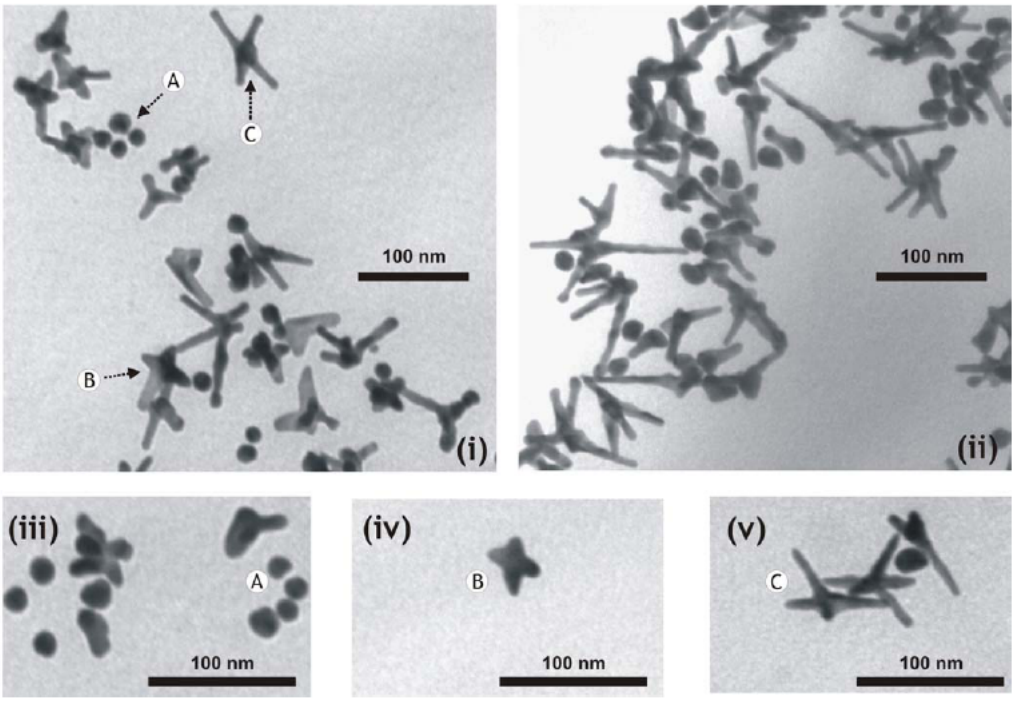

Figure 4.7: *TEM images. (i): obtained from a growth solution prepared with 0.6 M LSB, with a three band absorption spectrum. (ii): obtained form a growth solution 0.5 M LSB, with a negligible intermediate band. (iii) detail of nanospheres (from a 0.6 M LSB growth solution), 30% magnified. (iv) detail of nanostar, (v) detail of branched asymmetric nanoobjects 30% magnified (both from a 0.2M LSB growth solution).*

Image 4.7(ii) has been taken on a dispersion obtained with a 0.5 M growth solution with negligible intermediate band in the UV-Vis spectrum: in this case objects of tipology B are almost absent.
Based on TEM images, it is possible to assign the intermediate band to the B typology objects (nanostars) and of the long band to the C typology objects, in analogy to the GNR case (figure 4.5). The 520-530 nm LSPR band is attributed to the nanospheres, although a contribution to this band may also be due to the transverse LSPR of the larger nanoobjects.

For anisotropic branched NP, the LSPR position has been reported to be proportional to the length/base ratio of the branches (L/B, Figure 4.4) [30] or, similarly, to the length/aperture angle ratio of the branches [31], while it is independent on the number of branches grown on the core [31]. This agrees with the assignment of the intermediate band to the B typology objects (nanostars) and of the long band to the C typology

objects. A plot of the ratio of the length to base width (L/B) of the branches, calculated from TEM images, shows a similar dependence on the LSB concentration for the type C objects (Figure 4.4B, blue squares).
The L/B ratio for type B objects has been calculated only on images from 0.2 to 0.45M solutions (with higher LSB concentrations the tendency of the nano-objects to crop in dense assemblies on the TEM grids prevented graphical evaluations of sizes on the star nano-objects). In each synthesis a ≈ 3 units lower L/B ratio is found for the B population with respect to type C objects, with a slight tendency to increase with LSB concentration (Figure 4.4, red circles).

From TEM images, the dimensions of the different objects can be determined; the length L, the width B and the aspect ratio (L/B), as defined in figure 4.4C, were measured and reported in tables 4.1 and 4.2. The index 1 and 2 refer to C and B object tipology respectively; F_1 is the relative fraction of C type nanoparticles and F_2 of B type NPs.

[LSB] [M]	**L_1 [nm]**	**B_1 [nm]**	**AR_1**	**F_1 (%)**
0.2	54.5±3	8.0±0.8	6.9±0.8	49%
0.35	65.4±5.3	8.7±0.3	7.5±0.6	43%
0.45	60.9±1.9	7.5±1.1	8.1±1.1	59%
0.5	98.9±5.1	7.9±1.2	12.5±1.8	72%
0.6	64.3±11.1	8.2±3.7	7.8±1.4	30%

Table 4.1: *Values of the length, width and aspect ratio of the C type population of nanoparticles synthesized with LSB surfactant. AR is the aspect ratio.*

[LSB] [M]	**L_2 [nm]**	**B_2 [nm]**	**AR_2**	**F_2 (%)**
0.2	35.8±1.9	9.1±1.3	3.9±0.4	38%
0.35	41.0±10.9	8.5±1.5	4.9±1.3	47%
0.45	38.7±5	8.7±0.7	4.5±0.8	30%
0.5	-	-	-	0%
0.6	39.9±4.7	11.4±1.9	3.5±0.5	36%

Table 4.2: *Values of the length, width and aspect ratio of the B type population of nanoparticles synthesized with LSB surfactant. AR is the aspect ratio.*

Also the samples synthesized with the more conventional surfactant CTAB were characterized through trasmission electron microscopy (figure 4.5). In these cases only one typology of nanoparticles is observed; the values of the length L and the width D are reported in table 4.3.

[CTAB] [M]	L [nm]	D [nm]	AR [nm]
0.2	47.9±4.5	17.2±2.1	2.8±0.3
0.2 PEG2000	41.8±3.1	11.2±2.9	3.7±0.9

Table 4.3: *Values of the length and width parameters for the two samples synthesized with the surfactant CTAB. AR is the aspect ratio.*

4.4.3 Z-potential characterization

The nanoparticles solutions are characterized by a ζ-potential value of (-27.2±6.1) mV for 0.3 M LSB concentration and of (-13.4±4.55) mV for 0.45 M LSB: this numeric value indicate that the nanoparticles have a prevalent negative surface charge; the first solution is moderatly stable and the second one is in an incipient instability condition.

The sample synthesized with 0.2 M CTAB surfactant have a ζ-potential of (+14.0±10.5) mV; in this case the prevalent surface charge is negative but the charge distribution is wide and the solution is in an incipient instability form.

4.5 Dynamic Light Scattering characterization

Dynamic light scattering (DLS) measurements substantially validate the picture obtained through TEM. Contribution to scattering of LSB micelles is negligible (pure LSB solutions revealed spherical micelles with diameter increasing from 3.2±0.24 nm to 6.0±0.4 nm when increasing LSB concentration from 0.2 ot 0.6M). In all the suspensions of NPs small, spherical objects are observed (type A NPs, hydrodynamic radius, R_H, 6-10 nm) together with larger ones. The latter display both a rotational and a translational decay of the correlation function, whose values allow to evaluate the amount of depolarized scattering to the correlation function and therefore shape anisotropy [32].

4.5.1 Solutions of LSB (LSB micelles)

Solutions of LSB were prepared in water at increasing concentrations from 0.2 to 0.6 M. The AutoCorrelation Function (ACF) of the intensity of the light scattered at the angle θ= 90° can be fit to a single exponential decay according to the relation:

$$G(t) = \langle I \rangle^2 \left(1 + f^2 exp\left[-2DQ^2 t\right]\right) = \langle I \rangle^2 \left(1 + f^2 \left|g^{(1)}(t)\right|^2\right) \tag{4.1}$$

where Q is the scattering vector, $Q^2 = (4\pi n sin(\theta/2)/\lambda)^2 \cong 3.49 \text{x} 10^{10}$ cm^{-2}, where η is the viscosity, T = 297.15 K, is the solution temperature. The translational diffusion

coefficient D is then translated into the hydrodynamic radius, R_h, by means of the Stokes-Einstein relation:

$$D = \frac{k_B T}{6\pi\eta R_h} \tag{4.2}$$

The signal to noise ratio f (Eq.4.1) is typically ≅0.03. The ACFs reported in Fig. 4.8 indicates clearly that the relaxation time increases with the LSB concentration. Indeed the average hydrodynamic radius changes from R_h≅1.6 nm at [LSB] = 0.2 M, to R_h≅3 nm for [LSB] = 0.6 M, with a linear trend.

[LSB] [M]	**R_h [nm]**
0.2	1.6±0.12
0.3	2.1±0.2
0.4	2.3±0.2
0.5	2.6±0.2
0.6	3.0±0.2

Table 4.4: *Average hydrodynamic radii of micelles in solutions as obtained from polarized VV dynamic light scattering.*

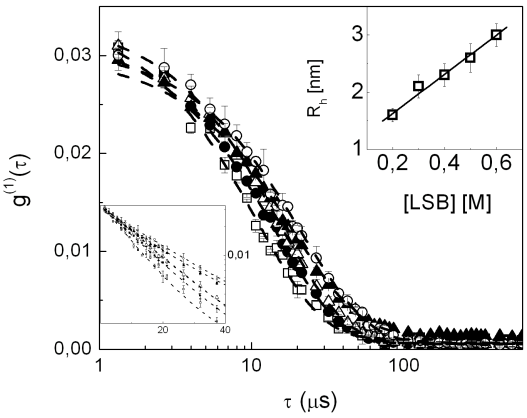

Figure 4.8: *ACFs of the light scattered by the LSB micelle solutions. The symbols refer to [LSB] = 0.2 M (open squares); [LSB] = 0.3 M (filled circles); [LSB] = 0.4 M (open triangles); [LSB] = 0.5 M (filled triangles); [LSB] = 0.6 M (open circles). The dashed lines are the best fit of Eq.4.1 to the data. A small baseline has been added to the data fitting and is probably due to residual dust contribution to the scattering intensity. The top inset shows the linear trend of the R_h as a function of the LSB concentration. The bottom inset shows the ACFs in log-linear scale.*

4.5.2 Dynamic light scattering of the NPs

The scattering of the solutions of the NPs has been measured through a vertical polarizer, i.e. parallel to the direction of the polarization of the laser light. In this case two exponential decays are needed to fit the data with relaxation times of the order 10 and 200 μs approximately (see Fig. 4.9).

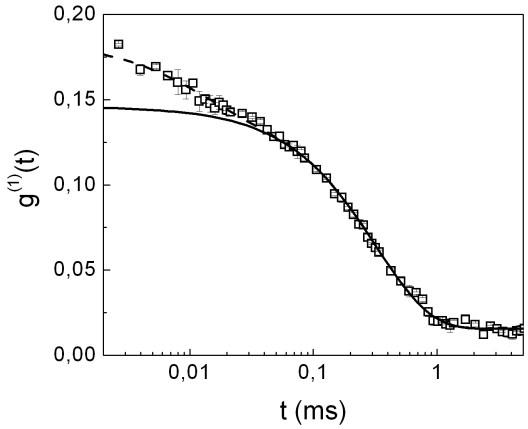

Figure 4.9: *ACF of the light scattered by a solution of NPs prepared at [LSB] = 0.2 M observed through a polarizer whose axis is parallel to the polarization direction of the excitation beam (vertical). The dashed line is the best fit to the function 4.4. The solid line represent the translational component of the ACF. A small baseline accounts for the presence of larger aggregates as also indicated by the TEM analysis.*

The presence of the faster component is taken as an evidence of the polarizability anisotropy of the NPs. In the view of the TEM analysis, the anisotropy of the polarizability is probably entirely due to the shape anisotropy of the NPs. The two relaxation components are then ascribed to the rotational and the translational diffusion of the NPs. According to the TEM image analysis the shape of the NPs may vary from spherical to branched and no clear cylindrical symmetry can be pointed out. The polarizability of the particle is in general a rank two tensor and can be diagonalized to give three eigenvalues that have the meaning of the polarizability along three orthogonal axes in the particle frame of reference. For sake of simplicity, we assume here that we can define in the NP a direction along which the polarizability ($\alpha_{\|}$) of the electrons is much larger than in the other two orthogonal directions ($\alpha_{\perp} << \alpha_{\|}$). Within this assumption, the intensity autocorrelation function can be written in the form [32]:

$$G(t) = \langle I \rangle^2 \left(1 + f^2 exp\left[-2DQ^2 t\right] \left(\langle \alpha \rangle^2 + \frac{4}{45}\left(\alpha_{\|} - \alpha_{\perp}\right)^2 exp[-6\Theta t]\right)\right) \tag{4.3}$$

In the above expression, α indicates the average excess polarizability of the NP, $\alpha_{\|}$ is

the polarizability along the long axis and $\alpha_\perp$ indicate the polarizabilities along the shorter axes (whose mutual difference with respect to $\alpha_\parallel$ can be neglected). The translational, D, and the tumbling rotational, Θ, diffusion coefficients can be used to derive the average hydrodynamic radius of the NP. The amplitudes of the two exponential components are instead used to estimate the degree of shape anisotropy as detailed hereafter. The experimental ACFs are fit then to a trial equation of the type:

$$G(t) = \langle I \rangle^2 \left(1 + Ae^{-\Gamma_T t}(1 + Re^{-\Gamma_R t})\right) \tag{4.4}$$

We assume that the anisotropy along a particle axis is proportional to the length of the axis and therefore:

$$\alpha_\parallel \propto L \tag{4.5}$$

$$\alpha_\perp \propto D \tag{4.6}$$

$$\alpha \propto \frac{1}{3}(L + 2D) \tag{4.7}$$

The ratio of the amplitudes of the translational to the rotational exponential components obtained from the best fit, R_{fit}, is then given by:

$$R_{fit} = \frac{4}{45}\frac{(\alpha_\parallel - \alpha_\perp)^2}{\alpha^2} = \frac{4}{45}\frac{\delta_\alpha^2}{\langle\alpha\rangle^2} \tag{4.8}$$

from which $\delta_\alpha / \langle\alpha\rangle$ can be measured. From Eqs. 4.5-4.8 it is straightforward to derive the (effective) axial ratio, D/L, as:

$$\frac{L}{D} = 3\left(\frac{2\delta_{alpha}}{9\langle\alpha\rangle} + 1\right)\left(1 - \frac{\delta_{alpha}}{3\langle\alpha\rangle}\right)^{-1} \tag{4.9}$$

The best fit values of the ratio δ_α/α are shown in Fig.4.10 and reported in Table 4.5 together with the estimates of the axial ratios, L/D. The comparison to the L/B (length/base) values measured on the branches of asymmetric NP (type C objects, TEM_C in Table 4.5) and on the branches of nanostars (type B objects, TEM_B in Table 4.5) from TEM images indicates that the analysis reported here is substantially in agreement with TEM data.

The nanostars and the branched asymmetric NP (i.e. type B and C) do not give separate contributions in the DLS autocorrelation functions, this meaning that they have similar hyrodynamic radius R_H. Though the average R_H is in fact 23±4 nm, independent of the LSB concentration, the ratio of the rotational to the translational scattering amplitude (R_{fit}) does increase linearly with the LSB concentration (Figure

4.10). Although this cannot be put in direct relation with the L/D ratio, it indicates that the increase of surfactant concentration promotes the formation of objects with increasing shape anisotropy.

[LSB] [M]	$\frac{\delta_{alpha}}{<\alpha>}$	$\mathbf{R}_{h,T}$ **[nm]**	$\mathbf{R}_{h,R}$ **[nm]**	**(L/D)**	$\mathbf{(L/B)}_{TEM_C}$	$\mathbf{(L/B)}_{TEM_B}$
0.2	1.8±0.2	24±2	21±3	5.5±0.9	6.9±0.8	3.9±0.4
0.35	1.9±0.2	29±2	28±4	6.2±0.9	7.5±0.6	4.9±1.3
0.45	2.2±0.3	21±3	27±3	8.9±3.0	8.1±1.1	4.5±0.8
0.5	2.4±0.2	19±3	27±3	13.2±5.0	12.5±1.8	
0.6	2.4±0.2	21±3	25±3	13.6±5.0	7.8±1.4	3.5±0.5

Table 4.5: *DLS amplitude analysis: δ_α/α from eq. 4.8, $R_{h,T}$ and $R_{h,R}$ are the hyroynamic radii, L/D is from eq. 4.9 and $(L/B)_{TEM}$ from TEM measurement. The best fit values of the ratio δ_α/α are obtained from the analysis of the ACFs measured through a vertical polarizer. The hydrodynamic radius, $R_{h,T}$, is obtained from the slower relaxation rate (Γ_T) and Eq. 4.2. The hydrodynamic radius, $R_{h,R}$, is obtained from the faster relaxation rate (Γ_R) and Eq. 4.10. The ratios (L/D) are estimated from Eq. 4.9. The ratios $(L/B)_{TEM}$ are estimated from the analysis of the TEM images on the C and B families of NPs.*

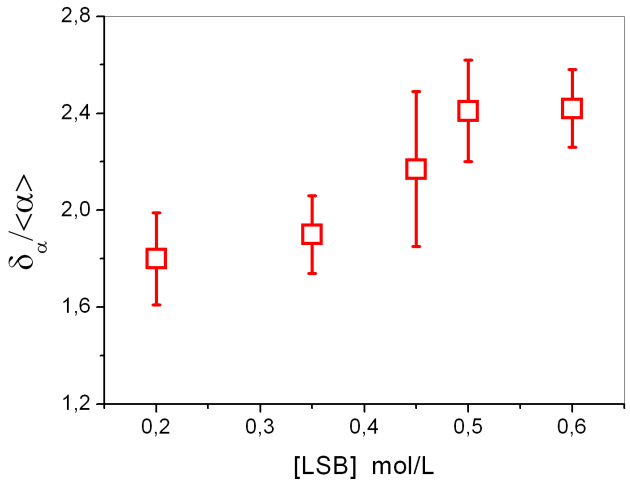

Figure 4.10: *Values of the ratio δ_α/α as a function of LSB concentration.*

Finally, regarding the information that can be obtained from the rotational relaxation rate, $\Gamma_R = 6\Theta$, we observe that to the first approximation we can estimate an average hydrodynamic radius from the relation:

$$\Theta = \frac{k_B T}{8\pi\eta R_{h,R}^3} \tag{4.10}$$

From Eq.4.10 a very rough estimate of the overall encumbrance can be done, reported in Table 4.5, that, however, appears to be consistent with the estimate obtained from the analysis of the translational relaxation rate. The average values of the hydrodynamic radii obtained from the analysis of the translational and rotational components of the ACFs are in fact: $\langle R_{h,T} \rangle = 22.8 \pm 4$ nm and $\langle R_{h,R} \rangle = 26 \pm 3$ nm. A more refined analysis of the rotational relaxation component can be done according to a number of approaches. We assume here the formulation given by Tirado and Garcia de la Torre [33] for the rotational diffusion coefficient of a rod:

$$\Theta = \frac{3k_B T}{\pi \eta L^3} \left[ln\left(\frac{L}{D}\right) + \sigma \right] \tag{4.11}$$

with

$$\sigma = -0.662 + 0.917\frac{D}{L} - 0.05\left(\frac{D}{L}\right)^2 \tag{4.12}$$

From the measurement of the rotational diffusion coefficient, $\Theta = \Gamma_R/6$, and of the axial ratio, obtained above from the amplitudes of the two components of the ACFs, we can gain an additional estimate of the "long" and "short" axes of the effective ellipsoid with which we have approximated the NPs.

	(L/D)	Θ **[kHz]**	σ	$\mathbf{L}_R$ **[nm]**	$\mathbf{D}_R$ **[nm]**	$\mathbf{L}_{TEM}$ **[nm]**	$\mathbf{B}_{TEM}$ **[nm]**
0.2	5.5±0.9	16.6±3	-0.497	65±4	12±2	54.5±3	8.0±0.8
0.35	6.2±0.9	6.9±0.4	-0.515	89±2	14±2	65.4±5.3	8.7±0.3
0.45	8.9±3.0	8.1±0.4	-0.559	91±1	10±4	60.9±1.9	7.5±1.1
0.5	13.2±5.0	8.2±0.5	-0.593	97±2	7.3±3	98.9±5.1	7.9±1.2
0.6	13.6±5.0	10.0±1	-0.595	92±3	6.7±2	64.3±11.1	8.2±3.7

Table 4.6: *Evaluation of the long and short effective axes of the NPs. L/D is taken from R_{fit} and eq. 4.8 and 4.9.* L/D is from table 4.5

The table 4.6 reports the comparison of the estimate of the sizes of the axes of the NPs obtained from TEM and from DLS analysis. The estimates of the long (L_R) and short (D_R) axes are obtained from the rotational diffusion coefficient according to Eq. 4.11-4.12.

When trying to compare the values of length of the long and short axes of the NPs obtained from DLS and from TEM, one should consider that in the analysis of the TEM images, the lengths are taken on the single branches while in the assumptions made for the analysis of the DLS ACFs we have described the whole NP as revolution ellipsoid.

In this sense the overestimation of the length of the long axis observed in Table 4.6, can be understood and the DLS data can be considered consistent with the TEM data.

4.6 FCS experiments

A characterization of the particles average encumbrance and dimensions in physiological medium is fundamental for in vivo applications and it has been performed here by means of the Fluorescence Correlation Spectroscopy (FCS) technique. FCS is a versatile, noninvasive high-resolution technique that takes advantage of the spontaneous intensity fluctuations of the fluorescence signal emitted by extremely low concentrated objects in a focal volume of about one femtoliter. The strength and duration of the fluorescence fluctuations are quantified by temporally autocorrelating the recorded signal: the autocorrelation function is a measure of the self-similarity of the signal after a lag time [34]. In our project, the use of FCS has been aimed at determining the size of anisotropic gold nanoparticles of different shapes (ellipsoidal nanoparticles, called nanorods, and star-shaped nanoparticles, called nanostars) in order to compare them to the DLS and TEM measurements. Moreover FCS has been employed to measure the concentration of NPs stock solution, a basic information needed to use NPs as probes for cellular imaging and to evaluate their toxicity.

NPs luminescence (TPL) was excited by means of TPE. The autocorrelation or cross-correlation functions were computed and the nanoparticles size was determined from the characteristic time of translational and rotational diffusion obtained from the ACF fitting. In fact, the nanoparticles studied here exhibit well distinct time scales for translational and rotational diffusion, which can be separated in the analytical expression of the autocorrelation function: the former is described by a decay with a characteristic relaxation time of the order of milliseconds, while the latter leads to a second decay, expressed by a single exponential function, on the microsecond time scale. Auto-correlation functions were collected by using linearly and circularly polarized excitation light; a strong dependence on the polarization configuration was found in the shape and amplitude of the function on the microsecond time window and made it possible to attribute the decay in this lag time range to rotational diffusion.
Circularly polarized excitation light has been obtained through a $\lambda/4$ waveplate positioned right before the entrance pupil of the objective. In general it is difficult to position the waveplate in order to convert the linearly into fully circularly polarized excitation, so the rotational component τ_R is not completely extincted (see for example figure 4.13) Translational and rotational diffusion constants were extracted from the diffusion times and, by making use of the Stokes - Einstein relations, an estimate of the effective hydrodynamic radius has been obtained. The hydrodynamic radius provides a measure for

the size of the nanoparticles, approximated to spheres, and, when evaluated from the translational diffusion coefficient, it has been found in good agreement with the estimate obtained by means of a transmission electron microscope (TEM). In order to take into account the larger relevance of the difference from the spherical shape, further analysis was conducted for nanorods: their translational and rotational diffusion coefficients have been compared to those obtained through Tirado and Garcia de la Torre's theory [33].

4.7 FCS autocorrelation analysis

Extensive ACFs' analysis has been undertaken to separate the contributions of rotational diffusion and translational diffusion [35][36][37][38]. With typical translational diffusion times being of the order of milliseconds, the rotational diffusion, on the order of microseconds, contributions are well separated in the ACFs. According to Kask et al.[38] and Widengren et al.,[39] the rotational diffusion term of the total auto-correlation function can be separated from the translational diffusion term and, to a first approximation, be written as a single exponential function:

$$G(\tau) = \left(1 + \frac{A}{1-A} e^{-\tau/\tau_R}\right) \frac{G_T(0)}{\left(1 + \frac{8D_T}{\omega_0^2}\right)\sqrt{1 + \frac{8D_t}{\omega_0^2}\left(\frac{\lambda}{\sqrt{2}\pi\omega_0}\right)^2}} \tag{4.13}$$

This analytical expression of the correlation function has been derived assuming spherical diffusors (having isotropic polarizability) and fluorescence lifetimes much shorter than the rotational correlation times. The effective hydrodynamic radius R_h was derived by extracting τ_D and τ_R from the correlation function, determining the diffusion constant D and the rotational diffusion contant Θ, and using the Stokes-Einstein relation:

$$D = \frac{k_B T}{6\pi\eta R_h} \propto \frac{1}{L} \tag{4.14}$$

$$\Theta = \frac{k_B T}{8\pi\eta R_h^3} \propto \frac{1}{L^3} \tag{4.15}$$

where k_B is the Boltzmann constant, T is the temperature, η is the solvent viscosity, R_h is the particle radius and L is the length of nanoparticle's branches.

FCS ACFs were acquired for the samples synthesized with both LSB and CTAB surfactant, diluted from 1:10 to 1:250 respect to the stock concentration .
The fitting of FCS curves acquired with both circular and linear polarized excitation polarization provides the translational and rotational diffusion coefficients D and Θ. From these and eqs. 4.14 and 4.15 we obtain the hydrodynamic radius, which is a first estimate

of the nanopaticle's branch length. Figures 4.11,4.12 and 4.13 show the FCS curves and the distribution of hydrodynamic radii obtained for the samples synthesized with 0.2, 0.45 and 0.6 M LSB surfactant.

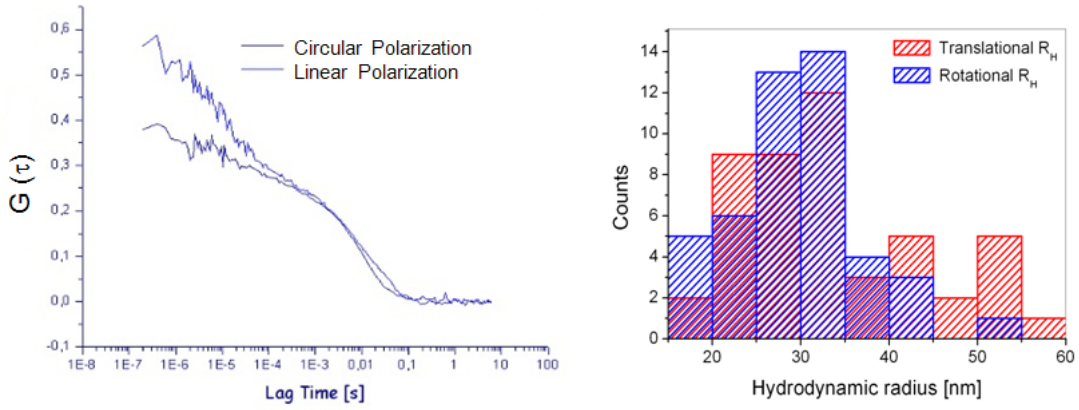

Figure 4.11: *Left: FCS curves obtained with linear and circular polarization. Right: Distribution of the hydrodynamic radii determined through relation 4.14 and 4.15 for sample obtained with 0.2M LSB.*

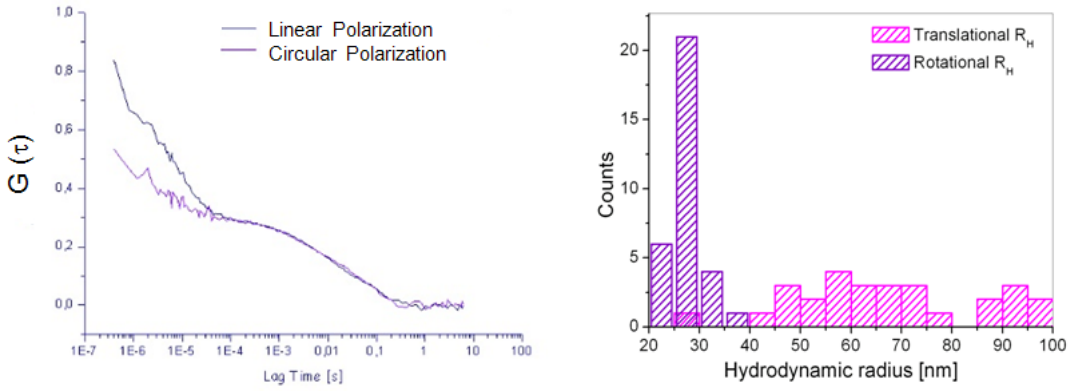

Figure 4.12: *Left: FCS curves obtained with linear and circular polarization. Right: Distribution of the hydrodynamic radii determined through relation 4.14 and 4.15 for sample obtained with 0.45M LSB.*

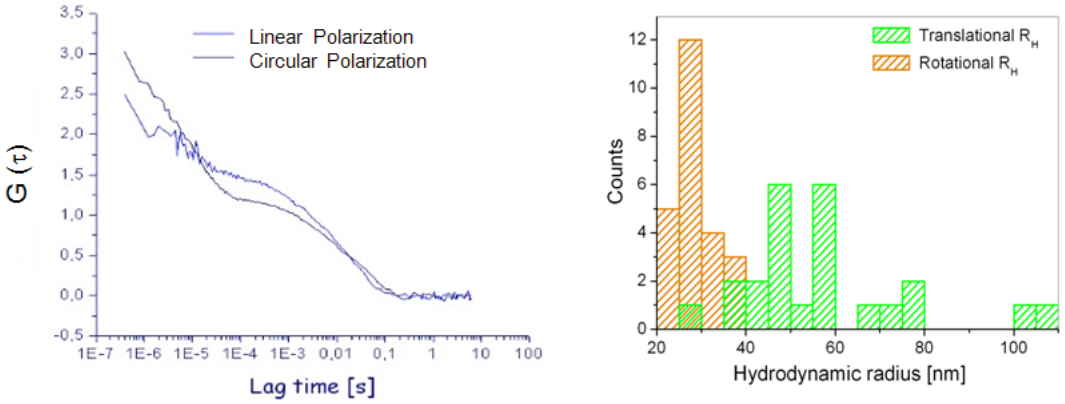

Figure 4.13: *Left: FCS curves obtained with linear and circular polarization. Right: Distribution of the hydrodynamic radii determined through relation 4.14 and 4.15 for sample obtained with 0.6M LSB.*

The best fitting results are summarized in table 4.7: for each sample the mean translational and rotational diffusion times τ_D and τ_R, the diffusion coefficients D and Θ and the mean hydrodynamic radii $R_{h,T}$ and $R_{h,R}$ are reported (table 4.7). For comparison, the branch length derived from TEM images, L_{TEM}, and the aspect ratio $(A.R.)_{TEM}$ are shown in table 4.8 (see also table 4.1).

Sample	τ_R [μs]	Θ [μs^{-1}]	**D** [$\mu m^2/s^{-1}$]	τ_D [ms]
0.2 M LSB	33.1±4.2	0.008±0.001	7.0±0.3	7.8±0.3
0.45 M LSB	22.0±1.7	0.009±0.001	3.5±0.2	15.6±0.8
0.6 M LSB	25.2±2.1	0.008±0.001	4.2±0.3	13.2±0.9

Sample	$\mathbf{R}_{h,T}$ [nm]	$\mathbf{R}_{h,R}$ [nm]
0.2 M LSB	34±2	30±1
0.45 M LSB	67±4	27±1
0.6 M LSB	57±4	29±1

Table 4.7: *The tables show the mean translational and rotational diffusion times τ_D and τ_R, the diffusion coefficients D and Θ and the mean hydrodynamic radii $R_{h,T}$ and $R_{h,R}$ for anisotropic NPs obtained with variable LSB concentration from FCS ACFs analysis.*

Sample	**Population (%)**	**L_{TEM} [nm]**	**$(A.R.)_{TEM}$ [nm]**
0.2 M LSB	49.4	54.5±3.0	6.9±0.8
0.2 M LSB	37.6	35.8±1.9	3.9±0.4
0.45 M LSB	58.8	60.9±1.9	8.1±1.1
0.45 M LSB	30.4	38.7±5.0	4.5±0.8
0.6 M LSB	30	64.3±11.1	7.8±1.4
0.6 M LSB	36	39.9±4.7	3.5±0.5

Table 4.8: *The table shows the values of the branch length derived from TEM images L_{TEM} and the aspect ratio $(A.R.)_{TEM}$.*

The hydrodynamic radii obtained from the translational and rotational diffusion coefficient for the sample synthesized with 0.2 M LSB are in good reciprocal agreement with the DLS measurements (see table 4.5). In particular $R_{h,T} \cong R_{h,R}$ demonstrating that spherical approximation is valid in this case. On the contrary, the radii obtained from D and Θ are different from DLS measurements for samples synthesized with 0.45 and 0.6 M LSB. This reflects the inhomogeneity of NPs populations; in fact, as shown in section 4.4.2, the samples consist of sherical, star-like and NPs with high aspect ratio branches. Because $\Theta \propto L^{-3}$, Θ is largely affected by high aspect ratio branched NPs.

We pass now to the control NPs synthesized with CTAB. The FCS autocorrelation functions for the sample synthesized with 0.2 M CTAB (nanorods) are shown in figure 4.14 and the rotational diffusion coefficients are reported in table 4.9.

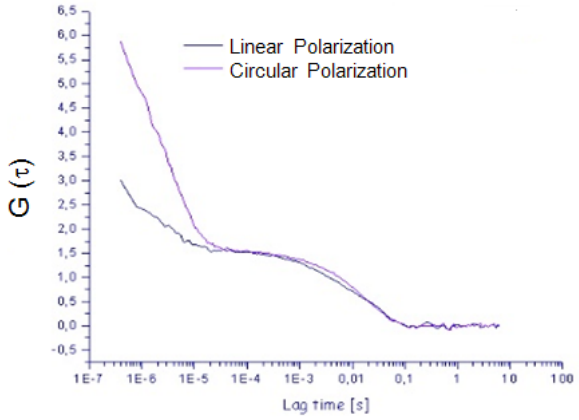

Figure 4.14: *Left: FCS curves obtained with linear and circular polarization. Right: Distribution of the hydrodynamic radii determined through relation 4.14 and 4.15 for sample obtained with 0.2M CTAB.*

Sample	Θ_{FCS} $[\mu s^{-1}]$	Θ_{TG} $[\mu s^{-1}]$
0.2 M CTAB	0.021±0.002	0.024±0.001
0.2 M CTAB+PEG 2000	0.040±0.004	0.047±0.002

Table 4.9: *Rotational diffusion coefficients obtained from FCS data and evaluated from Tirado-Garcia de la Torre relations (eqs. 4.16-4.17).*

The spherical approximation for this kind of NPs is not valid and it was not possible to value their dimensions. However, due to TEM results (figure 4.6), we can assume for this sample the formulation given by Tirado and Garcia de la Torre [33] for the rotational diffusion coefficient of a rod:

$$\Theta = \frac{3k_BT}{\pi\eta L^3}\left[ln\left(\frac{L}{D}\right) + \sigma\right] \tag{4.16}$$

with

$$\sigma = -0.662 + 0.917\frac{D}{L} - 0.05\left(\frac{D}{L}\right)^2 \tag{4.17}$$

where L and D are the nanorod length and width respectively, η is the viscosity and T the temperature. By replacing L and D with the values found in TEM measurement in eq. 4.16, we computed Θ, reported in table 4.9: the values Θ_{TG} and Θ_{FCS} are in good agreement.
The diffusional component was not accounted; it however resulted of the order of 8.5±0.8 $\mu m^2/s$ (for NP obtained with 0.2 M CTAB) and 4.3±0.2 $\mu m^2/s$ (for NPs obtained with 0.2 M CTAB and functionalized with PEG-2000), higher than the value estimated from Tirado-Garcia de La Torre formulation (13.8±0.1 and 18.2±0.1 for NP synthesized with 0.2M CTAB and 0.2M CTAB-PEG2000 respectively)[2] probably due to a residual spherical component.

4.8 Concentration evalutation

As we said, the interest of FCS is in the NP counting. The concentration of the samples, in terms of the number of NPs per excitation volume, was calculated from the G(0)

[2]from the equation:

$$D = \frac{k_BT}{3\pi\eta L}\left[ln\left(\frac{L}{D}\right) + \nu\right] \tag{4.18}$$

with

$$\nu = 0.312 + 0.565\frac{D}{L} - 0.1\left(\frac{D}{L}\right)^2 \tag{4.19}$$

values:

$$G(0) = \frac{\gamma}{N} = \frac{0.076}{N} \tag{4.20}$$

Because ρ_{Au}=19.3 g/cm^3 and the excitation volume and the dilution respect to the stock solution are known, the number of particles/L and also the molar concentration of the stock solution can be derived, as reported in table 4.10:

Sample	**C [nM]**	**C [mg/ml]**
0.2 M CTAB+PEG 2000	8.06±1.73	2.06±0.44
0.3 M LSB	8.6±0.6	1.7±0.2
0.35 M LSB	10.3±2.2	1.5±0.3
0.45 M LSB	6.2±0.4	1.03±0.06
0.5 M LSB	1.05±0.07	0.32±0.02

Table 4.10: *Concentration of the samples synthesized with LSB and CTAB surfactant.*

4.9 TPL dependence on the excitation power

The nonlinear nature of the TPL signal emitted by the gold nanoparticles was confirmed by measuring the dependence of the luminescence intensity I_{TPL} as a function of the average excitation power P_{exc}. Two different samples were evaluated:

- gold nanoparticles synthesized with the surfactant CTAB 0.2 M
- gold nanoparticles synthesized with the surfactant LSB 0.4 M

The excitation wavelenght was set equal to the wavelength of surface plasmon resonance λ_{SPR}, which is λ_{exc}=λ_{SPR}=780 nm for the first sample (CTAB 0.2 M) and λ_{exc}=λ_{SPR}= 900 nm for the second one (LSB 0.4 M) (figure 4.3). The measure was performed on a drop of gold nanoparticles solution dried on top of a coverslip; the signal is obtained averaging 3 images through a 535/50 nm pass band filter. The evaluation of the signal level on the images was accomplished by computing an average on at least 5 different regions of interest (ROIs) taken from bright regions of the image. Signal intensities were collected for increasing incident power from 0 to 2 mW. Figure 4.15 show the log-log plot of the emitted TPL intensity for the samples analysed; a quadratic dependence of the signal intensity I_{TPL} on the input power was observed [22][7][40], with slope values of 2.15 ± 0.16 in the range 0.1-0.8 mW and 1.95 ± 0.04 in the range 0.1-1 mW for the gold nanoparticles synthesized with CTAB and LSB, respectively.

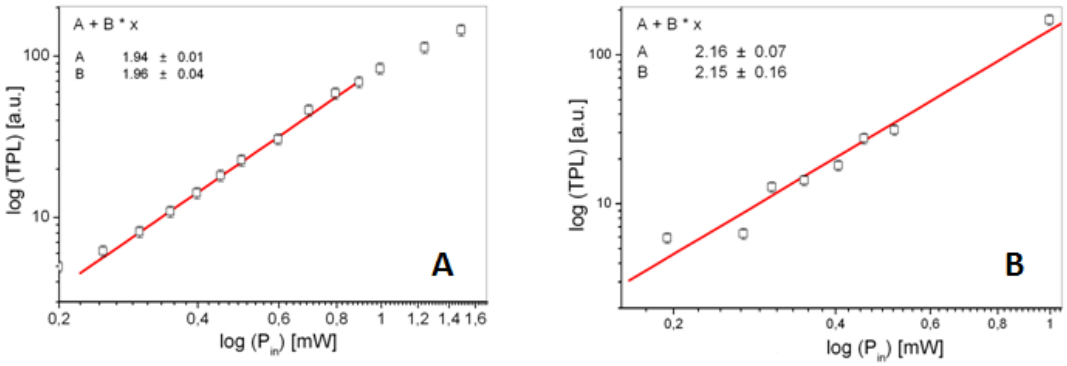

Figure 4.15: *Quadratic dependence of the signal intensity I_{TPL} on the input power for samples obtained with 0.45M LSB(A) and 0.2M CTAB (B).*

To confirm also qualitatively that the emission signal is due to a two-photon excitation process, the laser was switched in the contiuous wave (CW) operation mode. In the CW case (figure 4.16) no signal was emitted by the samples: irradiation of the nanorods in a wide range of power levels reduced the signal to background noise level, confirming the two-photon nature of the nanorod luminescence [40].

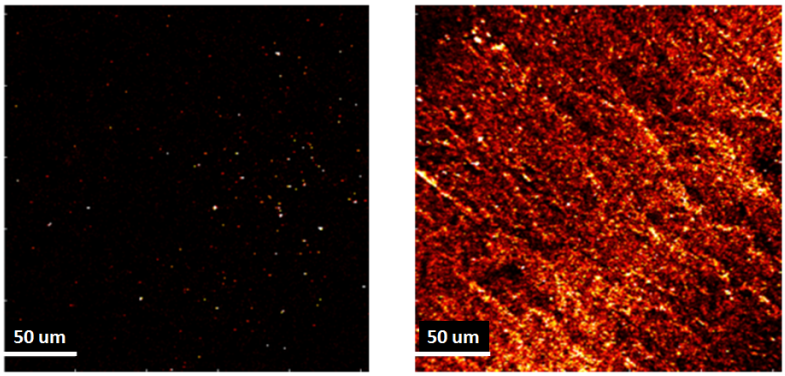

Figure 4.16: *Irradiation of nanorods in CW laser mode (left) and 80 MHz-pulse laser configuration (right).*

4.10 TPL emission spectra

TPL spectra were obtained by using a solution of gold nanorods at different excitation wavelengths (see Fig.4.17), variable in the range 730-920 nm with P_{exc} ≈2 mW, measured on the focal plane[3]. In figure 4.17 the emission spectra of the different sample synthesized with CTAB (image D) and LSB surfactant are reported (A,B,C).

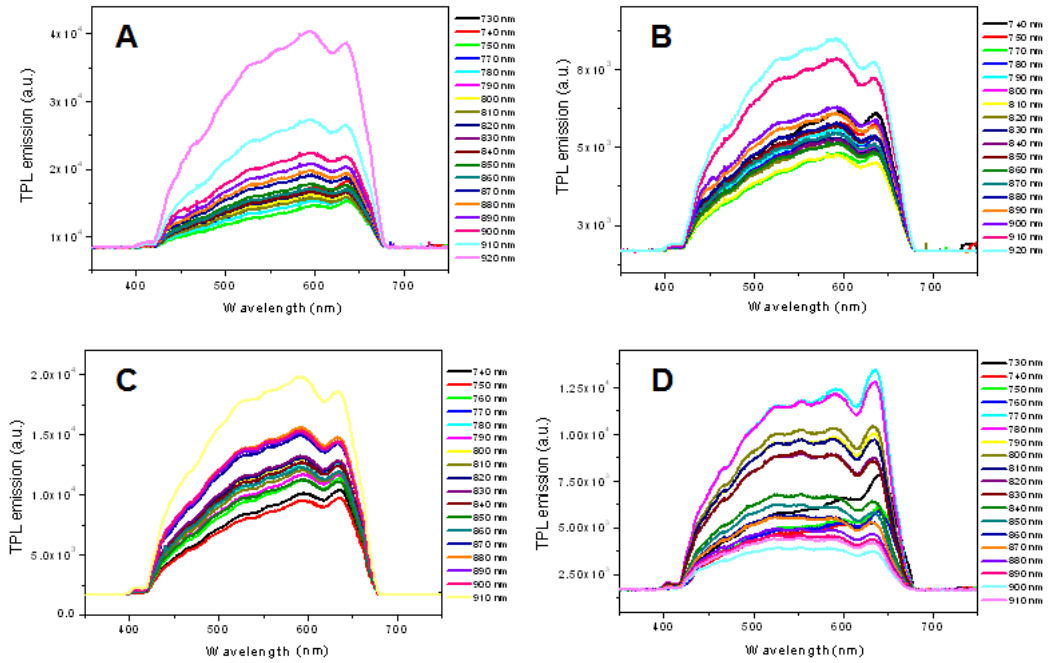

Figure 4.17: *Emission spectra of NPs synthesized with 0.35M LSB (A), 0.45M LSB (B), 0.5M LSB (C), 0.2M CTAB (D). The excitation wavelength are indicated in the panels.*

The emission spectra is a broad band [40][17] in the visible region (400-650 nm) [40]; the cut-off at 670 nm is due to the presence of a dichroic filter in the optical path which avoid the incident radiation reaching the CCD.

The emission spectrum includes the 6s-5d (L) transition (electron-hole recombination near L point of the Brillouin zone) and 6s-5d (X) transition (recombination near X point of the Brillouin zone), which occurs for bulk gold at 518 and 654 nm, respectively [40][17]. The peak positions in the TPL spectra are independent on the excitation energy and on LSB concentration (and the NP aspect ratio as consequence).

[3]the excitation power was corrected for the setup transmission in order to obtain the same power at the focal plane at variable wavelengths

4.11 TPL excitation spectra

The overall TPL intensity correlated strongly with excitation wavelength and reached a maximum at plasmon resonance, indicating a plasmon-enhanced two-photon absorption cross section [40].
In order to reconstruct the excitation spectra and to determine the relation between the TPL and the surface plasmon resonance (SPR), the area subtanded under the emission TPL spectra was calculated for each excitation wavelenght λ_{exc} and the values were reported as a function of λ_{exc}, as shown in figure 4.18. We find (figure 4.19) that the excitation spectrum (open squares) overlaps well with the longitudinal plasmon band, indicating that the TPL intensity is governed by the local field enhancement from the plasmon resonance [40].

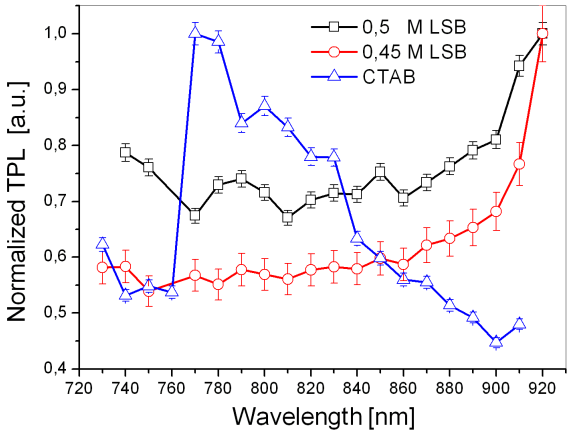

Figure 4.18: *Two-photon excitation spectra for the samples synthesized with 0.45M (red) and 0.5M LSB (black) and 0.2M CTAB (blue). The excitation power was corrected for the setup transmission.*

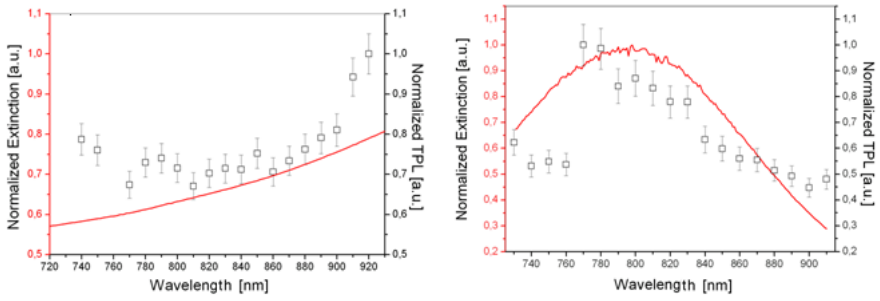

Figure 4.19: *Superposition of extinction and excitation spectra for samples obtained with 0.45 M LSB (left) and 0.2 M CTAB (right).*

4.12 Dependence of TPL on the Polarization of the exciting field light beam

The TPL intensity of the nanorods was examined as a function of polarization angle θ between the incident laser beam polarization and the NPs principal axis for the samples synthesized with 0.3, 0.4 M LSB and 0.2 M CTAB.
A drop of nanoparticles solution was dispersed and immobilized onto glass cover slips such that isolated particles could be irradiated by fs-pulsed excitation at their longitudinal plasmon resonance wavelength with an average excitation power of 1 mW on the sample. In the optical path of the experiment, described in section 4.3.2, an half-wave plate was inserted in order to rotate the polarization of the incident radiation on the whole 360° range. The TPL image was obtained by averaging 3 images collected through a 535/50 nm pass band filter and no analyzer was used. The evaluation of the TPL signal of the NPs was accomplished by computing the average signal on different regions of interest (ROIs) on the images, taken around single bright spots ascribed to isolated particles, as judged from the emission level of the single spot respect to the distribution of levels computed on a full frame. The signal corresponding to each particle was then plotted as a function of θ.

We assume that TPL is maximized when the incident field, tuned at the plasmon resonance, has its polarization parallel to the long axis of nanorod or the principal axis of a branched nanostar [17][41].

Two typical results are shown in Fig. 4.20 and 4.21; in both cases, the data can be fitted to a $\cos^4$ function [40].

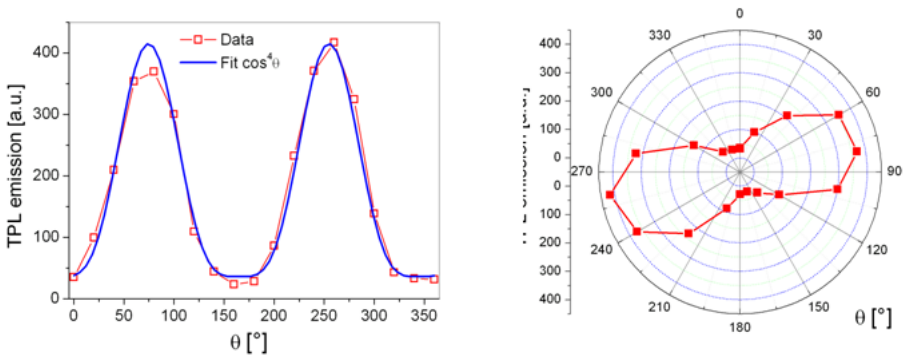

Figure 4.20: *Dependence of TPL emission on incident polarization for NPs synthesized with 0.40M LSB.*

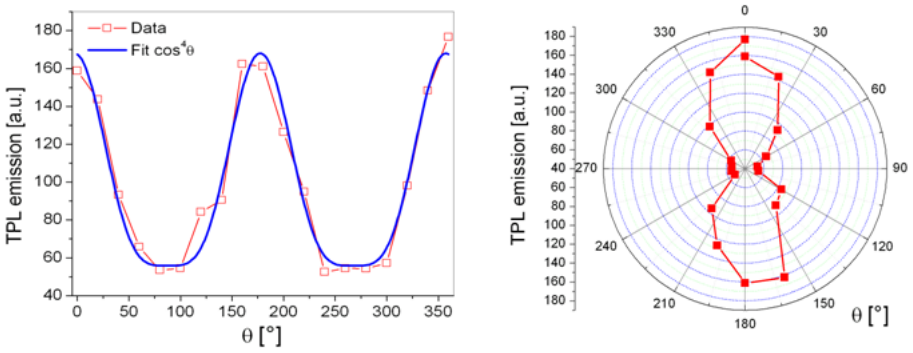

Figure 4.21: *Dependence of TPL emission on incident polarization for NPs synthesized with 0.2M CTAB.*

The polarization anisotropy ν defined as [20]:

$$\nu = \frac{I_{max} - I_{min}}{I_{max} + I_{min}} \tag{4.21}$$

is a good measure of the sensitivity to the polarization vector where I_{max} and I_{min} are the TPL intensity for the polarization excitation oriented along the longitudinal and transverse axis, respectively.

For every spot[4] of each separated sample the ν parameters were calculated and their frequency count histograms are shown in figure 4.22. From a gaussian fit of the histograms it was possible to obtain the results reported hereafter:

- ν=0.70±0.15 for sample obtained with an LSB concentration of 0.3 M
- ν=0.9±0.1 for 0.4 M LSB
- ν=0.9±0.1 for 0.2 M CTAB

The anisotropy parameter increases with the increasing of the LSB concentration and therefore with the aspect ratio (and the anisotropy) of the nanoparticles synthesized. The polarization anisotropy can then be used as simple method to obtain a rough evaluation of nanoparticles anisotropy.
Having characterized the NPs from structural an spectroscopic point of views, we now pass to analyze their application in the biomedical research.

[4]ascribed to isolated particles, as judged from the emission level of the single spot respect to the distribution of levels computed on a full frame.

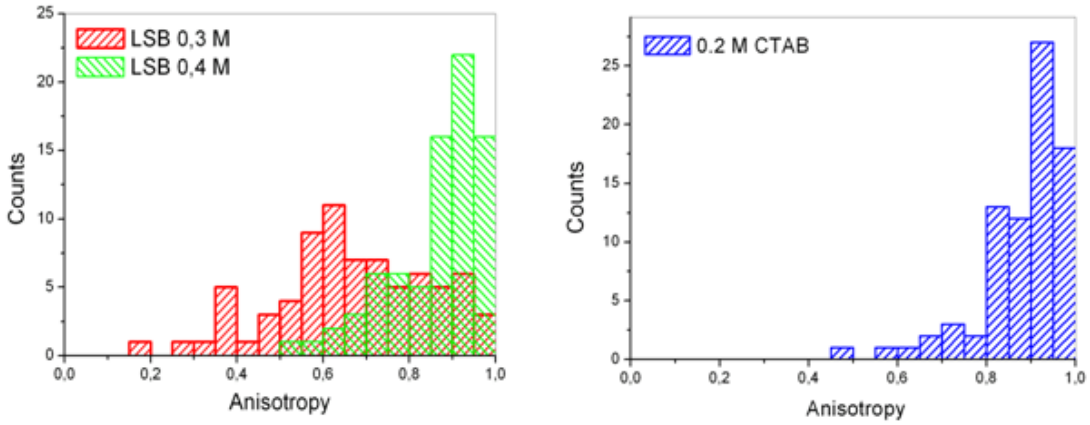

Figure 4.22: *Histograms of the anisotropy distribution for NPs obtained with 0.3 and 0.4 M LSB (Left) and 0.2 M CTAB (Right). The anistropy increases with the increasing of LSB concentration.*

4.13 Imaging applications

Cellular uptake of gold nanoparticles is a relevant issue in this field [42][43][44][45] that should be explored when considering their use in diagnostic and therapeutic applications [5][12]. Additional issues involve cytotoxicity and will be treated later in this chapter.

4.13.1 Citotoxicity

The toxicity of the NPs was tested in order to verify their potential application in in-vivo cell imaging [46][47][48][49]. The cells viability was tested after the treatment for 24h with an increasing concentration of the NPs, as shown in figures 4.23, 4.24 and 4.25 for NPs obtained with 0.2 M CTAB-PEG 2000, 0.35 M LSB and 0.5 M LSB, respectively. The histograms show the percentage of cells in vitality conditions in dependence of an increasing concentration of gold NPs. The concentration of the NP suspension was obtained by FCS using $V=(4/3)\pi R_h^3$ and $\rho_{Au} \cong 19.3$ g/cm^3 (see also section 4.8).
Samples were rinsed three times with MilliQ; no aggregation effect was present (measured by DLS; data not shown).
From these data we can infer that the nanoparticles synthesized with 0.2 M CTAB and functionalized with PEG polymer are not toxic for the cells also at high concentration (figure 4.23) [50][12][51]. Otherwise the number of dead cells increase rising the concentration of the NPs obtained with LSB surfactant; in particular at concentration used in the experiments reported above the 80% of the cells are in vitality conditions for NPs obtained with 0.35 M LSB (figure 4.24), and this percentage lower to ≈70% for NPs synthesized with 0.5 M LSB (figure 4.25). The toxicity is probably due to the LSB sur-

factant: in fact also after 3 centrifugation and resuspension in Milli-Q water cycles, a tiny amount is present in the solution which may be the origin of the cells death. In order to reduce the toxicity, it is necessary to shield the surfactant with PEG or polyelectrolyte layers (Viability≅95%, figure 4.23).

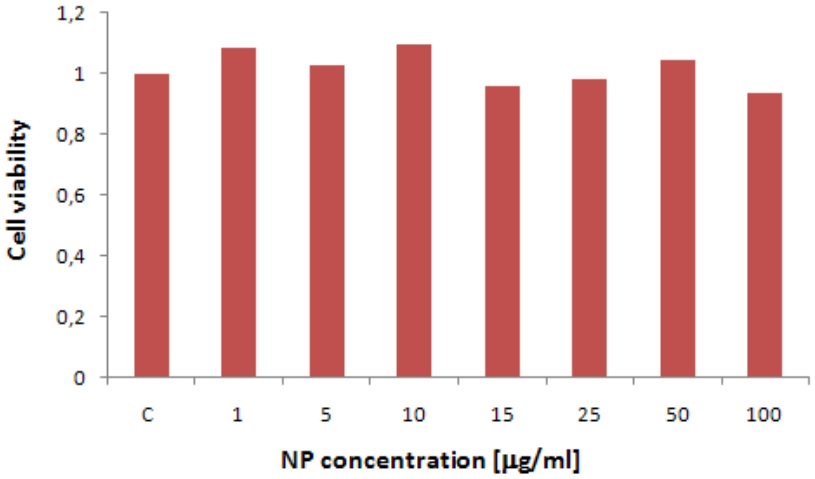

Figure 4.23: *Cell viability as a function of increasing NPs concentration. NPs were obtained with 0.2 M CTAB functionalized with PEG2000; C is the control case in which no NPs were added to cells.*

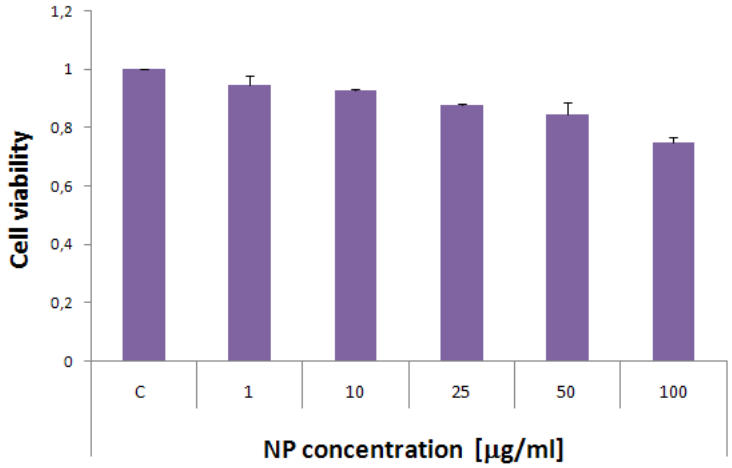

Figure 4.24: *Cell viability as a function of increasing NPs concentration. NPs were obtained with 0.35 M LSB; C is the control case in which no NPs were added to cells.*

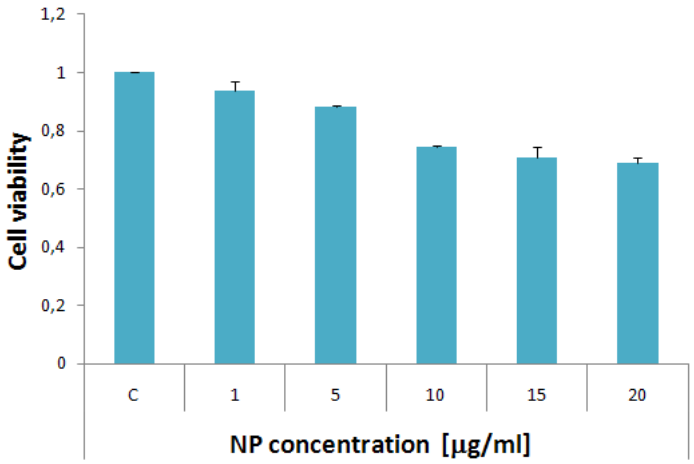

Figure 4.25: *Cell viability as a function of increasing NPs concentration. NPs were obtained with 0.5 M LSB; C is the control case in which no NPs were added to cells.*

4.14 Cellular uptake

Their strong TPL signal, resistance to photobleaching, chemical stability, ease of synthesis, simplicity of conjugation chemistry, and biocompatibility make gold anisotropic NPs an attractive contrast agent for two-photon imaging of cells [22][7][8][49].

We have therefore investigated the ability of the NPs to permeate cell membranes, by measuring the cellular uptake from HEK-293 cells and mice macrophages in tissue plated cells. We used HEK cells because they are easy to grow and representative of epithelial cells; macrophages can instead be used to study the effect of gold NPs on the immune system, in fact they act in both non-specific defense (innate immunity) as well as to help initiate specific defense mechanisms (adaptive immunity) [52]. In particular the uptake of four different samples was analized, as shown in the table:

Number	Sample
1	NPs synthesized with 0.5 M LSB
2	NPs synthesized with 0.35 M LSB
3	NPs synthesized with 0.2 M CTAB
4	NPs synthesized with 0.2 M CTAB and functionalized with the polymer PEG-2000

Images have been recorded 30 min after the addition of the NPs by exploiting two photon excitation at 800 nm. The TPL emission was detected in a wide spectral range

[40], through 485/30, 535/50 and 600/40 band pass filters. Images shown in the following panels are the result of 5 kalman average scans with 10 μs of residence time per pixel. The absence of relevant bleeding through of autofluorescence has been verified on non stained cells by measuring the fluorescence emission with and without the band pass filter used to select the TPL emission of the NPs. Measurements performed under the same laser power in the absence of NPs showed that cells autofluorescence was negligible both for HEK and macrophages cells. Figure 4.26 shows that autofluorescence of macrophages (left) and HEK cells (right) with an excitation power P_{exc}=50 mW is negligible; otherwise with P_{exc}=150 mW a strong autofluorescence signal is measured through the 485/30, 535/50 and 600/40 nm band pass filters (see figure 4.27).

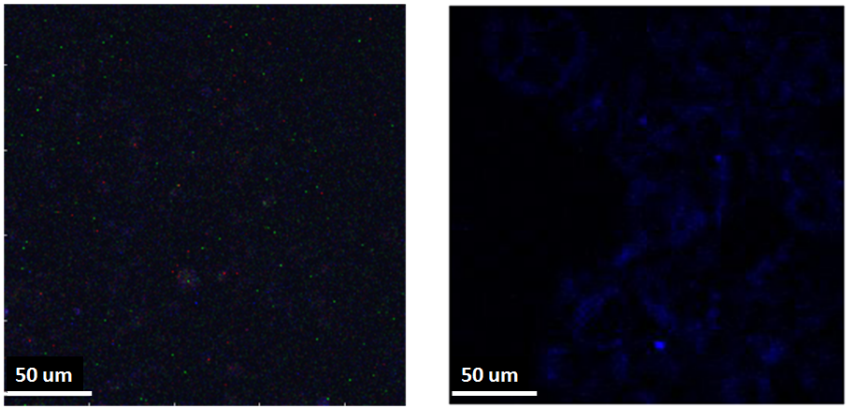

Figure 4.26: *Autofluorescence of macrophages (left) and HEK cells (right) with λ=800 nm and P_{exc}=50 mW. No emission filter was present.*

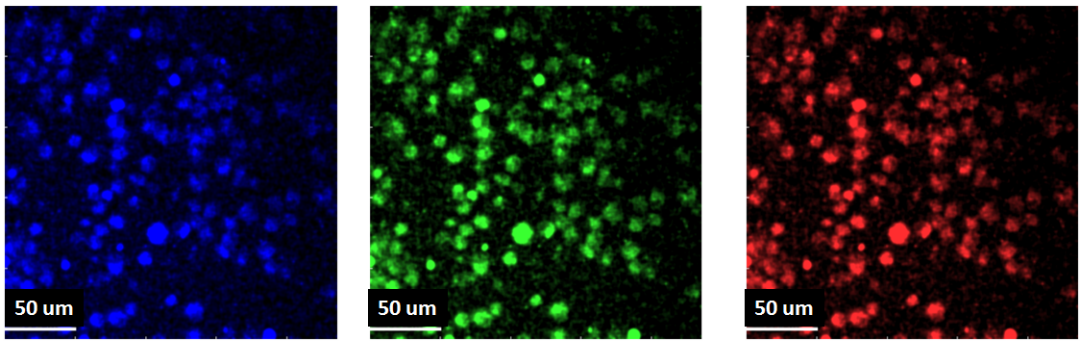

Figure 4.27: *Autofluorescence signal of macrophages cells selected through 485/30, 535/50 and 600/40 nm band pass filters, from left to right, with P_{exc}=150 mW*

By restricting P<50 mW we can then visualize (figure 4.28) the internalization in HEK cells of NPs obtained with 0.5 M LSB at concentration C=10μg/ml. In figures 4.29, 4.30 and 4.31 the TPL signal of samples 2 (C=40 μg/ml, P_{exc}=20 mW), 3 (C=100 μg/ml, P_{exc}=15 mW) and 4 (C=100 μg/ml, P_{exc}=15 mW) is reported: the three images refer to the emission through 485/30, 535/50 and 600/40 nm band pass filters; intense luminescence was observed, indicating that NPs penetrates the cell membrane of HEK cells staining the cytoplasm but not the nucleus, with an excitation power lower than the that needed to excite autofluorescence emission. In general, gold nanoparticles, including rods, enter cells by a non-specific process of endocytosis and concentrate in endosomes.

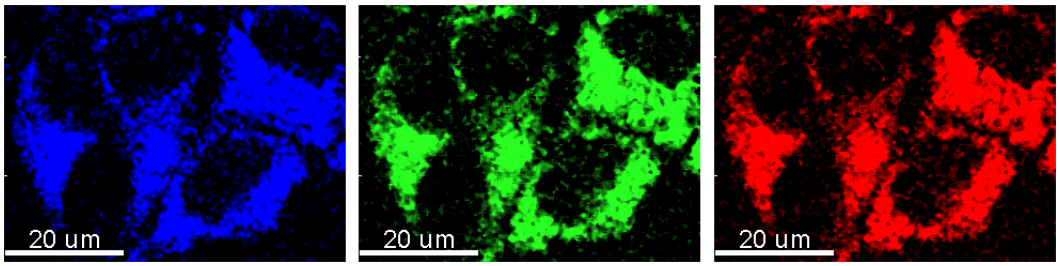

Figure 4.28: *NPs obtained with 0.5 M LSB with C=10 μg/ml internalized in HEK cells. The three images refer (from left to right) to the NPs emission selected through 485/30, 535/50 and 600/40 nm band pass filters with P_{exc}=40 mW. Only cytoplasm seems to be stained by the NPs.*

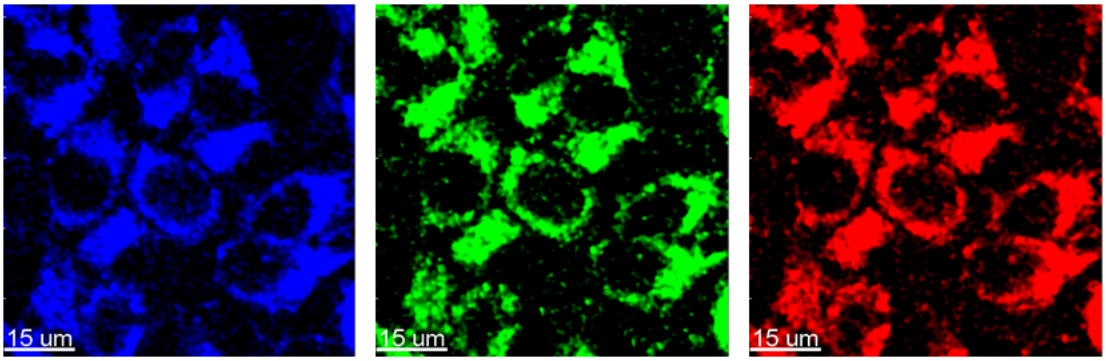

Figure 4.29: *NPs obtained with 0.35 M LSB with C=40 μg/ml internalized in HEK cells. The three images refer (from left to right) to the NPs emission selected through 485/30, 535/50 and 600/40 nm band pass filters with P_{exc}=20 mW. Only cytoplasm seems to be stained by the NPs.*

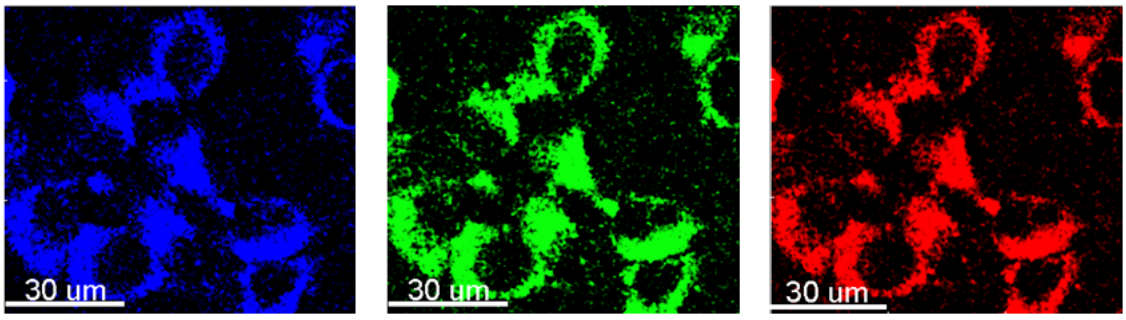

Figure 4.30: *NPs, obtained with 0.2 M CTAB, with C=100 µg/ml internalized in HEK cells. The three images refer (from left to right) to the NPs emission selected through 485/30, 535/50 and 600/40 nm band pass filters with P_{exc}=15 mW. Only cytoplasm seems to be stained by the NPs.*

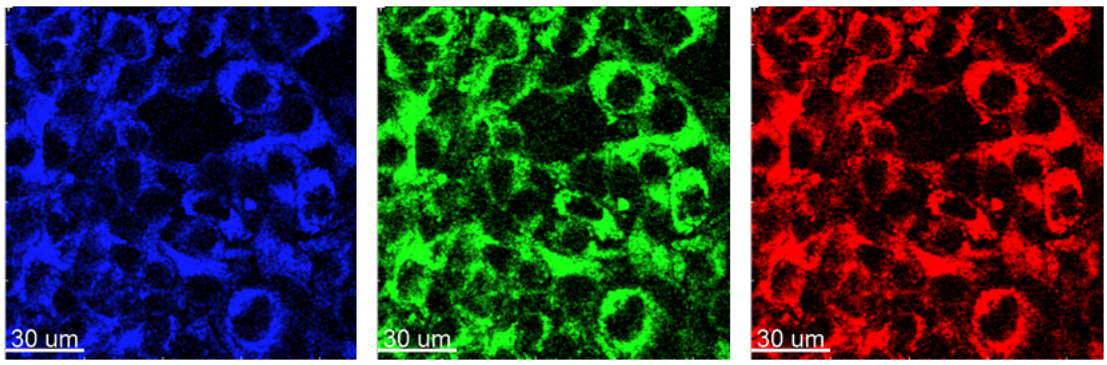

Figure 4.31: *NPs, obtained with 0.2 M CTAB and functionalized with PEG-2000, with C=100 µg/ml internalized in HEK cells. The three images refer (from left to right) to the NPs emission selected through 485/30, 535/50 and 600/40 nm band pass filters with P_{exc}=15 mW. Only cytoplasm seems to be stained by the NPs.*

HEK cells are representative of epithelial cells. We have also investigated cells of the immuno response, since NPs tipically switch on immunoreaction [53][54].

An early study of the interaction of NPs and cells of the immune system, such as macrophages, was then accomplished. Not only do macrophage-based misfunctions play a central role in auto-immune diseases such as artherosclerosis, diabetes or rheumatoid arthritis, but these cells are also frequently the host for parasitic organisms such as Toxoplasma gondii, Mycobacterium tuberculosis and Listeria monocytogenes [55][45][56]. Therefore the concept of designing nanoparticle vehicles that will attach to and/or be selectively ingested by macrophages appears to hold considerable potential.
Figures 4.32 and 4.33 show that macrophages internalize NPs obtained with 0.2 M CTAB (C=100 μg/ml) and 0.35 M LSB (C=40 mug/ml) respectively; the NPs are distributed in cytoplasmatic vesicles but not in the nuclei and are visible with the excitation power $P_{exc} \approx 15$ mW. In order to demonstrate this fact, the nuclei were stained with the DAPI dye: in figure 4.33 the nuclei are shown in blue (DAPI emission was selected through the band-pass filter 485/30 nm) and the emission of NPs in red (band-pass filter 600/40 nm).

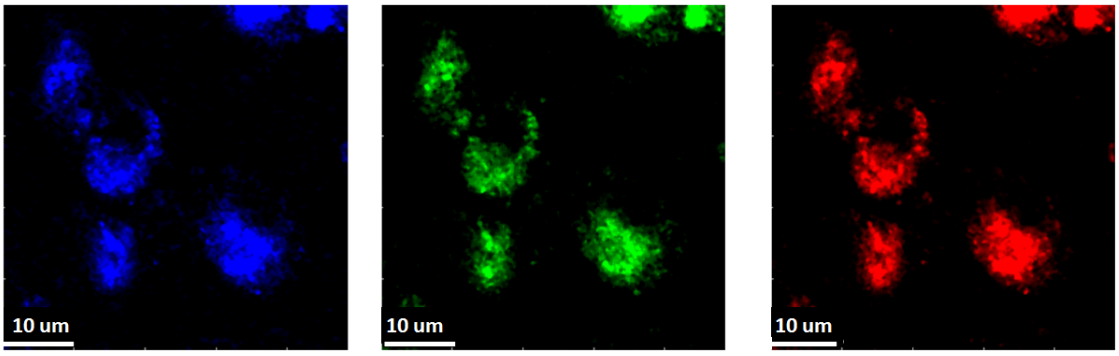

Figure 4.32: *NPs obtained with 0.2 M CTAB with C=100 μg/ml internalized in macrophages cells. The three images refer to the NPs emission selected through 485/30, 535/50 and 600/40 nm band pass filters with P_{exc}=15 mW ; NPs are internalized in cytoplasmatic vesicles.*

Instead, macrophages cells don't internalize the PEGylated nanorods (figure 4.34), in fact coating the particle with thiolated polyethylene glycol (PEG) renders it invisible to the immune system ; PEGylation is known to reduce interaction of particles with cells due to the formation of a hydrophilic stealth coating around the particles leading to reduced uptake [55][57][58].

The cells, stained with sample 4, are visible only with $P_{exc} \approx$100 mW, which is the power that produces the autofluorescence signal. No NP signal was detected even of this power.

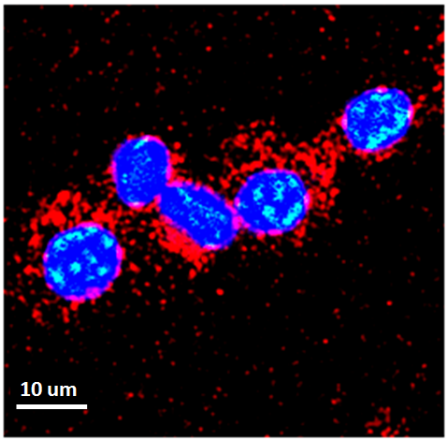

Figure 4.33: *NPs obtained with 0.35 M LSB with C=40 µg/ml internalized in macrophages cells. The nuclei, stained with the DAPI dye and are shown in blue (DAPI emission was selected through the band-pass filter 485/30 nm) and the emission of NPs in red (band-pass filter 600/40 nm). P_{exc}=15 mW*

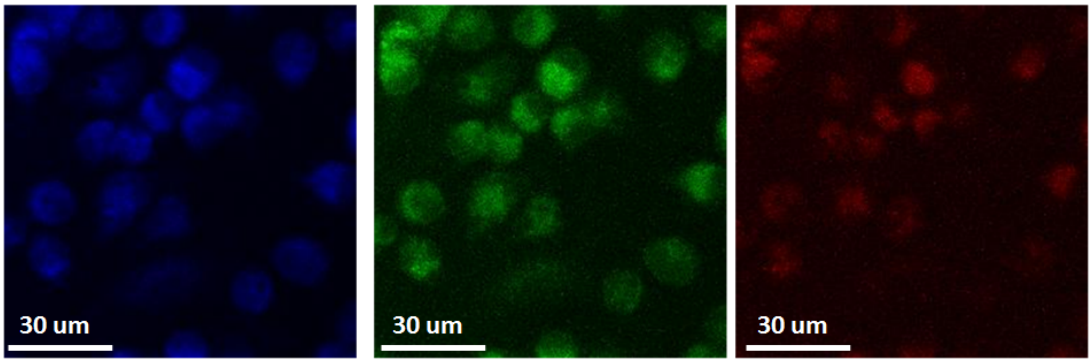

Figure 4.34: *Autofluorescence signal from macrophages cells incubated with pegylated NPs. P_{exc}=100 mW*

These preliminary results indicate that NPs are viable as a staining agent for cell imaging, although more detailed experiments are needed in order to establish the kinetics and mechanism of the process, the influence of the kind of cells used, concentration of gold nanoparticles on cellular uptake, adsorption of proteins and toxicity. The positive outcome of the investigation reported here and in the following paragraph is that they can serve as multifunctional imaging and therapeutic agents for specific targeted cells.

Moreover, in order to verify the possibility to detect gold NPs also in explanted organs, a concentration of C=1 mg/ml was inhaled by mice [5], the lungs were extracted, dissected and fixed on a coverslip.
Figure 4.35 shows the autofluorescence signal of alveolar tissue selected with the band-pass filters 485/30, 535/50 and 600/40 nm with P_{exc}=20 mW: it is negligible in the green range of emission spectrum. In figures 4.36 and 4.37 the emission of the NPs is broadband and can be seen through the 3 band-pass filters with an emission signal higher than the autofluorescence, especially in the green channel; in the superposition of the three images the NPs are shown in white.

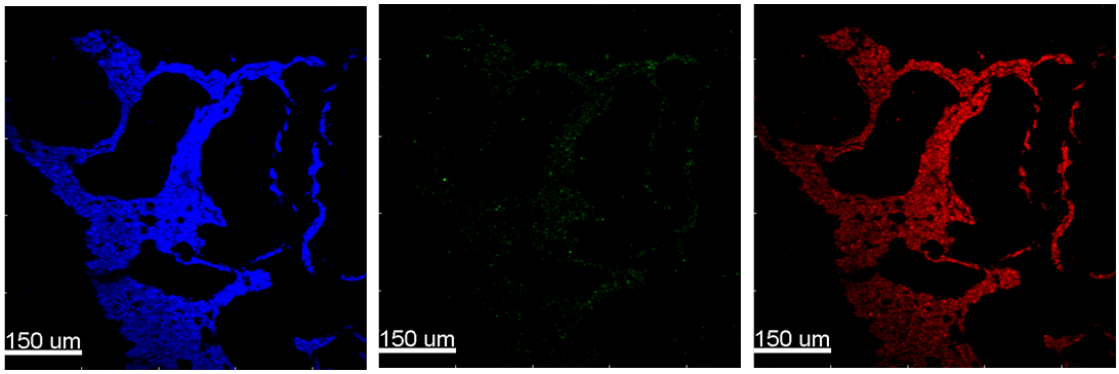

Figure 4.35: *Autofluorescence signal of alveolar tissue through 485/30, 535/50 and 600/40 nm (from left to right) band pass filters with P_{exc}=20 mW*

[5] in collaboration with Dr. P.Mantecca, Dr. G.Soncini and Dr.Maurizio Gualtieri, Environmental Sciences and Technologies Department (Polaris Project), University of Milano-Bicocca, Milano

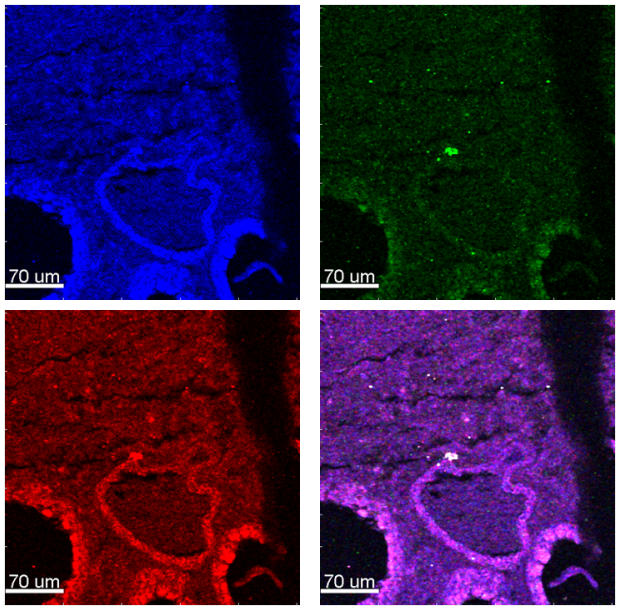

Figure 4.36: *Signal due to autofluorescence of alveolar tissue and NPs luminescence through 485/30 (up, left), 535/50 (up, right) and 600/40 nm (bottom, left). In the superposition of the three channel (bottom, right) the NPs luminescence is shown in white.*

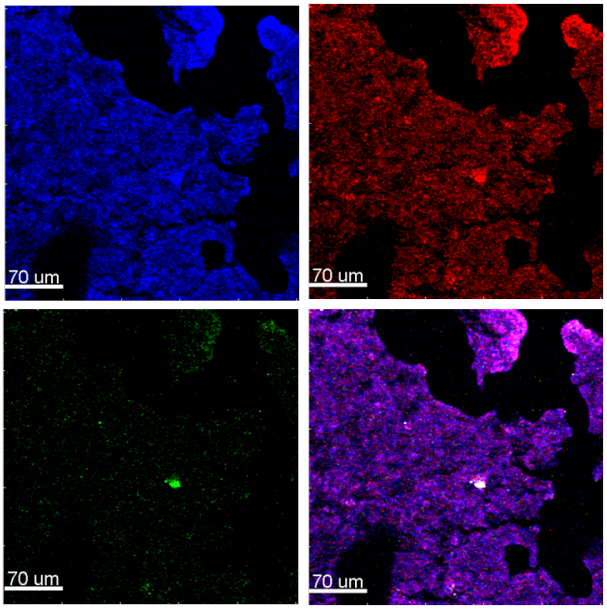

Figure 4.37: *Signal due to autofluorescence of alveolar tissue and NPs luminescence through 485/30 (up, left), 535/50 (up, right) and 600/40 nm (bottom, left). In the superposition of the three channel (bottom, right) the NPs luminescence is shown in white.*

4.15 Photothermal effects of gold NRs

The appeal of gold NRs as contrast agents for imaging is amplified by their additional capability to serve as photothermal agents, with as high as 96% of the absorbed photons converted into heat by nonradiative processes [3]. The in vitro photothermal effects of NRs have been reported by a number of groups on cultured tumor cells [5][11][59], as well on parasitic protozoans [60], macrophage [55] and bacterial pathogens [61][62]. The potential of using NRs for in vivo photothermal therapy has recently been demonstrated by Dickerson et al. who exploited the enhanced permeation and retention effect for the accumulation of PEG-NRs in tumor xenografts in mice [63]. Gold NRs exhibit a high photothermal conversion efficiency, with a larger absorption cross-section at NIR frequencies per unit volume than most other types of nanostructures [64]. The absorption of light energy is essentially instantaneous, and faster than the relaxation processes which mediate its release as heat. While initial photon absorption rates are on the fs timescale, the electron-phonon transition is on the order of a few ps, and heat diffusion to the surrounding media generally requires tens to hundreds of ps [65]. At low powers or photon densities, heat diffusion is efficient and the result is a measurable increase in temperature, in agreement with the widely appreciated concept of local hyperthermia. At high photon densities, the repetitive absorption of photons by gold NRs can exceed the rate of heat diffusion and lead to an extremely rapid rise in local temperature and superheating, resulting in cavitation effects. These considerations can be applied to different extents to CW and to pulsed excitations.
It is clear that in order to apply thermal phototherapy in medical field is essential to know the temperature at which the NPs interact with cells. In order to measure the local temperature's rise on the particles surface, induced by the absorption of infrared radiation, we have devised a novel sensor based on the conjugation of Rhodamine-B fluorophores with NPs and tested it on anisotropic gold nanoparticles (nanorods).
Our aim is to exploit changes of the dye excited-state lifetime induced by the temperature increasing of gold anisotropic nanoparticles due to laser irradiation, as reported in the following.

4.16 Experimental details

4.16.1 Sample preparation: Nanoparticle-Dye complexes

Gold nanorod-dye complex is based on electrostatic physisorption between negative and postive charged polyelectrolyte layers around the NPs. Since gold nanorods stabilized with CTAB show strong cytotoxicity, polyelectrolyte coating was used [66][67][68] in

order to enable in-vivo application of the sensor. Moreover multiple polyelectrolyte layers avoid a "direct" interaction between gold nanoparticles and fluorophores, which could result in the quenching of the dye fluorescence emission by resonant energy transfer [68][69].

The functionalization was performed as reported in the following; about 2 mL of as prepared NRs was centrifuged twice at 5,000 rpm for 10 min, the supernatant was discarded, and the precipitate was redispersed in 1 mL CTAB (0.2 M). Subsequently, it was added dropwise to 1 mL of the negative charged polyelectrolite PSS (2 g L^{-1}) aqueous solution. After 1 h adsorption time, it was centrifuged twice at 5,000 rpm to remove excess polyelectrolyte and dispersed in 1 mL deionized water. Finally, the PSS-coated GNRs were added dropwise to 1 mL of the positive charged polyelectrolyte PAH (2 g L^{-1}) aqueous solution. After 1 h, it was centrifuged twice at 5,000 rpm to remove excess polyelectrolyte and dispersed in 1 mL of deionized water. The procedure was iterated and a second layer of PSS was added. In order to obtain the NP-dye complex, the NPs were added dropwise to 1 mL Rhodamine-B solution ($\approx$ 5 nM). Finally, the solution was centrifuged at 5,000 rpm to remove excess unbound dye molecules. The final distance between the gold NP and the Rhodamine-B molecules is $\cong$ 1.5 nm.

Zeta potentials (ζ) were measured to follow the formation of the NPs-dye bioconjugates [6]. The ζ-potential of the coated GNRs was measured after deposition of each layer, as shown in Fig. 4.38. The ζ-potential after the adsorption of each layer is reported in table 4.11 and in figure 4.38.

Layer	**ζ potential [mV]**
PSS (first)	-36 $\pm$ 4
PAH (first)	12$\pm$ 7
PSS (second)	-26$\pm$2
Rhodamine-B	49.7$\pm$0.5

Table 4.11: *ζ-potential as a function of the number of PSS-PAH layers adsorbed to the GNRs.*

[6]Collaboration with Dr. Miriam Colombo, Nanobiotechnology Lab, Biotechnology Department, University of Milano Bicocca. Measures were taken on a Malvern Zeta sizers.

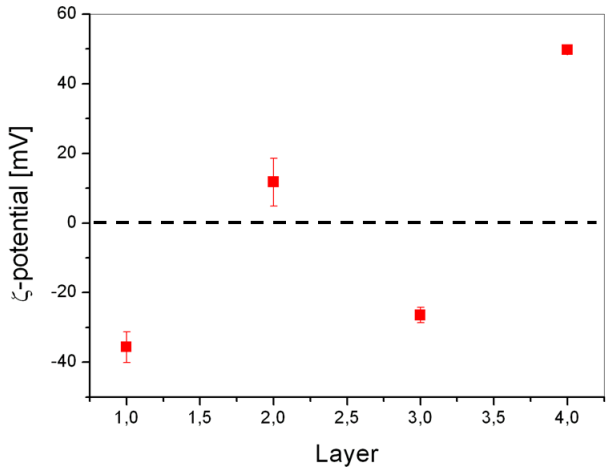

Figure 4.38: *ζ-potential after the adsorption of PSS-PAH layers.*

4.16.2 Spectral characterization

The fluorescence emission spectra of Rhodamine-B dye were acquired on a Varian Eclipse spectrofluorimeter (Varian, U.K.).

4.16.3 Fluorescence Spectroscopy

The description of the system is reported in section 3.4. The lifetime histograms were computed on the selected bursts for Np-dye complexes and on the background for free Rhodamine-B dye.
The free Rhodamine-B lifetime histograms were fitted to a single exponential function, while the NP-dye complexes fluorescence decays were fitted to double exponential functions with fractional intensities, f_1 and f_2=1-f_1, and relaxation times, τ_1 and τ_2.

4.16.4 Dye-Lifetime measurement

Lifetime measurements in frequency domain were performed by the multifrequency cross-correlation phase and modulation fluorometer K2 (ISS, Illinois).
The beam, coming from Argon ion laser, is reflected by a series of mirrors on a two way-polarizer and later directed into a Pockel cell, which is responsible for modulating the excitation light. A radio-frequencies synthesizer (Marconi 2022C) regulates the voltage - in the range of 0.6-330 MHz - given to the birefringent crystal (Potassium dihydrogen

phospate) of the Pockel cell, causing a shift between the ordinary and the extraordinary beam. A beam splitter divides the output beam from Pockel cell in two parts: a beam is detected by a photomultiplier tube (PMT) and represents the reference signal for excitation phase and modulation measurements; the other reaches the thermostatting sample compartment, a two cuvettes rotating chamber, computer controlled, for the sample and for a reference dye necessary in lifetime measurements. Light from sample and reference, selected by a pass band filter in order to eliminate Rayleigh and Raman scattering, is orthogonally detected by a second PMT powered by 3W amplifier (Model 525LA, EN). PMT (R928 Hamamatsu) voltage is manually controlled, with the maximum gain of 900V. Moreover, the PMT is coupled with a second frequencies synthesizer, which generates frequencies synchronized with Pockel cell synthesizer but different by 80 Hz in order to perform the Cross Correlation Detection. A dedicated board processes the signal from PMT and allows to change amplifier gain depending on sample signal intensity. The data analysis is performed by a proper software (Vinci Analysis) that includes lifetime calculations, analysis of the fluorescence anisotropy and phase and modulation resolved spectra.

4.17 Results

4.17.1 Rhodamine-B characterization

Fluorescence emission measurement

The dependence of the Rhodamine-B emission spectra in solution was first measured while increasing the temperature from 10 to 60 °C. As shown in figure 4.39A and in table 4.12 the peak emission intensity decreases when increasing the temperature.

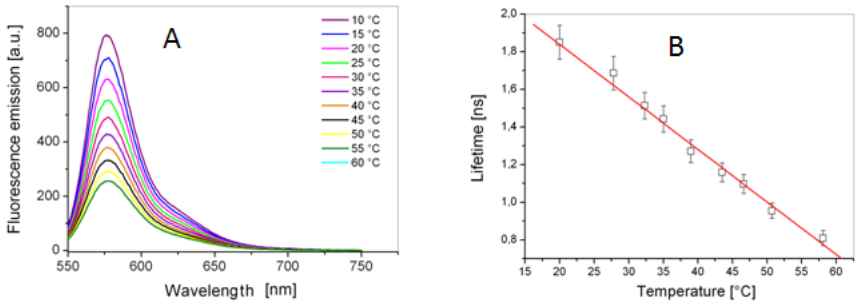

Figure 4.39: *A: Rhodamine-B emission spectra while increasing the temperature. B: peak emission intensity vs. temperature. The linear fit is described by the relation* $\langle\tau\rangle$*=[2.4-0.029T(° C)] ns*

Temperature [°C]	**Emission intensity [a.u.]**
10	882±8
15	794±8
20	704±7
25	631±6
30	552±7
35	487±8
40	429±7
45	379±7
50	331±6
55	291±6
60	255±6

Table 4.12: *Dependence of Rhodamine-B emission intensity on temperature.*

The quantum yield is defined as [70]:

$$\phi = \frac{k_R}{k_R + k_{NR}} \tag{4.22}$$

where k_R and k_{NR} are the rate of radiative and non-radiative decay of Rhodamine-B, respectively. It can be assumed that the decrease in the Rhoamine-B fluorescence emission (and as consequence of ϕ) of the fluorophore is due to the increasing of k_{NR}, i.e. the number of non-radiative de-excitation, as k_R is typically not affected when no resonant energy transfer is present.

4.17.2 Lifetime measurement

We characterized the fluorescence response of Rhodamine-B in solution at increasing temperature, also in terms of its excited-state lifetime τ. The results are reported in table 4.13.
As shown in table 4.13 and in figure 4.40, also the excited state lifetime decreases when increasing the temperature. Since τ is [70]:

$$\tau = 1/K = \frac{1}{k_R + k_{NR}} \tag{4.23}$$

in agreement with the emission, we can infer from the data that k_{NR} increases with T, leading to the excited-state lifetime decrease.

Temperature [°C]	**Lifetime [ns]**
20	1.85±0.09
27.8	1.68±0.08
32.3	1.51±0.07
35	1.44±0.07
39	1.27±0.06
43.5	1.15±0.05
46.6	1.09±0.05
50.7	0.95±0.04
58	0.80±0.04

Table 4.13: *Dependence of Rhodamine-B excited state lifetime on temperature.*

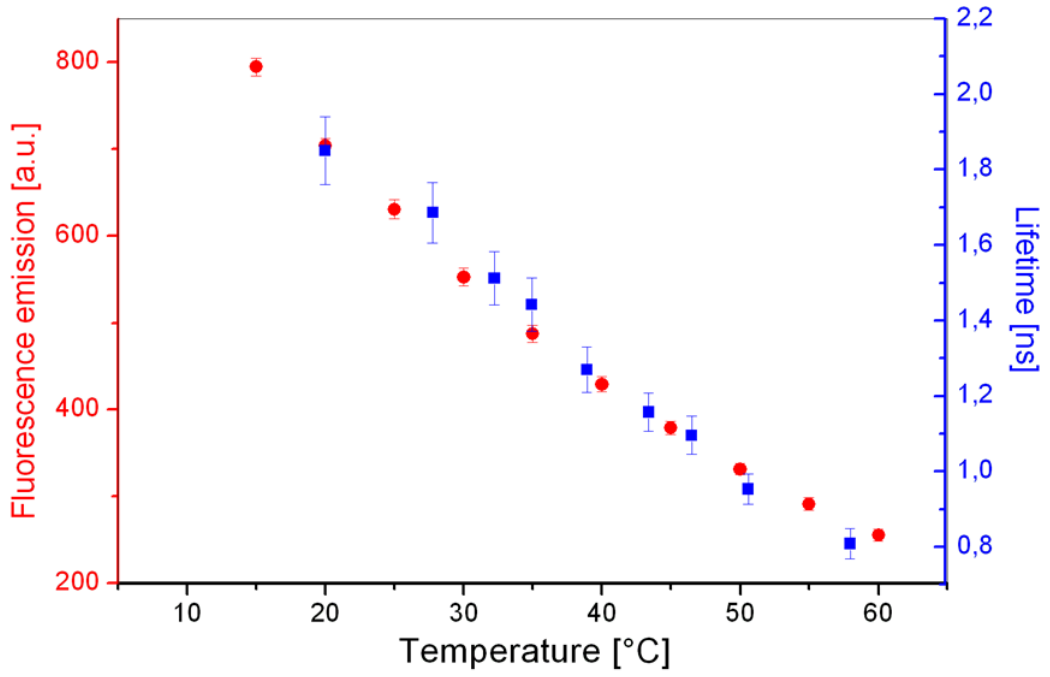

Figure 4.40: *Emission intensity (red) and excited-state lifetime (blue) of Rhodamine-B dye decrease as a function of the temperature*

In figure 4.40 the fluorescence intensity and lifetime of Rhodamine-B as a function of T are reported. The trend observed is very similar confirming our hypothesis that k_R stays ≈ constant with T.

As shown in figure 4.39B data are well approximated by a linear fit, described by the following relation:

$$\langle\tau\rangle = [(2.4 \pm 0.3) - (0.029 \pm 0.005)T(^{\circ}C)]ns \tag{4.24}$$

which enables to evaluate the temperature increase T from the dye excited state lifetime $\langle\tau\rangle$.

These results show that Rhodamine-B is a good sensor of the temperature in the range 10-60 °C. We can then conjugate it with gold NPs in order to create a novel assay for the online monitoring of the local temperature on GNRs to be used for photothermal therapy.

4.18 Assay characterization

A solution with a concentration ≈300 pM of gold nanorods-fluorophores complexes was irradiated with an infrared laser with power ranging from 2 mW to 25 mW and the wavelength set at the surface plasmon resonance λ=λ_{SPR}= 800 nm which excites both the T sensitive dye and the NPs (with the consequent fluorescence and TPL emission), and heats the NPs.
The time fluorescence traces of the assays show several fluorescence burst which are ascribed to the transit of the complexes through the excitation volume (figure 4.41red), while the Rhodamine-B traces are relatively uniform (figure 4.41black).

The lifetime histograms were computed on the selected bursts and the fluorescence decays were fitted to double exponential functions with fractional intensities, f_1 and f_2=1-f_1, and relaxation times, τ_1 and τ_2. From this analysis the average lifetime was also computed as:

$$\langle\tau\rangle = f_1\tau_1 + f_2\tau_2 \tag{4.25}$$

with

$$f_i = \frac{\alpha_i\tau_i}{\sum_i \alpha_i\tau_i} \tag{4.26}$$

where α_i are the pre-exponential factors of the i-th component with lifetime τ_i. τ_1 ≤400 ps was ascribed to the NPs lifetime, while τ_2 ≈1-3 ns is due to the Rhodamine-B dye lifetime. We have preferred to account for both τ_1 and τ_1 by computing $< \tau >$,

although the fractional intensity $f_1 \cong 0.15 << f_2$, since the double exponential fit would increase the uncertainty on the best fit value.

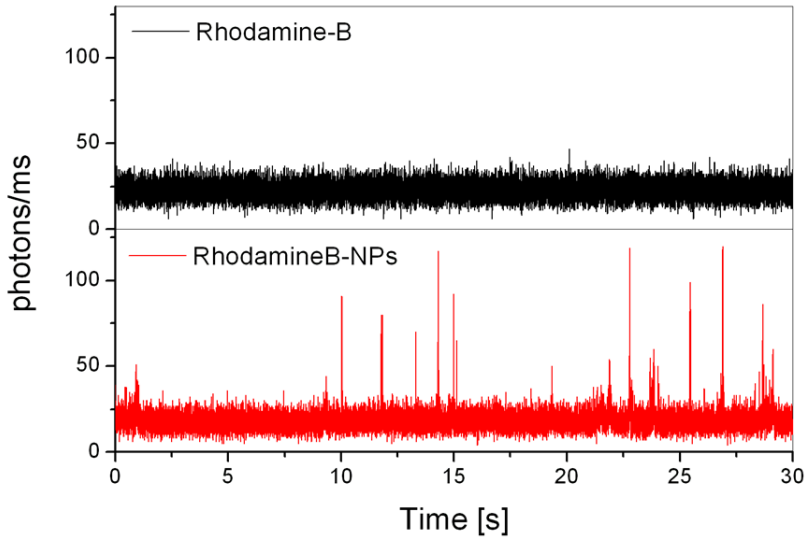

Figure 4.41: *Fluorescence traces of the Rhodamine-B (upper trace, black) and RhodamineB-NPs assay (lower trace, red).*

$< \tau >$ decreases while rising the laser power and presumably the NPs surface temperature, as shown in figure 4.42 and in table 4.14. Otherwise the lifetime of the free Rhodamine-B, $< \tau >_{Rh-B}$ (table 4.14), remains constant while increasing the power[7]. The histograms of $< \tau >$ distribution are also reported in figures 4.43.

P [mW]	$< \tau >$ **[ns]**	$< \tau >_{Rh-B}$ **[ns]**
2	1.74±0.2	1.80±0.12
4	1.66±0.2	1.79±0.12
8	1.52±0.16	1.80±0.11
15	1.35±0.07	1.79±0.13
20	1.25±0.1	1.80±0.12
25	1.0±0.1	1.80±0.11

Table 4.14: *The table shows the $< \tau >$ values of the NPs-Rhodamine B assay and the free Rhodamine B obtained rising the laser power.*

[7]The power was measured after the objective, near the focal plane.

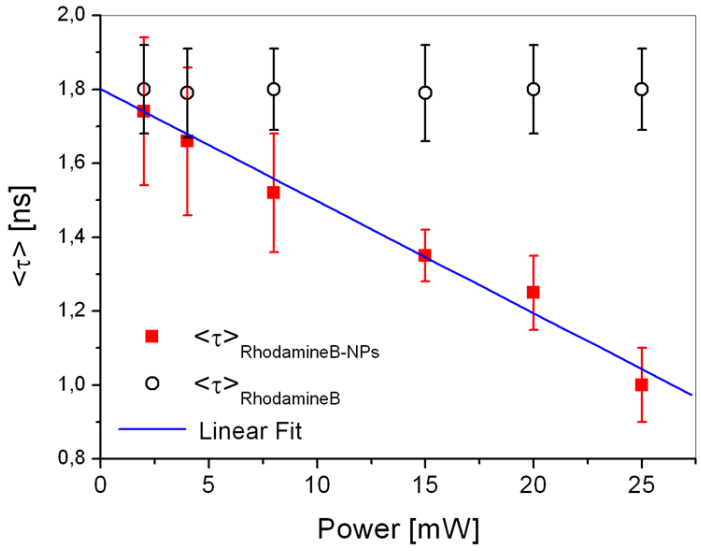

Figure 4.42: *Dependence of mean excited-state lifetime of the assay (red) and the free Rhodamine-B (black) on the incident power.*

If we assume that the decrease of $< \tau >$ is due to a T increase on the surface we can infer the local temperature by writing equation 4.24 in the form:

$$T = \frac{2.4 - \langle \tau \rangle}{0.029} {}^{\circ}C \tag{4.27}$$

This equation links the local temperature due to surface NPs heating to $< \tau >$ of the Rhodamine-B dye. Due to the fact that the temperature increase is due to more than one laser pulses[8], the T evaluation, from eq. 4.27, can be considered as a mean temperature.
In table 4.15 the temperature values corresponding to the Rhodamine-B mean lifetime (when bound to NPs in the assay) are reported as a function of the T.

Data reported in these sections show that, once the link between the dye excited state lifetime and the temperature is known, the increase in the NP local surface temperature, due to laser heating, can be deduced from the measurement of the dye τ (figure 4.44).

Moreover, the fluorescence-excited state lifetime of the free dye in solution was measured increasing the laser radiation power in the same range (2-25 mW) in order to verify that the temperatute rising was due to NPs surface heating. It was found that the Rhodamine-B lifetime τ=1.8±0.1 ns doesn't depend on the laser power in the range explored (figure 4.42black). This proves that the decrease in dye excited state lifetime is due to NP surface heating and as consequence, the assay is able to play the role of molecular thermometer to measure local tempeature.

[8]in the experiment a Titanium-Sapphire laser with 80 MHz repetition rate was used

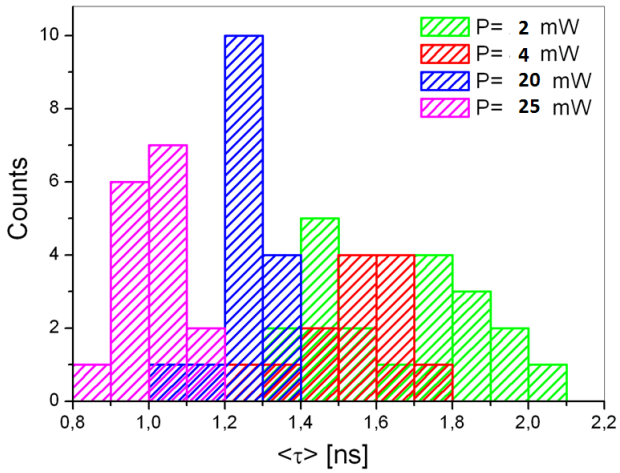

Figure 4.43: *Superposition of mean excited state lifetime histograms of the assay RhodamineB-NPs.*

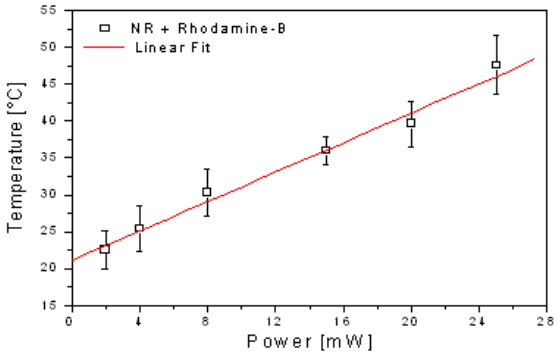

Figure 4.44: *Dependence of surface NPs temperature, measured through Rhodamine-B excited state lifetime, on incident power.*

P [mW]	$< \tau >$ **[ns]**	**T [°C]**
2	1.74±0.25	22.6±2.6
4	1.66±0.2	25.5±3.1
8	1.52±0.16	30.3±3.2
15	1.35±0.07	36.0±1.87
20	1.25±0.1	39.6±3.1
25	1.0±0.1	47.6±4

Table 4.15: *The temperature values corresponding to each Rhodamine-B mean lifetime are shown.*

4.19 Conclusion

In this chapter we reported the characterization of asymmetric branched gold nanoparticles obtained by using for the first time a zwitterionic surfactant, laurylsulphobetaine (LSB), in the seed growth method approach [9]. LSB concentration in the growth solution allows to control the dimension of the NPs and the LSPR position, that can be tuned in the 700-1100 nm Near Infrared range. The samples have been analized with several techniques to obtain a complete characterization: from the data obtained through the absorption spectra in the UV-Visible region, the TEM images of the solutions, FCS and DLS experiments, we reached information on the nanoparticles shape and dimensions. In particular, in the case of LSB surfactant three different populations have been found: nanospheres with diameter lower than 20 nm, nanostars characterized by large trapezoidal branches, and asymmetric branched nanoparticles with high aspect ratio.
The dependence of the luminescence intensity on the incident light intensity for samples realized with LSB and CTAB was studied, checking the quadratic dependence and therefore the two photon nature of the observed luminescence (TPL). By measuring the luminescence spectra for different excitation wavelengths with a spectral CCD camera, it has been possible to obtain the excitation spectra of the NPs, very similar to the extinction spectra: this result is indicative of the role played by surface plasmons in TPL. As a further characterization, the dependence of the TPL on polarization angle of the incident radiation was checked.
The use of gold anisotropic nanoparticles as bright contrast agents for two-photon luminescence (TPL) imaging of cells was also explored: NPs synthesized with both LSB and CTAB surfactant are internalized in the cytoplasm of HEK and macrophages cells; otherwise pegylated gold NPs are invisible to the immune system and none cellular uptake was detected.

Finally we have developed a novel hybrid metal-organic system, based on NPs complexed to RhB by electrostatic adsorption on multiple poly-electrolyte layers, in order to detect the local temperature around the NP induced by the laser heating. Rhodamine-B-NPs assay is able to play the role of molecular thermometer and can be tested in-vivo to evaluate the damage temperature of tumoral cells. The hybrid sensor in fact can be used for imaging and photothermal purposes at the same time: the infrared laser radiation can excite both Rhodamine-B and TPL from the gold NRs in order to visualize the internalization of the sensor in cells and the same radiation can heat the NRs, damaging the tumor cell.

[9] The synthesis was proposed and performed by the group of Prof. P.Pallavicini, at University of Pavia (General Chemistry Department)

Bibliography

[1] Murphy C.J.; Gole A.M.; Hunyadi S.E.; Stone J.W.; Sisco P.N.; Alkilany A.; Kinard B.E.; Hankins P. Chemical sensing and imaging with metallic nanorods. *Chemical Communications*, 2008(5):544–557, 2008.

[2] Perez-Juste J.; Pastoriza-Santos I.; Liz-Marzan L.M.; Mulvaney P. Gold nanorods: synthesis, characterization and applications. *Coordination Chemistry Reviews*, 249(17-18):1870–1901, 2005.

[3] Huang X.; Jain P.K.; El-Sayed I.H.; El-Sayed M.A. Gold nanoparticles: interesting optical properties and recent applications in cancer diagnostics and therapy. *Nanomedicine*, 2(5):681–693, 2007.

[4] Sokolov K.; Follen M.; Aaron J.; Pavlova I.; Malpica A.; Lotan R.; Richards-Kortum R. Real-time vital optical imaging of precancer using anti-epidermal growth factor receptor antibodies conjugated to gold nanoparticles. *Cancer Research*, 63(9):1999, 2003.

[5] El-Sayed I.H.; Huang X.; El-Sayed M.A. Surface plasmon resonance scattering and absorption of anti-EGFR antibody conjugated gold nanoparticles in cancer diagnostics: applications in oral cancer. *Nano Lett*, 5(5):829–834, 2005.

[6] Sonnichsen C. and Alivisatos A.P. Gold nanorods as novel nonbleaching plasmon-based orientation sensors for polarized single-particle microscopy. *Nano Lett*, 5(2):301–304, 2005.

[7] Durr N.J.; Holfeld B.A.; Larson T.; Smith D.K.; Korgel B.A.; Sokolova K.; Ben-Yakar A. Gold nanorods for optimized two-photon luminescence imaging of cancerous tissue. In *Proceedings of SPIE*, volume 6641, page 66410O, 2007.

[8] Link S.; El-Sayed M.A. Shape and size dependence of radiative, non-radiative and photothermal properties of gold nanocrystals. *Int. Reviews in Physical Chemistry*, 19 (3):409–453, 2000.

[9] O'Neal D.P.; Hirsch L.R.; Halas N.J.; Payne J.D.; West J.L. Photo-thermal tumor ablation in mice using near infrared-absorbing nanoparticles. *Cancer letters*, 209(2):171–176, 2004.

[10] Loo C.; Lowery A.; Halas N.; West J.; Drezek R. Immunotargeted nanoshells for integrated cancer imaging and therapy. *Nano Lett*, 5(4):709–711, 2005.

[11] Huff T.B.; Tong L.; Zhao Y.; Hansen M.N.; Cheng J.X.; Wei A. Hyperthermic effects of gold nanorods on tumor cells. *Nanomedicine*, 2(1):125–132, 2007.

[12] Tong L.; Wei Q.; Wei A.; Cheng J.X. Gold Nanorods as Contrast Agents for Biological Imaging: Optical Properties, Surface Conjugation and Photothermal Effects. *Photochemistry and photobiology*, 85(1):21–32, 2009.

[13] Petrova H.; Juste J.P.; Pastoriza-Santos I.; Hartland G.V.; Liz-Marzán L.M.; Mulvaney P. On the temperature stability of gold nanorods: comparison between thermal and ultrafast laser-induced heating. *Physical Chemistry Chemical Physics*, 8(7):814–821, 2006.

[14] Wust P.; Hildebrandt B.; Sreenivasa G.; Rau B.; Gellermann J.; Riess H.; Felix R.; Schlag PM. Hyperthermia in combined treatment of cancer. *The lancet oncology*, 3(8):487–497, 2002.

[15] Pallavicini P.; Chirico G.; Collini M.; Dacarro G.; Donà A.; D'Alfonso L.; Falqui A.; Diaz-Fernandez Y.; Freddi S.; Garofalo B.; Sironi L.; Taglietti A. Synthesis of branched Au nanoparticles with tunable near-infrared LSPR using a zwitterionic surfactant. *Chem. Commun.*, 2010.

[16] Mooradian A. Photoluminescence of metals. *Physical Review Letters*, 22(5):185–187, 1969.

[17] Boyd GT ; Yu ZH; Shen YR. Photoinduced luminescence from the noble metals and its enhancement on roughened surfaces. *Physical Review B*, 33(12):7923–7936, 1986.

[18] Demers L.M.; Mirkin C.A.; Mucic R.C.; Reynolds III R.A.; Letsinger R.L.; Elghanian R.; Viswanadham G. A fluorescence-based method for determining the surface coverage and hybridization efficiency of thiol-capped oligonucleotides bound to gold thin films and nanoparticles. *Anal. Chem*, 72(22):5535–5541, 2000.

[19] Mohamed M.B.; Volkov V.; Link S.; El-Sayed M.A. The lightning gold nanorods: fluorescence enhancement of over a million compared to the gold metal. *Chemical Physics Letters*, 317(6):517–523, 2000.

[20] Bouhelier A.; Bachelot R.; Lerondel G.; Kostcheev S.; Royer P.; Wiederrecht GP. Surface plasmon characteristics of tunable photoluminescence in single gold nanorods. *Physical review letters*, 95(26):267405, 2005.

[21] Imura K.; Nagahara T.; Okamoto H. Near-field two-photon-induced photoluminescence from single gold nanorods and imaging of plasmon modes. *J. Phys. Chem. B*, 109(27):13214–13220, 2005.

[22] Wang H.; Huff T.B.; Zweifel D.A.; He W.; Low P.S.; Wei A.; Cheng J.X. In vitro and in vivo two-photon luminescence imaging of single gold nanorods. *Proceedings of the National Academy of Sciences of the United States of America*, 102(44):15752, 2005.

[23] Wilcoxon JP; Martin JE; Parsapour F.; Wiedenman B.; Kelley DF. Photoluminescence from nanosize gold clusters. *The Journal of Chemical Physics*, 108:9137, 1998.

[24] Boyd GT; Rasing T.; Leite JRR; Shen YR. Local-field enhancement on rough surfaces of metals, semimetals, and semiconductors with the use of optical second-harmonic generation. *Physical Review B*, 30(2):519–526, 1984.

[25] Beversluis M.R.; Bouhelier A.; Novotny L. Continuum generation from single gold nanostructures through near-field mediated intraband transitions. *Physical Review B*, 68(11):115433, 2003.

[26] Okamoto H. and Imura K. Near-field imaging of optical field and plasmon wavefunctions in metal nanoparticles. *Journal of Materials Chemistry*, 16(40):3920–3928, 2006.

[27] Biagioni P.; Celebrano M.; Savoini M.; Grancini G.; Brida D.; Mátéfi-Tempfli S.; Mátéfi-Tempfli M.; Duò L.; Hecht B.; Cerullo G. et al. Dependence of the two-photon photoluminescence yield of gold nanostructures on the laser pulse duration. *Physical Review B*, 80(4):45411, 2009.

[28] Kim H.; Xiang C.; Guell A.G.; Penner R.M.; Potma E.O. Tunable two-photon excited luminescence in single gold nanowires fabricated by lithographically patterned nanowire electrodeposition. *The Journal of Physical Chemistry C*, 112(33):12721–12727, 2008.

[29] Nikoobakht B.; El-Sayed M.A. Preparation and growth mechanism of gold nanorods (NRs) using seed-mediated growth method. *Chem. Mater*, 15(10):1957–1962, 2003.

[30] Khoury C.G.; Vo-Dinh T. Gold Nanostars For Surface-Enhanced Raman Scattering: Synthesis, Characterization and Optimization. *The Journal of Physical Chemistry C*, 112(48):18849–18859, 2008.

[31] Kumar P.S.; Pastoriza-Santos I.; Rodríguez-González B.; Abajo F.; Liz-Marzán L.M. High-yield synthesis and optical response of gold nanostars. *Nanotechnology*, 19:015606, 2008.

[32] Bruce J. Berne and Robert Pecora. Dynamic Light Scattering: With Applications to Chemistry, Biology, and Physics. *Dover, N.Y. (USA)*, 1976.

[33] De La Torre J.G.; Martinez M.C.L.; Tirado M.M. Dimensions of short, rodlike macromolecules from translational and rotational diffusion coefficients. Study of the gramicidin dimer. *Biopolymers*, 23(4):611–615, 1984.

[34] Schwille P. and Haustein E. Fluorescence Correlation Spectroscopy. *Prcdement publi dans Biophysics Textbook Online (BTOL).*

[35] Magde D.; Elson E.L.; Webb W.W. Fluorescence correlation spectroscopy. II. An experimental realization. *Biopolymers*, 13(1):29–61, 1974.

[36] Ehrenberg M. and Rigler R. Rotational brownian motion and fluorescence intensify fluctuations. *Chemical Physics*, 4(3):390–401, 1974.

[37] Aragon S.R.; Pecora R. Fluorescence correlation spectroscopy and Brownian rotational diffusion. *Biopolymers*, 14(1):119–137., 1975.

[38] Kask P.; Piksarv P.; Pooga M.; Mets
"U.; Lippmaa E. Separation of the rotational contribution in fluorescence correlation experiments. *Biophysical Journal*, 55(2):213–220, 1989.

[39] Widengren J.; Mets
"U.; Rigler R. Photodynamic properties of green fluorescent proteins investigated by fluorescence correlation spectroscopy. *Chemical Physics*, 250(2):171–186, 1999.

[40] Wang D.S.; Hsu F.Y.; Lin C.W. Surface plasmon effects on two photon luminescence of gold nanorods. *Optics Express*, 17(14):11350–11359, 2009.

[41] Novotny L.; Bian R.X.; Xie X.S. Theory of nanometric optical tweezers. *Physical Review Letters*, 79(4):645–648, 1997.

[42] Chithrani B.D.; Ghazani A.A.; Chan W.C.W. Determining the size and shape dependence of gold nanoparticle uptake into mammalian cells. *Nano Lett*, 6(4):662–668, 2006.

[43] Ferrari M. Cancer nanotechnology: opportunities and challenges. *Nature Reviews Cancer*, 5(3):161–171, 2005.

[44] Gratton S.E.A.; Ropp P.A.; Pohlhaus P.D.; Luft J.C.; Madden V.J.; Napier M.E.; DeSimone J.M. The effect of particle design on cellular internalization pathways. *Proceedings of the National Academy of Sciences*, 105(33):11613, 2008.

[45] Khlebtsov B.; Khanadeev V.; Bogatyrev V.; Dykman L.; Khlebtsov N. Engineering of plasmon-resonant nanostructures for biomedical applications. In *Tenth International Conference on Light Scattering by Non-spherical Particles, 2007*.

[46] Alkilany A.M.; Nagaria P.K.; Hexel C.R.; Shaw T.J.; Murphy C.J.; Wyatt M.D. Cellular uptake and cytotoxicity of gold nanorods: molecular origin of cytotoxicity and surface effects. *Small*, 5(6):701–708, 2009.

[47] Chen Y.S.; Hung Y.C.; Liau I.; Huang G.S. Assessment of the in vivo toxicity of gold nanoparticles. *Nanoscale research letters*, 4(8):858–864, 2009.

[48] Fischer H.C.; Chan W.C.W. Nanotoxicity: the growing need for in vivo study. *Current opinion in biotechnology*, 18(6):565–571, 2007.

[49] Murphy C.J.; Gole A.M.; Stone J.W.; Sisco P.N.; Alkilany A.M.; Goldsmith E.C.; Baxter S.C. Gold nanoparticles in biology: beyond toxicity to cellular imaging. *Accounts of chemical research*, 41(12):1721–1730, 2008.

[50] Lewinski N.; Colvin V.; Drezek R. Cytotoxicity of nanoparticles. *Small*, 4(1):26–49, 2008.

[51] Alexis F.; Pridgen E.; Molnar L.K.; Farokhzad O.C. Factors affecting the clearance and biodistribution of polymeric nanoparticles. *Molecular pharmaceutics*, 5(4):505–515, 2008.

[52] Janeway C.A.Jr. Immunobiology. *6th Edition*, 2006.

[53] Bastus N.G.; Sánchez-Tilló E.; Pujals S.; Farrera C.; Kogan M.J.; Giralt E.; Celada A.; Lloberas J.; Puntes V. Peptides conjugated to gold nanoparticles induce macrophage activation. *Molecular immunology*, 46(4):743–748, 2009.

[54] Dobrovolskaia M.A.; Aggarwal P.; Hall J.B.; McNeil S.E. Preclinical studies to understand nanoparticle interaction with the immune system and its potential effects on nanoparticle biodistribution. *Molecular pharmaceutics*, 5(4):487–495, 2008.

[55] Pissuwan D.; Valenzuela S.M.; Killingsworth M.C.; Xu X.; Cortie M.B. Targeted destruction of murine macrophage cells with bioconjugated gold nanorods. *Journal of Nanoparticle Research*, 9(6):1109–1124, 2007.

[56] Moghimi S.M.; Hunter A.C.; Murray J.C. Nanomedicine: current status and future prospects. *The FASEB journal*, 19(3):311, 2005.

[57] Hamblin MR; Miller JL; Rizvi I.; Loew HG; Hasan T. Pegylation of charged polymer-photosensitiser conjugates: effects on photodynamic efficacy. *British journal of cancer*, 89(5):937–943, 2003.

[58] Arnida A.M.; Ghandehari H. Cellular uptake and toxicity of gold nanoparticles in prostate cancer cells: a comparative study of rods and spheres. *Journal of Applied Toxicology*, 30(3):212–217, 2010.

[59] Takahashi H.; Niidome T.; Nariai A.; Niidome Y.; Yamada S. Gold nanorod-sensitized cell death: microscopic observation of single living cells irradiated by pulsed near-infrared laser light in the presence of gold nanorods. *Chemistry Letters*, 35(5):500–501, 2006.

[60] Pissuwan D.; Valenzuela S.M.; Miller C.M.; Cortie M.B. A golden bullet? Selective targeting of Toxoplasma gondii tachyzoites using antibody-functionalized gold nanorods. *Nano Lett*, 7(12):3808–3812, 2007.

[61] Norman R.S.; Stone J.W.; Gole A.; Murphy C.J.; Sabo-Attwood T.L. Targeted photothermal lysis of the pathogenic bacteria, Pseudomonas aeruginosa, with gold nanorods. *Nano Lett*, 8(1):302–306, 2008.

[62] He W.; Henne W.A.; Wei Q.; Zhao Y.; Doorneweerd D.D.; Cheng J.X.; Low P.S.; Wei A. Two-photon luminescence imaging of bacillus spores using peptide-functionalized gold nanorods. *Nano research*, 1(6):450–456, 2008.

[63] Dickerson E.B.; Dreaden E.C.; Huang X.; El-Sayed I.H.; Chu H.; Pushpanketh S.; McDonald J.F.; El-Sayed M.A. Gold nanorod assisted near-infrared plasmonic photothermal therapy (PPTT) of squamous cell carcinoma in mice. *Cancer letters*, 269(1):57–66, 2008.

[64] Jain P.K.; Lee K.S.; El-Sayed I.H.; El-Sayed M.A. Calculated absorption and scattering properties of gold nanoparticles of different size, shape, and composition: applications in biological imaging and biomedicine. *J. Phys. Chem. B*, 110(14):7238–7248, 2006.

[65] Link S.; Burda C.; Mohamed MB; Nikoobakht B.; El-Sayed MA. Femtosecond transient-absorption dynamics of colloidal gold nanorods: Shape independence of the electron-phonon relaxation time. *Physical Review B*, 61(9):6086–6090, 2000.

[66] Leonov A.P.; Zheng J.; Clogston J.D.; Stern S.T.; Patri A.K.; Wei A. Detoxification of gold nanorods by treatment with polystyrenesulfonate. *ACS nano*, 2(12):2481–2488, 2008.

[67] Gole A.; Murphy C.J. Polyelectrolyte-coated gold nanorods: synthesis, characterization and immobilization. *Chem. Mater*, 17(6):1325–1330, 2005.

[68] Ni W.; Yang Z.; Chen H.; Li L.; Wang J. Coupling between Molecular and Plasmonic Resonances in Freestanding Dye- Gold Nanorod Hybrid Nanostructures. *Journal of the American Chemical Society*, 130(21):6692–6693, 2008.

[69] Schneider G.; Decher G.; Nerambourg N.; Praho R.; Werts M.H.V.; Blanchard-Desce M. Distance-dependent fluorescence quenching on gold nanoparticles ensheathed with layer-by-layer assembled polyelectrolytes. *Nano Lett*, 6(3):530–536, 2006.

[70] Lakowicz J.R. In principles of fuorescence spectroscopy. *Kluwer Academic Plenum Press, New York.*, 1999.

Conclusions

The studies reported in this PhD thesis have highlighted a number of possible applications for spherically and non-spherically symmetric gold nanoparticles in biology and medicine for imaging and sensing, based on their peculiar spectroscopic properties. Noble metal (especially gold and silver nanoparticles) are in fact characterized by the phenomenon known as surface plasmon resonance (SPR), an in-phase oscillation of all the conduction band electrons that resonates with the light wave electric field. The resonance frequency depends on the size, shape, orientation and dielectric constant of the nanoparticle. The coupling of SPR with the electromagnetic field leads to a large enhancement of all the nanoparticle radiative properties, such as absorption and scattering. The extinction cross section of these nanoparticles is 10^5-10^6 larger than that of organic dye, they are extremely photostable and, depending on the shape, they convert efficiently light into heat. Moreover, anisotropic gold nanoparticles can emit an enhanced luminescence signal (TPL) when excited by Two-Photon Excitation (TPE) (when coupled with an appropriate plasmon resonance). These properties promise to improve the usefulness of these nanoparticles for in-vivo imaging in the NIR region of the electromagnetic spectrum.

According to these considerations we have developed our project on two lines related to the use of gold nanoparticles for sensing and non linear imaging.

The aim of the first part of this research project is to exploit changes of the dye excited-state lifetime and brightness induced by its interaction with the gold surface plasmons for the detection of tiny amounts of protein in solution under physiological conditions. The system we investigated is based on 10 and 5 nm diameter spherically symmetric gold NPs coupled (via a biotin-streptavidin linker) to the FITC dye and to a specific protein antibody. The interaction of the fluorophore with the gold surface plasmon resonances, mainly occuring through quenching, affects the excited state lifetime that is measured on single NP or small aggregates by fluorescence burst analysis in highly diluted NP suspensions. The binding of protein to the gold NPs through antigen-antibody recognition further modifies the fluorophore excited-state lifetime, which change can then be used to measure the protein concentration.

We have tested the nanodevice by bovine serum albumin (BSA) and the tumor marker p53 protein, both in standard solutions and in total cell extracts. The analysis reported here suggests that the gold NP-FITC-Ab_{p53} nano-constructs can be used to detect the presence of traces (5 pM limit of detection) of p53 proteins in TCEs opening the way to their application to in-vivo studies.
Moreover, we have developed a spectroscopic method to measure the local temperature increase on non spherically symmetric gold NPs, based on the measurement of the temperature dependent lifetime of the Rhodamine-B dye. This RhodamineB-NPs assay plays the role of a molecular thermometer and can be tested in-vivo to evaluate the thermal damage of tumoral cells induced by heating due to NPs. The hybrid sensor, composed of a gold NPs complexed to Rh-B, can then be used for imaging and photothermal purposes at the same time: the infrared laser radiation can excite both Rhodamine-B and TPL from the gold NRs in order to visualize the internalization of the sensor in cells and the same radiation can heat the NRs, damaging the tumor cell.
In the second part of the project non spherically symmetric gold nanoparticles were exploited as probes in cellular imaging. Gold NP were synthesized by the group of Prof. Pallavicini (University of Pavia) using for the first time in the seed growth method approach a zwitterionic surfactant, laurylsulphobetaine (LSB). The LSB concentration in the growth solution allows to control the dimension of the NPs and the SPR position, that can be tuned in the 700-1100 nm Near Infrared range. The samples have been analyzed with a number of structural techniques to obtain a complete characterization: absorption spectra in the UV-Visible region, TEM images of the suspensions, Fluorescence Correlation Spectroscopy (FCS) and Dynamic Light Scattering (DLS) experiments in suspensions. From these data we reached information on the nanoparticles shapes, dimensions and aggregation. In particular, three different populations have been found: nanospheres with diameter lower than 20 nm, nanostars characterized by large trapezoidal branches, and asymmetric branched nanoparticles with high aspect ratio ($\cong$3-4).
A through characterization of the NPs Two-Photon Luminescence (TPL) was performed for imaging applications by employing two photon excitation (TPE). The dependence of the TPL intensity on the power, wavelength and polarization of the incident light intensity was studied and TPL was exploited to study the cellular uptake of the nanoparticles in different cell lines (macrophages and HEK cells). NPs synthesized with both LSB and CTAB surfactant are internalized in the cytoplasm of HEK and macrophages. Pegylated gold NPs are otherwise invisible to the immune system and no cellular uptake was detected.

Collaborations and Manuscripts

List of the collaborations that have make possible this PhD work:

- General Chemistry Department, University of Pavia, Pavia, Italy In particular the group of Prof. P.Pallavicini
- Environment and Terrytory Department, University of Milano-Bicocca, Milan, Italy
  In particular Dr. P.Mantecca, Dr. G.Soncini and Dr. Maurizio Gualtieri (Polaris Project)
- Department of Biotechnology and Bioscience, University of Milano-Bicocca, Milan, Italy.
  In particular Prof. Francesca Granucci, Dr. Ivan Zanoni, Dr. Tatiana Gorletta and Dr. Marco Di Gioia

List of the manuscripts related to this PhD work:

- M. Caccia, L. Sironi, M. Collini, G. Chirico, I. Zanoni, and F. Granucci. "Image filtering for two-photon deep imaging of lymphonodes", Eur. Biophys. J., 37:979987, Jul 2008.
- S. Freddi, L. D'Alfonso, M. Collini, M. Caccia, L. Sironi, G. Tallarida, S. Caprioli, and G. Chirico. "Excited-state lifetime assay for protein detection on gold colloids-fluorophore complexes.", J. Phys. Chem. C, 113:27222730, Jan 2009.
- L.Sironi, S.Freddi, L.D'Alfonso, M. Collini, T. Gorletta, S.Soddu, G.Chirico. "P53 detection by fluorescence lifetime on a hybrid fluorescein-isothiocyanate gold nanosensor", J.Biomedical nanotechnology, 5: 683-691, 2009.
- L. Sironi, S. Freddi, L. D'Alfonso, M. Collini, T. Gorletta, S. Soddu, G. Chirico. "In-vitro and in-vivo detection of p53 by fluorescence lifetime on a hybrid FITC-gold nanosensor", Proceedings of the SPIE, 7574:757403, 2010

- M. Caccia, T. Gorletta, L. Sironi, I. Zanoni, C. Salvetti, M. Collini, F. Granucci., G. Chirico. "Two Photon Microscopy Intravital Study of DC-Mediated Anti-Tumor Response of NK Cells", Proceedings of the SPIE, 7565:75650Q, 2010

- P. Pallavicini, G. Chirico, M. Collini, G. Dacarro, A. Dona', L. D'Alfonso, A. Falqui, Y. A. Diaz-Fernandez, S. Freddi, B. Garofalo, A. Genovese, L. Sironi and A. Taglietti. "Synthesis of branched gold nanoparticles with tunable Near-InfraRed Localized Surface Plasmon Resonance using a zwitterionic surfactant for the seed-growth method", Chem. Commun., 2011, DOI: 10.1039/C0CC02682D